Jordan Journal of Mechanical and Industrial Engineering (JJMIE)

JJMIE is a high-quality scientific journal devoted to fields of Mechanical and Industrial Engineering. It is published by Hashemite University in cooperation with the Jordanian Scientific Research and Innovation Support Fund, Ministry of Higher Education and Scientific Research.

SUBMISSION ADDRESS:

Prof. Moh'd Sami Ashhab, Editor-in-Chief
Jordan Journal of Mechanical & Industrial Engineering,
Hashemite University,
PO Box 330127, Zarqa, 13133 , Jordan
E-mail: jjmie@hu.edu.jo

Hashemite Kingdom of Jordan

Hashemite University

Jordan Journal of Mechanical and Industrial Engineering

JJMIE

An International Peer-Reviewed Scientific Journal

Financed by Scientific Research Support Fund

Volume 15, Number 2, June 2021

http://jjmie.hu.edu.jo/

ISSN 1995-6665

Jordan Journal of Mechanical and Industrial Engineering (JJMIE)

JJMIE is a high-quality scientific journal devoted to fields of Mechanical and Industrial Engineering. It is published by Hashemite University in cooperation with the Jordanian Scientific Research and Innovation Support Fund, Ministry of Higher Education and Scientific Research.

Introduction: The Editorial Board is very committed to build the Journal as one of the leading international journals in mechanical and industrial engineering sciences in the next few years. With the support of the Ministry of Higher Education and Scientific Research and Jordanian Universities, it is expected that a heavy resource to be channeled into the Journal to establish its international reputation. The Journal's reputation will be enhanced from arrangements with several organizers of international conferences in publishing selected best papers of the conference proceedings.

Aims and Scope: *Jordan Journal of Mechanical and Industrial Engineering* (JJMIE) is a refereed international journal to be of interest and use to all those concerned with research in various fields of, or closely related to, mechanical and industrial engineering disciplines. *Jordan Journal of Mechanical and Industrial Engineering* aims to provide a highly readable and valuable addition to the literature which will serve as an indispensable reference tool for years to come. The coverage of the journal includes all new theoretical and experimental findings in the fields of mechanical and industrial engineering or any closely related fields (Materials, Manufacturing, Management, Design, Thermal, Fluid, Energy, Control, Mechatronics, and Biomedical). The journal also encourages the submission of critical review articles covering advances in recent research of such fields as well as technical notes.

Guide for Authors

Manuscript Submission:
High-quality submissions to this new journal are welcome now and manuscripts may be either submitted online or email.

Online: For online and email submission upload one copy of the full paper including graphics and all figures at the online, submission site, accessed via http://jjmie.hu.edu.jo. The manuscript must be written in MS Word Format. All correspondence including notification of the Editor's decision and requests for revision, takes place by e-mail and via the Author's homepage, removing the need for a hard-copy paper trail

Submission address and contact :
Prof. Moh'd Sami Ashhab
Editor-in-Chief
Jordan Journal of Mechanical & Industrial Engineering, Hashemite University
PO Box 330127, Zarqa, 13115, Jordan
E-mail: jjmie@hu.edu.jo

Types of contributions*:* Original research papers and Technical reports

Corresponding author: Clearly indicate who is responsible for correspondence at all stages of refereeing and publication, including post-publication. Ensure that telephone and fax numbers (with country and area code) are provided in addition to the e-mail address and the complete postal address. Full postal addresses must be given for all co-authors.

Original material: Submission of an article implies that the work described has not been published previously (except in the form of itstan abstract or as part of a published lecture or academic thesis), that it is not under consideration for publication elsewhere, tha publication is approved by all authors and that, if accepted, it will not be published elsewhere in the same form, in English or in any other language, without the written consent of the Publisher. Authors found to be deliberately contravening the submission guidelines on originality and exclusivity shall not be considered for future publication in this journal.

Withdrawing: If the author chooses to withdraw his article after it has been assessed, he shall reimburse JJMIE with the cost of reviewing the paper.

Manuscript Preparation:

General: Editors reserve the right to adjust style to certain standards of uniformity. Original manuscripts are discarded after .publication unless the Publisher is asked to return original material after use. Please use MS Word for the text of your manuscript

Structure: Follow this order when typing manuscripts: Title, Authors, Authors title, Affiliations, Abstract, Keywords, Introduction, Main text, Conclusions, Acknowledgements, Appendix, References, Figure Captions, Figures and then Tables. Please supply figures imported into the text AND also separately as original graphics files. Collate acknowledgements in a separate section at the end of the article and do not include them on the title page, as a footnote to the title or otherwise.

Text Layout: Use 1.5 line spacing and wide (3 cm) margins. Ensure that each new paragraph is clearly indicated. Present tables and figure legends on separate pages at the end of the manuscript. If possible, consult a recent issue of the journal to become familiar with layout and conventions. All footnotes (except for table and corresponding author footnotes) should be identified with superscript Arabic numbers. To conserve space, authors are requested to mark the less important parts of the paper (such as records of experimental results) for printing in smaller type. For long papers (more than 4000 words) sections which could be deleted without destroying either the sense or the continuity of the paper should be indicated as a guide for the editor. Nomenclature should conform to that most frequently used in the scientific field concerned. Number all pages consecutively; use 12 or 10 pt font size and standard fonts.

Corresponding author: Clearly indicate who is responsible for correspondence at all stages of refereeing and publication, including post-publication. The corresponding author should be identified with an asterisk and footnote. Ensure that telephone and fax numbers (with country and area code) are provided in addition to the e-mail address and the complete postal address. Full postal addresses must be given for all co-authors. Please consult a recent journal paper for style if possible.

Abstract: A self-contained abstract outlining in a single paragraph the aims, scope and conclusions of the paper must be supplied.

Keywords: Immediately after the abstract, provide a maximum of six keywords (avoid, for example, 'and', 'of'). Be sparing with abbreviations: only abbreviations firmly established in the field may be eligible.

Symbols: All Greek letters and unusual symbols should be identified by name in the margin, the first time they are used.

Units: Follow internationally accepted rules and conventions: use the international system of units (SI). If other quantities are mentioned, give their equivalent quantities in SI

Maths: Number consecutively any equations that have to be displayed separately from the text (if referred to explicitly in the text).

References: All publications cited in the text should be presented in a list of references following the text of the manuscript.

Text: Indicate references by number(s) in square brackets in line with the text. The actual authors can be referred to, but the reference number(s) must always be given.

List: Number the references (numbers in square brackets) in the list in the order in which they appear in the text.

Examples:

Reference to a journal publication:

[1] M.S. Mohsen, B.A. Akash, "Evaluation of domestic solar water heating system in Jordan using analytic hierarchy process". Energy Conversion & Management, Vol. 38 (1997) No. 9, 1815-1822.

Reference to a book:

[2] Strunk Jr W, White EB. The elements of style. 3rd ed. New York: Macmillan; 1979.

Reference to a conference proceeding:

[3] B. Akash, S. Odeh, S. Nijmeh, "Modeling of solar-assisted double-tube evaporator heat pump system under local climate conditions". 5th Jordanian International Mechanical Engineering Conference, Amman, Jordan, 2004.

Reference to a chapter in an edited book:

[4] Mettam GR, Adams LB. How to prepare an electronic version of your article. In: Jones BS, Smith RZ, editors. Introduction to the electronic age, New York: E-Publishing Inc; 1999, p. 281-304

Free Online Color : If, together with your accepted article, you submit usable color and black/white figures then the journal will ensure that these figures will appear in color on the journal website electronic version.

Tables: Tables should be numbered consecutively and given suitable captions and each table should begin on a new page. No vertical rules should be used. Tables should not unnecessarily duplicate results presented elsewhere in the manuscript (for example, in graphs). Footnotes to tables should be typed below the table and should be referred to by superscript lowercase letters.

Notification: Authors will be notified of the acceptance of their paper by the editor. The Publisher will also send a notification of receipt of the paper in production.

Copyright: All authors must sign the Transfer of Copyright agreement before the article can be published. This transfer agreement enables Jordan Journal of Mechanical and Industrial Engineering to protect the copyrighted material for the authors, but does not relinquish the authors' proprietary rights. The copyright transfer covers the exclusive rights to reproduce and distribute the article, including reprints, photographic reproductions, microfilm or any other reproductions of similar nature and translations.

Proof Reading: One set of page proofs in MS Word format will be sent by e-mail to the corresponding author, to be checked for typesetting/editing. The corrections should be returned within 48 hours. No changes in, or additions to, the accepted (and subsequently edited) manuscript will be allowed at this stage. Proofreading is solely the author's responsibility. Any queries should be answered in full. Please correct factual errors only, or errors introduced by typesetting. Please note that once your paper has been proofed we publish the identical paper online as in print.

JJMIE

Volume 15, Number 2, June. 2021
ISSN 1995-6665

Jordan Journal of Mechanical and Industrial Engineering

PAGES	PAPERS

JJMIE

Volume 15, Number 2, June. 2021
ISSN 1995-6665
Pages 153 - 167

Jordan Journal of Mechanical and Industrial Engineering

Optimal Quay Crane Assignment and Scheduling in Port's Container Terminals

Abbas Al-Refaie [a] *, Hala Abedalqader [b]

[a] *Department of Industrial Engineering, University of Jordan, Amman, 11942.*

[b] *Received her master degree from Department of Industrial Engineering, University of Jordan.*

Received September 9 2019 *Accepted April 14 2021*

Abstract

Effective scheduling of quay cranes can increase throughput, and lead to higher revenues of container terminals. This research, therefore, proposes an optimization model to deal with quay crane assignment and scheduling problem (QCASP) considering multiple objective functions. The first objective minimizes the handling makespan in the terminal by sequencing the work of quay cranes on vessels' bays, while the second objective aims to maximize the number of containers being handled by each quay crane (QC) for all QCs in the container port to make sure that all QCs are utilized during the handling process. Finally, the third objective seeks to maximize satisfaction levels on handling completion times. The model takes into consideration the non-violence of non-crossing constraints and task completion without preemption constraints. Illustrations of the developed model were provided. The results showed that the proposed optimization model is found effective in optimizing terminal performance by optimizing the three stated objective functions concurrently. In practice, solving the QCASP helps in enhancing utilization of QCs, shortening service period at the terminal, and increasing the throughput at the terminal. In conclusion, the proposed optimization model can benefit planning engineers in determining optimal quay crane assignment and scheduling. Future research will focus on integrating berth allocation problem with QCASP.

Keywords: Optimization, Quay cranes, Scheduling and Assignment.;

1. Introduction

The ports irrespective of their location mainly face the problems of congestion, lost opportunities, high costs, and instability if not decreasing level of customer satisfaction. Seaports are complex dynamic systems consisting of numerous connecting elements, influenced by several random factors. Accordingly, full utilization of the obtainable resources and efficient management of operations are two major goals. Under these two goals numerous objectives can be accomplished; such as, increasing the port throughput and usage of resources (berths, cranes, quay, yards.), minimizing handling time, decreasing port congestion [1-2].

It is well known that the container terminal business is capital intensive. Therefore, effective scheduling of resources; especially quay cranes (QCs), can increase throughput and lead to higher revenues of container terminals [3-4]. Quay crane assignment and scheduling problem (QCASP) is a key task in seaside operations, where available quay cranes are assigned to vessels and their operations are scheduled. Therefore, this research develops an optimization model to deal with the QCASP with three main objectives including minimizing makespan, maximizing the number of operational QCs, and maximizing satisfaction level on bays' completion times. In practice, this model provides great assistance to planning engineers in ports in determining the optimal schedule of QCs and thereby improving terminal performance. The remainder of this research including the introduction is organized as follows. Section 2 reviews previous literature related to QCASP. Section 3 develops an optimization model to deal with QCASP. Section 4 illustrates the developed optimization models. Section 5 provides results and discussion. Finally, Section 6 presents the conclusions and future research.

2. Literature Review

Several studies have handled the QCASP. For example, Hu [5] studied the QCASP with the objective of minimizing the movements of QCs during the operations of each vessel in Ningbo Beilun Port in China using integer linear programming model. Lee and Wang [6] integrated berth allocation and QCASP to minimize makespan of handling all container ships, and reduce handling time of each container ship at each berth via genetic algorithm. Lee and Chen [7] optimized the QCSP with non-crossing constraints with two approximation algorithms, which are the best partition method and the enhanced partition method, to obtain optimal makespan for the QCSP. Zeng *et al*. [8] proposed a berth reallocation and quay crane rescheduling models to tackle irregular disruptions in container terminals, targeting the minimization of negative impacts of disruption. A Tabu search algorithm was used to solve

* Corresponding author e-mail: abbas.alrefai@ju.edu.jo.

the berth reallocation and QC rescheduling models. Data of numerical experiments were collected from the Tianjin Five Continents International Container Terminal. Chung and Chan [9] examined the QCSP aiming to minimize the makespan (completion time) of tasks. Workload balancing heuristics were applied in a Genetic Algorithm to solve the model and compare the workload balancing between the QCs. Diabat and Theodorou [10] developed a mathematical formulation for the integrated QCASP aiming to minimize the handling makespan of the ship while assuming that all QCs were identical with corresponding handling rates. Furthermore, a unidirectional movement for cranes was adopted so that QCs began handling the lowest-indexed bay out of the total bays, and the clearance conditions were enforced between adjacent QCs. Fu *et al.* [11] analyzed the integrated quay crane assignment and scheduling problem with the objective of maximizing the sum of the weighted work completion flag. A genetic algorithm was proposed to solve the problem, and different sizes instances were used to test the performance of the proposed model and the developed genetic algorithm. Al-Dhaheri *et al.* [12] studied the QCSP to minimize the absolute value of the sum of the differences in workload over time between all bays using mixed-integer programming. It was assumed that a QC could be assigned to at most one bay, a single QC could handle at most one task at an instant in time, QCs were mounted on a single rail so that the crossing of cranes was prevented, while the bi-directional movement was allowed. Identical service rates were assumed for all cranes, and the safety distance was implicitly taken into consideration. Msakni *et al.* [13] investigated the QCASP with the objective of minimizing the sum of selected QC-to-bay assignments required to achieve all container works (minimizing the makespan). A branch-and-price algorithm based on a set covering formulation was proposed to solve the problem. Chang *et al*. [14] studied the QCSP with the objective of minimizing the operation time of all ships at port and obtaining operation equilibrium of quay cranes using a genetic algorithm. The main assumptions were, all quay cranes had the same capacity and the same moving speed; the berthing time, berthing location and container stowage plan of every ship were all given and known. Chu *et al.* [15] studied the QCSP with the aim of minimizing the makespan of the ship handling operation, taking into account the constraint of the ship balance. Multi-Crane double cycling (double cycling means that a QC can unload the ship's container and load the ship's container in the same cycle) model was developed to optimize the operation sequence of each QC while considering ship stabilization during loading/ unloading operations. A Lagrangian relaxation heuristic algorithm was designed to solve the model, and one instance of a ship berthing in Tianjin Port in China was used to test the model validity.

In the previously-presented studies, the most common objective function in the QCASP was minimizing the makespan of handling operations, completion time of tasks [5-6] and minimizing costs of handling [7].However, this research takes into consideration multiple objective functions; maximizing the number of operated QCs, minimizing the makespan, and maximizing satisfaction on completion times, with their more realistic conditions; such as, the non-crossing condition among operating QCs, and quay crane of distinct capacity, moving speed, and service rates.

3. The Proposed QCASP Optimization Model

The primary elements in the QCASP are the set of vessels that will be operated, and the set of quay cranes available in the terminal. Let Q denotes the set of QCs available to work in the terminal indexed by $q \in Q,\ q = (1,...,N)$, and B denotes the set of all bays belonging to berthing vessels in the terminal indexed by $b \in B,\ b = (1,...,S)$. In addition, let B_v denotes the subset of bays belonging to specific vessel $v \in V$ from the set of vessels berthing in the terminal. The QCASP model determines the number of quay cranes assigned to each vessel bays and their sequence of operations required to achieve the minimal handling period. The main assumptions and practical considerations of the proposed model are:

The length of each vessel is split into compartments for containers storage, which are termed as bays. Bay areas are assumed to be indexed sequentially along the quay, according to their position from left to right as shown in Fig. 1.

The bays of all berthing vessels are ordered from left to right in ascending order dealing with them as a single ship problem.

Safety margin between operating QCs working on the same vessel is not considered.

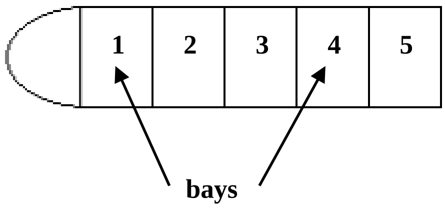

Figure 1. A vessel bays ordered from left to right in ascending order.

Each bay cannot be served by multiple cranes in the same time period. And, once a crane started its operation on a certain bay, it cannot leave until completing the loading and/ or unloading operations at that bay.

The quay cranes movement is bidirectional, giving them the freedom to travel in both directions left and right, as long as they do not cross each other. However, cranes can move from a vessel to another while serving it (dynamic allocation) as shown in Fig. 2.

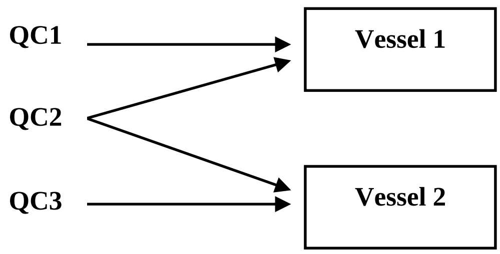

Figure 2. Dynamic allocation of QCs to berthing vessels.

The time required for quay cranes to travel between bays of vessels is small if compared to container handling times. Therefore, horizontal moving time of quay cranes is not considered in this model.

The quay cranes are positioned on a single track; therefore, they are not allowed to cross each other to shift position. Moreover, it is assumed that they are indexed in ascending order from left to right; this helps in preventing middle numbered QCs from serving bays at the ends. In other words, each bay has feasible quay crane or quay cranes, which can serve it.

The parameters of the proposed model are: (1) Total number of bays for the berthing vessels in the terminal (S), and their workload, the number of containers that should be loaded and/ or unloaded in each bay (ω_b). In addition to the number of bays belonging to each vessel (S_v) and (2) number of available quay cranes in the terminal (N), and their working rate in container/ hour (r_q).

The first objective function is to minimize the makespan, ψ, (latest completion time of all handling tasks for the bays of vessels in the terminal), which is represented as follows:

$$Min \quad \psi \tag{1}$$

The second objective function is to maximize the number of containers operated by each quay crane$q$, ζ_q, for better employment of all QCs in the terminal, this is represented as:

$$Max \sum_{q=1}^{N} \zeta_q \tag{2}$$

The objective functions are subject to the following constraints:

1. Let the binary decision variable λ_{bq} determines to which quay crane q a bay b is assigned, it equals 1 if quay crane $q \in Q$ is assigned to bay $b \in B$ (=0 otherwise). In order to meet all handling tasks of all bays in the terminal, each bay shall be assigned to only one quay crane in order to complete the loading and/ or unloading operations of it without preemption. Mathematically,

$$\sum_{q=1}^{N} \lambda_{bq} = 1, \qquad \forall b \in B \tag{3}$$

2. Let the binary decision variable $\upsilon_{bb'}$ determines the work precedence between bays, it equals 1 if the work on bay $b \in B$ is completed before the work on bay $b' \in B$ starts (= 0 otherwise). Also, if bays are being served simultaneously, the bays cannot be assigned to the same quay crane. Given that the quay cranes are moving on the same track, then the non-crossing constraint is formulated as given in Inequality (4).

$$\sum_{q=1}^{N} q \times \lambda_{bq} - \sum_{q=1}^{N} q \times \lambda_{b'q} + 1 \le M \times (\upsilon_{bb'} + \upsilon_{b'b}), \quad \forall b, \ b' \in B \mid b < b' \tag{4}$$

Fig. 3 shows how different berthing vessels are combined and served by QCs as a single ship problem. If bays numbers 3 and 4 are being served simultaneously, the right-hand side of inequality (4) will be zero. Accordingly, if the quay crane serving bay number 3, which is equivalent to (b) in the inequality, is of higher order than the one serving bay number 4 (b'); e.g. the crane serving bay number 3 is of order number 3, while the crane serving bay number 4 is of order number 2, the constraint will not be satisfied because after substituting the values in inequality (4), the result is (3-2+1=2, which is not less than or equal to zero). Consequently, the crossing between QCs moving on a single rail will be prevented.

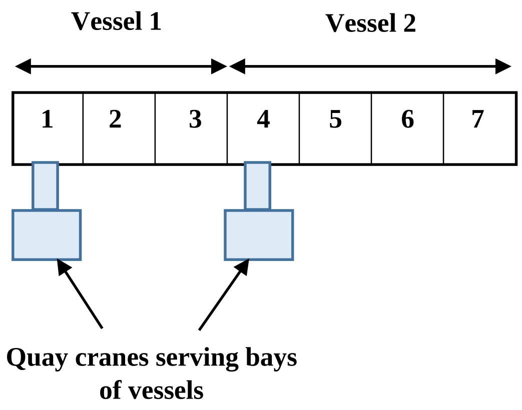

Figure 3. Quay cranes operating on bays of vessels.

3. To make sure that there is always enough space between any two quay cranes, in other words, a crane of order number 1 and another one of order number 3 will never be working on adjacent bays to make sure that there is enough space for quay crane number 2. This is represented as:

$$\sum_{q=1}^{N} q \times \lambda_{b'q} - \sum_{q=1}^{N} q \times \lambda_{bq} \le b' - b + M \times (\upsilon_{bb'} + \upsilon_{b'b}), \quad \forall b, b' \in B, b < b' \tag{5}$$

For more explanation to constraint (5), in Fig. 3 if bays numbers 2 and 3 are being serviced simultaneously, and the number of QCs serving them are 1 and 3, respectively. Such situation will not occur when applying this constraint because the term multiplied by the big M will be zero, however, ((3-1=2) which represents the QCs order numbers is not less than or equal to (3-2=1) which are the order numbers of bays $(b' - b)$ in the inequality). Accordingly, there will be always enough space for in between QCs.

4. The middle-numbered quay cranes shall not be assigned to end bays because this means that the quay cranes which are located on the bounds are pushed out of boundaries. For example, if in Fig. 3 the quay crane serving bay number one is QC number two, this will mean that quay crane number 1 is pushed out. Accordingly, equations (6) and (7) are used to define the feasible set of quay cranes that can be assigned to each bay:

$$\lambda_{bq} = 0, \quad \forall b \in B, q \in Q, q > b \tag{6}$$

$$\lambda_{bq} = 0, \quad \forall b \in B, q \in Q, S - b < N - q \tag{7}$$

Assume that there are 4 QCs in a certain MCT, then applying constraints (6) and (7) on the 7 bays in Fig. 3 gives the set of feasible QCs that can serve each bay as shown in Fig. 4. Total number of bays for the berthing vessels in the terminal (S), number of available quay cranes in the terminal (N).

Bay number	1	2	3	4	5	6	7
Feasible quay cranes	1	1 2	1 2 3	1 2 3 4	2 3 4	3 4	4

Figure 4. Bays and feasible quay cranes.

5. Given the number of containers, ω_b, that need loading/unloading in bay b and the working rate, r_q, of each quay crane, the processing time, ρ_b, for bay b needed to complete the tasks can be calculated:

$$\rho_b = \sum_{q=1}^{N} \frac{\lambda_{bq} \times \omega_b}{r_q}, \qquad \forall b \in B \quad (8)$$

6. The completion time of every bay processing is greater than or equal to its processing period. Moreover, let the decision variable h_v denotes the handling time of vessel $v \in V$, then the handling time of each vessel can be calculated as the latest completion time of its bays; mathematically:

$$C_b \ge \rho_b, \quad \forall b \in B \quad (9)$$

$$h_v \ge C_b, \quad \forall b \in B_v, v \in V \quad (10)$$

7. The work of QCs on bays is without preemption, this means that a quay crane shall complete its work on the current bay before moving to any other bay. This is assured by inequality (11), which determines the work sequence of every QC:

$$C_b \le C_{b'} - \rho_{b'} + M \times (1 - \upsilon_{bb'}), \quad \forall b, b' \in B, b \ne b' \quad (11)$$

8. The number of containers (size of workload) handled by each quay crane equals the sum of containers that need loading/unloading in the bays which the QC was assigned to; this is determined by equation (12):

$$\zeta_q = \sum_{b=1}^{S} \lambda_{bq} \, x \, \omega_b, \qquad \forall q \in Q \quad (12)$$

9. The makespan of processing jobs on all bays in the terminal is calculated as the largest completion time among all processed bays; that is:

$$\psi \ge C_b, \qquad \forall b \in B \quad (13)$$

10. Non-negative and binary variables are determined in constraints (14) and (15):

$$\psi, C_b, \rho_b, \zeta_q, h_v \ge 0, \quad \forall b \in B, q \in Q, v \in V \quad (14)$$

$$\lambda_{bq}, \upsilon_{bb'} \in \{0,1\} \quad (15)$$

Further, let SC_b denotes the satisfied completion time for bay b. It is also important to maximize the satisfactions on the bays' completion times. Ideally, the satisfaction will be 100% if the completion time meets the satisfied completion time; while the satisfaction decreases when the completion time exceeds the satisfied target [16-20]. Let μ_b denote the membership function that represents the satisfaction on bays' completion times. Let Δ^+_b denotes the maximal positive permitted deviation from SC_b. The *STB* function is shown in Fig.5.

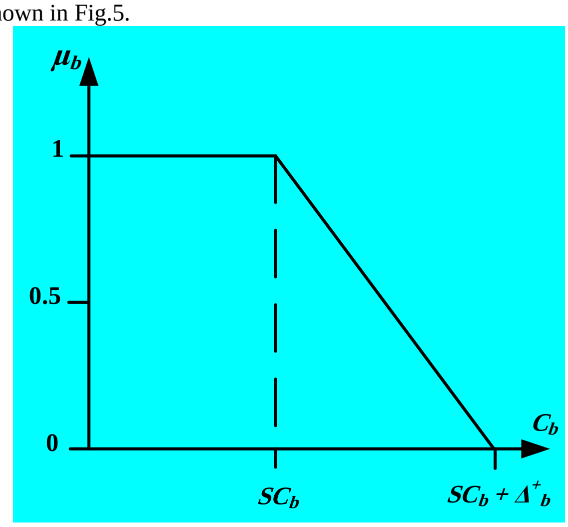

Figure 5. The (*STB*) type satisfaction.

Then, the objective function is to maximize the satisfaction on completion times of bays; or, mathematically

$$Max \sum_{b=1}^{S} \mu_b \quad (16)$$

Let δ^+_b denotes any positive deviation from the target value, SC_b. the value of δ^+_b is always positive and less than the maximum allowed deviation as in Eq. (17).

$$0 \le \delta^+_b \le \Delta^+_b, \forall b \quad (17)$$

Furthermore, the amount of any positive deviation is determined by observing how far the difference between SC_b and the actual completion time, C_b, is expressed as:

$$C_b - \delta^+_b = SC_b, \forall b \quad (18)$$

Also, the value of the membership function is calculated using Eq. (19).

$$\mu_b + \frac{\delta^+_b}{\Delta^+_b} = 1, \forall b \quad (19)$$

Finally, the value of each membership should not be less than the minimum allowable satisfaction θ_b which is expressed as:

$$\mu_b \ge \theta_b, \quad \forall b \quad (20)$$

The cranes assignment schedule and sequence of operations on bays in order to minimize the time required to complete all handling processes are obtained by solving the complete optimization model, which is written as:

$$Min = \psi$$

$$Max = \sum_{q=1}^{N} \zeta_q + \sum_{b=1}^{S} \mu_b$$

Subject to:

$$\sum_{q=1}^{N} \lambda_{bq} = 1, \forall b \in B$$ [QCs assignment to bays]

$$\sum_{q=1}^{N} q \times \lambda_{bq} - \sum_{q=1}^{N} q \times \lambda_{b'q} + 1 \le M \times (\upsilon_{bb'} + \upsilon_{b'b}), \forall b, b' \in B, b < b'$$ [Non-crossing constraint]

$$\sum_{q=1}^{N} q \times \lambda_{b'q} - \sum_{q=1}^{N} q \times \lambda_{bq} \le b' - b + M \times (\upsilon_{bb'} + \upsilon_{b'b}), \forall b, b' \in B, b < b'$$ [Keeping enough space between QCs]

$$\lambda_{bq} = 0, \forall b \in B, q \in Q, q > b$$
$$\lambda_{bq} = 0, \forall b \in B, q \in Q, S - b < N - q$$ [Defining the feasible QC or QCs for working on each bay]

$$\rho_b = \sum_{q=1}^{N} \frac{\lambda_{bq} \times \omega_b}{r_q}, \forall b \in B$$ [Processing period for each bay]

$$C_b \ge \rho_b, \forall b \in B$$ [Completion time for work on each bay]

$$h_v >= C_b, \forall b \in B_v, v \in V$$ [Handling time of each vessel]

$$C_b \le C_{b'} - \rho_{b'} + M \times (1 - \upsilon_{bb'}), \forall b, b' \in B, b \ne b'$$ [Precedence between bays]

$$\zeta_q = \sum_{b=1}^{S} \lambda_{bq} x\, \omega_b, \forall q \in Q$$ [Number of containers handled by each QC]

$$\psi \ge C_b, \forall b \in B$$ [Makespan]

$$\psi, C_b, \rho_b, \zeta_q, h_v \ge 0, \qquad \forall b \in B, q \in Q, v \in V$$ [Non-negative variables]

$$0 \le \delta_b^+ \le \Delta_b^+ \ , \forall b$$ [The deviation always positive]

$$C_b - \delta_b^+ = SC_b \ , \forall b$$ [The amount of any positive deviation]

$$\mu_b + \frac{\delta_b^+}{\Delta_b^+} = 1 \ , \forall b$$ [The value of the membership function]

$$\mu_b \ge \theta_b, \ \forall b$$ [The minimum allowable satisfaction]

$$\lambda_{bq}, \upsilon_{bb'} \in \{0,1\}$$ [Binary variables]

4. Results and Discussion

The proposed model was applied on three cases. The results and discussion of these cases are presented as follows.

4.1. Case I: Small sample size (3 vessels, 6 quay cranes, and 12 bays)

Consider three vessels that have already arrived and berthed in the terminal, then the load profile of each vessel (number of bays belonging to each vessel and the number of containers in each bay) is summarized in Table 1. The heterogeneous working rates of the quay cranes in the MCT are presented in Table 2.

Solving the proposed QCASP optimization model of 224 variables and 328 constraints using Lingo 11.0 (Processor: Intel (R) Core (TM) i5-4210U; CPU @ 1.70GHz, 2.40 GHz, elapsed time = 6.15 minutes), the total makespan, handling time periods for each vessel, processing and completions times for operations on each bay are obtained as summarized in Tables 3. Further, the calculated number of containers operated per crane is shown in Table 4.

Table 1. Berthing vessels' load profile.

Input	Value											
Vessel number	1			2					3			
Number of bays	3			5					4			
Total number of bays for all vessels (B)				12								
Bays numbers from left to right sequentially (b)	1	2	3	4	5	6	7	8	9	10	11	12
Number of containers in each bay (ω_b)	100	200	125	150	250	150	100	175	125	200	250	150

Table 2. Quay cranes working rates.

Quay crane number	Working rate (containers per hour) (r_q)
1	30
2	15
3	35
4	15
5	30
6	35

Table 3. Optimal results for QCASP model (Case I).

Variable		Final value											
ψ		14.29											
$\sum_{q=1}^{N} \zeta_q$		1975											
Vessel number		1			2					3			
h_v		14.29			14.29					11.43			
Processing and completion times of bays	Bay number	1	2	3	4	5	6	7	8	9	10	11	12
	ρ_b	3.33	6.67	4.17	10	7.14	4.29	2.86	11.67	4.17	6.67	7.14	4.29
	C_b	7.62	14.29	4.17	14.29	11.43	4.29	14.29	14.29	4.17	11.43	7.14	11.43

Table 4. Number of containers operated by each QC.

Quay crane number	Number of containers loaded/ unloaded (ζ_q)
1	425
2	150
3	500
4	175
5	325
6	400

In Table 3, it is noted that the total sum of operated containers (= 1975) equals the number of containers that shall be loaded/ unloaded from all bays of berthing vessels. This means that all required handling operations are accomplished. The optimal makespan is found 14.29 hours. The optimal values of the binary decision variable (λ_{bq}) determines which QC (q) is assigned to bay (b) when it takes the value of 1 $(\lambda_{bq} = 1)$ are listed in Table 5. The time precedence relations between bays, which define what bay shall complete its operation before the start of the job on another bay, are taken from the value of the binary decision variable $(\upsilon_{bb'})$; it equals 1 if the job on bay b completes before the start of operation on bay b'. Table 6 defines the precedence relations between tasks by summarizing the variables that took the value 1 $(\upsilon_{bb'} = 1)$

Table 5. The bays assigned to each quay crane.

Assignment Variable	Value meaning
$\lambda_{11} = 1$	QC number (1) is assigned to bay number (1)
$\lambda_{21} = 1$	QC number (1) is assigned to bay number (2)
$\lambda_{31} = 1$	QC number (1) is assigned to bay number (3)
$\lambda_{42} = 1$	QC number (2) is assigned to bay number (4)
$\lambda_{53} = 1$	QC number (3) is assigned to bay number (5)
$\lambda_{63} = 1$	QC number (3) is assigned to bay number (6)
$\lambda_{73} = 1$	QC number (3) is assigned to bay number (7)
$\lambda_{84} = 1$	QC number (4) is assigned to bay number (8)
$\lambda_{95} = 1$	QC number (5) is assigned to bay number (9)
$\lambda_{105} = 1$	QC number (5) is assigned to bay number (10)
$\lambda_{116} = 1$	QC number (6) is assigned to bay number (11)
$\lambda_{126} = 1$	QC number (6) is assigned to bay number (12)

Table 6. Time precedence relations among bays.

Output	Value meaning	Output	Value meaning
$\upsilon_{12} = 1$	Operation on bay No. (1) completes before the start of operation on bay No. (2).	$\upsilon_{610} = 1$	Operation on bay No. (6) completes before the start of operation on bay No. (10).
$\upsilon_{17} = 1$	Operation on bay No. (1) completes before the start of operation on bay No. (7).	$\upsilon_{612} = 1$	Operation on bay No. (6) completes before the start of operation on bay No. (12).
$\upsilon_{31} = 1$	Operation on bay No. (3) completes before the start of operation on bay No. (1).	$\upsilon_{910} = 1$	Operation on bay No. (9) completes before the start of operation on bay No. (10).
$\upsilon_{32} = 1$	Operation on bay No. (3) completes before the start of operation on bay No. (2).	$\upsilon_{912} = 1$	Operation on bay No. (9) completes before the start of operation on bay No. (12).
$\upsilon_{34} = 1$	Operation on bay No. (3) completes before the start of operation on bay No. (4).	$\upsilon_{117} = 1$	Operation on bay No. (11) completes before the start of operation on bay No. (7).
$\upsilon_{57} = 1$	Operation on bay No. (5) completes before the start of operation on bay No. (7).	$\upsilon_{1112} = 1$	Operation on bay No. (11) completes before the start of operation on bay No. (12).
$\upsilon_{65} = 1$	Operation on bay No. (6) completes before the start of operation on bay No. (5).	$\upsilon_{127} = 1$	Operation on bay No. (12) completes before the start of operation on bay No. (7).
$\upsilon_{67} = 1$	Operation on bay No. (6) completes before the start of operation on bay No. (7).		

For the third objective function which aims to maximize satisfactions on the bays' completion times, the minimum allowable satisfaction for each bay (θ_b) and the maximum allowable deviation (Δ^+_b) were decided values of 85% and 3, respectively. The optimal values of the satisfaction levels and positive deviations are summarized in Table 7. It is obvious that all the satisfaction levels on the completion times are larger than the threshold of 85%. In addition, the satisfaction level is 100% for 9 bays out of 12. The above results reveal the effectiveness of the proposed models in solving the QCASP. Finally, Table 8 shows the optimal sequence of QCs operations on bays over the planning horizon based on the defined precedence relations among bays and the results of assignment, processing and completion times.

Table 7. The optimal satisfaction levels on completion times.

Bay, b	Satisfied completion times, SC_b	Actual completion times, C_b	δ^{+}_{b}	μ_b
1	7.5	7.62	0.12	96%
2	14	14.29	0.29	90%
3	5	4.17	0	100%
4	15	14.29	0	100%
5	13	11.43	0	100%
6	6	4.29	0	100%
7	15	14.29	0	100%
8	15	14.29	0	100%
9	5	4.17	0	100%
10	11	11.43	0.43	86%
11	8	7.14	0	100%
12	13	11.43	0	100%

Table 8. Sequence of QCs operations (time periods x bays).

Time period	Bay number											
	1	2	3	4	5	6	7	8	9	10	11	12
1			QC1			QC3			QC5		QC6	
2			QC1			QC3			QC5		QC6	
3			QC1			QC3		QC4	QC5		QC6	
4			QC1			QC3		QC4	QC5		QC6	
5	QC1			QC2	QC3			QC4		QC5	QC6	
6	QC1			QC2	QC3			QC4		QC5	QC6	
7	QC1			QC2	QC3			QC4		QC5	QC6	
8		QC1		QC2	QC3			QC4		QC5		QC6
9		QC1		QC2	QC3			QC4		QC5		QC6
10		QC1		QC2	QC3			QC4		QC5		QC6
11		QC1		QC2	QC3			QC4		QC5		QC6
12		QC1		QC2			QC3	QC4				
13		QC1		QC2			QC3	QC4				
14		QC1		QC2			QC3	QC4				
15												

4.2. Case II: Large sample size (6 vessels, 12 quay cranes, and 24 bays)

Assume that six vessels have arrived and berthed in the terminal, then the load profile of all vessels are presented in Table 9. Twelve QCs are available with working rates (containers per hour) as shown in Table 10.

The optimization model for Case II includes 826 variables and 1234 constraints. Using Lingo 11.0 (Processor: Intel (R) Core (TM) i5-4210U; CPU @ 1.70GHz, 2.40 GHz, elapsed time = 17.19 minutes), the assigned QC for each bay are obtained as shown in Table 11, where it is found that the optimal makespan and number of operated containers are 15 hour and 3995, respectively. Further, the optimal satisfaction values on completion times are shown in Table 12. It is seen that the smallest satisfaction value is 83%, which is larger than the satisfaction threshold value. Furthermore, the number of containers operated by each QC is displayed in Table 13, where it is found that the largest number of loaded/unloaded containers (=525) corresponds to QC number 9.

Table 9. Berthing vessels' load profile for Case study II.

Input	Value					
Vessel number	1	2	3	4	5	6
Number of bays	3	5	4	4	4	4
Total number of bays for all vessels (*B*)	24					
Bay number (*b*)	1	2	3	4	5	6
Number of containers in each bay (ω_b)	100	200	125	150	250	150
Bay number (*b*)	7	8	9	10	11	12
Number of containers in each bay (ω_b)	100	175	125	200	250	150
Bay number (*b*)	13	14	15	16	17	18
Number of containers in each bay (ω_b)	200	120	100	200	175	150
Bay number (*b*)	19	20	21	22	23	24
Number of containers in each bay (ω_b)	125	250	175	200	100	225

Table 10. Working rates for QCs (Case II).

Quay crane number	Working rate (containers per hour)	Quay crane number	Working rate (containers per hour)
1	30	7	30
2	15	8	15
3	35	9	35
4	15	10	15
5	30	11	30
6	35	12	35

Variable	Final value
The optimal makespan ψ	15
The optimal number of operated containers $(\sum_{q=1}^{N} \zeta_q)$	3995

Vessel number	1			2					3			
Bay number	1	2	3	4	5	6	7	8	9	10	11	12
Processing time in hours	3.33	6.67	4.17	10	7.14	10	3.33	5	3.5	6.67	8.33	4.26
Completion time	14.17	6.67	10.83	15	10.71	13.57	15	13.33	3.57	15	8.3	4.29
Handling time	14.17			15					15			

Vessel number	4				5				6			
Bay number	13	14	15	16	17	18	19	20	21	22	23	24
Processing time in hours	6.67	8	6.67	5.71	5	4.28	8.33	8.33	5	6.67	2.86	6.43
Completion time	6.67	15	6.67	15	9.29	4.29	15	15	15	6.67	2.86	9.29
Handling time	15				15				15			

Table 11. Optimal results for QCASP model (Case II).

Table 12. The satisfaction on completion times for Case study II.

Bay, *b*	Satisfied completion times, SC_b	Actual completion times, C_b	δ^{+}_{b}	μ_b	Bay, *b*	Satisfied completion times, SC_b	Actual completion times, C_b	δ^{+}_{b}	μ_b
1	14	14.17	0.17	94%	13	6.67	6.67	0	100%
2	6.5	6.67	0.17	94%	14	15	15	0	100%
3	10.5	10.83	0.33	89%	15	6.5	6.67	0.17	94%
4	15	15	0	100%	16	15	15	0	100%
5	10.5	10.71	0.21	93%	17	9	9.29	0.29	90%
6	13.33	13.57	0.24	92%	18	4	4.29	0.29	90%
7	15	15	0	100%	19	14.5	15	0.5	83%
8	13	13.33	0.33	89%	20	15	15	0	100%
9	3.5	3.57	0.07	98%	21	15	15	0	100%
10	15	15	0	100%	22	6.5	6.67	0.17	94%
11	8	8.3	0.3	90%	23	2.5	2.86	0.36	88%
12	4	4.29	0.29	90%	24	9	9.29	0.29	90%

Table 13. Number of containers operated by each QC in case study II.

Quay crane number	Number of containers loaded/ unloaded (ζ_q)	Quay crane number	Number of containers loaded/ unloaded (ζ_q)
1	425	7	400
2	150	8	220
3	375	9	525
4	150	10	125
5	350	11	450
6	325	12	500

Finally, the optimal sequence of QCs operations on bays over the planning horizon for case study II is developed and then displayed in Table 14.

Sensitivity analysis on the arrangement and service rates of QCs was conducted and then obtained optimization results are summarized in Table 15. It is noted that the arrangement of high rates QCs at the sides results in the largest makespan (= 27.02 hours) but the largest minimal satisfaction level (= 88%). Although the base arrangement corresponds to the smallest minimal satisfaction level, however it provides the best optimal results on the remaining objective functions.

Table 14. Sequence of QCs operations in case study II.

Time period	Bay number											
	1	2	3	4	5	6	7	8	9	10	11	12
1		QC1		QC2		QC4			QC3		QC5	QC6
2		QC1		QC2		QC4			QC3		QC5	QC6
3		QC1		QC2		QC4			QC3		QC5	QC6
4		QC1		QC2		QC4			QC3		QC5	QC6
5		QC1		QC2	QC3	QC4		QC6			QC5	
6		QC1		QC2	QC3	QC4		QC6			QC5	
7		QC1		QC2	QC3	QC4		QC6			QC5	
8			QC1	QC2	QC3	QC4		QC6			QC5	
			QC1	QC2	QC3	QC4		QC6		QC7		
9			QC1	QC2	QC3	QC4	QC5	QC6		QC7		
10			QC1	QC2	QC3	QC4	QC5			QC7		
11			QC1		QC3		QC5			QC7		
12	QC1									QC7		
13	QC1									QC7		
14	QC1									QC7		
15										QC7		

Time period	Bay number											
	13	14	15	16	17	18	19	20	21	22	23	24
1	QC7		QC8			QC9	QC10			QC11	QC12	
2	QC7		QC8			QC9	QC10			QC11	QC12	
3	QC7		QC8			QC9	QC10			QC11	QC12	
4	QC7		QC8			QC9	QC10			QC11		QC12
5	QC7		QC8		QC9		QC10			QC11		QC12
6	QC7		QC8		QC9		QC10			QC11		QC12
7	QC7		QC8		QC9		QC10			QC11		QC12
8		QC8			QC9		QC10	QC11				QC12
9		QC8			QC9			QC11				QC12
10		QC8		QC9				QC11	QC12			
11		QC8		QC9				QC11	QC12			
12		QC8		QC9				QC11	QC12			
13		QC8		QC9				QC11	QC12			
14		QC8		QC9				QC11	QC12			
15		QC8		QC9				QC11				

Table 15. Optimal results of sensitivity analysis for Case II.

Crane	1	2	3	4	5	6	7	8	9	10	11	12	Makespan	Total containers	Minimum satisfaction
Base case	30	15	35	15	30	35	30	15	35	15	30	35	15	3995	83%
Ascending order	15	15	15	15	30	30	30	30	35	35	35	35	20	3995	88%
High rates at the middle	15	15	30	30	35	35	35	35	30	30	15	15	17.86	3995	86%
High rates at the sides	35	35	30	30	15	15	15	15	30	30	35	35	27.02	3995	88%

4.3. Case III: Large sample size (6 vessels, 12 quay cranes, and 40 bays)

Six vessels were assumed to be arrived and berthed in the terminal. The load profile of all vessels in this case is presented in Table 16. The optimization model for Case III includes 2074 variables and 3330 constraints. Using Lingo 11.0 (Processor: Intel (R) Core (TM) i5-4210U; CPU @ 1.70GHz, 2.40 GHz, elapsed time = 129.43 minutes). The optimal loaded/unloaded containers for Case III are displayed in Table 17, where it is noted that QC number 12 loaded/unloaded the largest number of containers (= 870).

The optimization results for Case III are then displayed in Table 18, where it is noted that the makespan and total loaded/unloaded containers are 16.52 hours and 5940, respectively.

The optimal sequence of QCs operations is then developed as shown in Table 19. Finally, the sensitivity analysis on the arrangement of QCs is conducted and then the results are shown in Table 20. Clearly, the best arrangement of QCs corresponds to the base case.

Table 16. Input data for Case III.

Input	Variable									
Vessel number	1		2	3		4		5	6	
Number of bays	6		7	6		6		8	7	
Total number of bays for all vessels (B)	40									
Bay number (b)	1	2	3	4	5	6	7	8	9	10
Number of containers in each bay (ω_b)	100	125	75	100	75	75	100	100	75	50
Bay number (b)	11	12	13	14	15	16	17	18	19	20
Number of containers in each bay (ω_b)	100	200	225	100	170	25	500	75	75	350
Bay number (b)	21	22	23	24	25	26	27	28	29	30
Number of containers in each bay (ω_b)	450	175	200	175	150	75	100	50	50	100
Bay number (b)	31	32	33	34	35	36	37	38	39	40
Number of containers in each bay (ω_b)	150	50	25	25	50	275	275	290	230	350

Table 17. Optimal QCs' loaded/unloaded containers for Case III.

Quay crane number	Number of containers loaded/ unloaded (ζ_q)	Quay crane number	Number of containers loaded/ unloaded (ζ_q)
1	475	7	700
2	500	8	275
3	695	9	300
4	175	10	100
5	500	11	550
6	800	12	870

Table 18. Optimization results for Case III.

Variable	Final value									
ψ	16.52									
$\sum_{q=1}^{N}\zeta_q$	5940									
Vessel number	1					2				
Bay number	1	2	3	4	5	9	10	11	12	13
ρ_b	3.33	6.67	8.33	4.29	5	4.17	5.71	2.86	4.29	6.67
C_b	3.33	7.81	16.52	8.64	8.64	6.14	7.36	4.52	5.98	9.02
Bay number	6	7	8	-	-	14	15	-	-	-
ρ_b	10	2.86	5.83	-	-	3.43	6.67	-	-	-
C_b	7.51	9.79	7.36	-	-	3.43	6.62	-	-	-
Handling time	16.52					9.02				
Vessel number	3					4				
Bay number	16	17	18	19	20	23	24	25	26	27
ρ_b	5.71	11.67	10	3.57	8.33	3.33	3.57	3.33	6.67	4.17
C_b	7.35	11.67	13.19	9.93	14.12	7.36	4.19	14.52	6.67	4.36
Bay number	21	22	-	-	-	28	-	-	-	-
ρ_b	5	5	-	-	-	4.29	-	-	-	-
C_b	8.33	9.62	-	-	-	14.52	-	-	-	-
Handling time	14.12					14.52				
Vessel number	5					6				
Bay number	29	30	31	32	33	35	36	37	38	39
ρ_b	8.33	10	2.86	5.83	4.17	5.71	4.29	5.71	3.43	2.86
C_b	14.12	14.02	5.54	7.95	6.71	9.02	4.29	5.71	3.43	8.57
Bay number	34	-	-	-	-	40	-	-	-	-
ρ_b	5.71	-	-	-	-	6.67	-	-	-	-
C_b	7.95	-	-	-	-	7.31	-	-	-	-
Handling time	14.12					9.02				

Table 19. Optimal QC operations sequence for Case III.

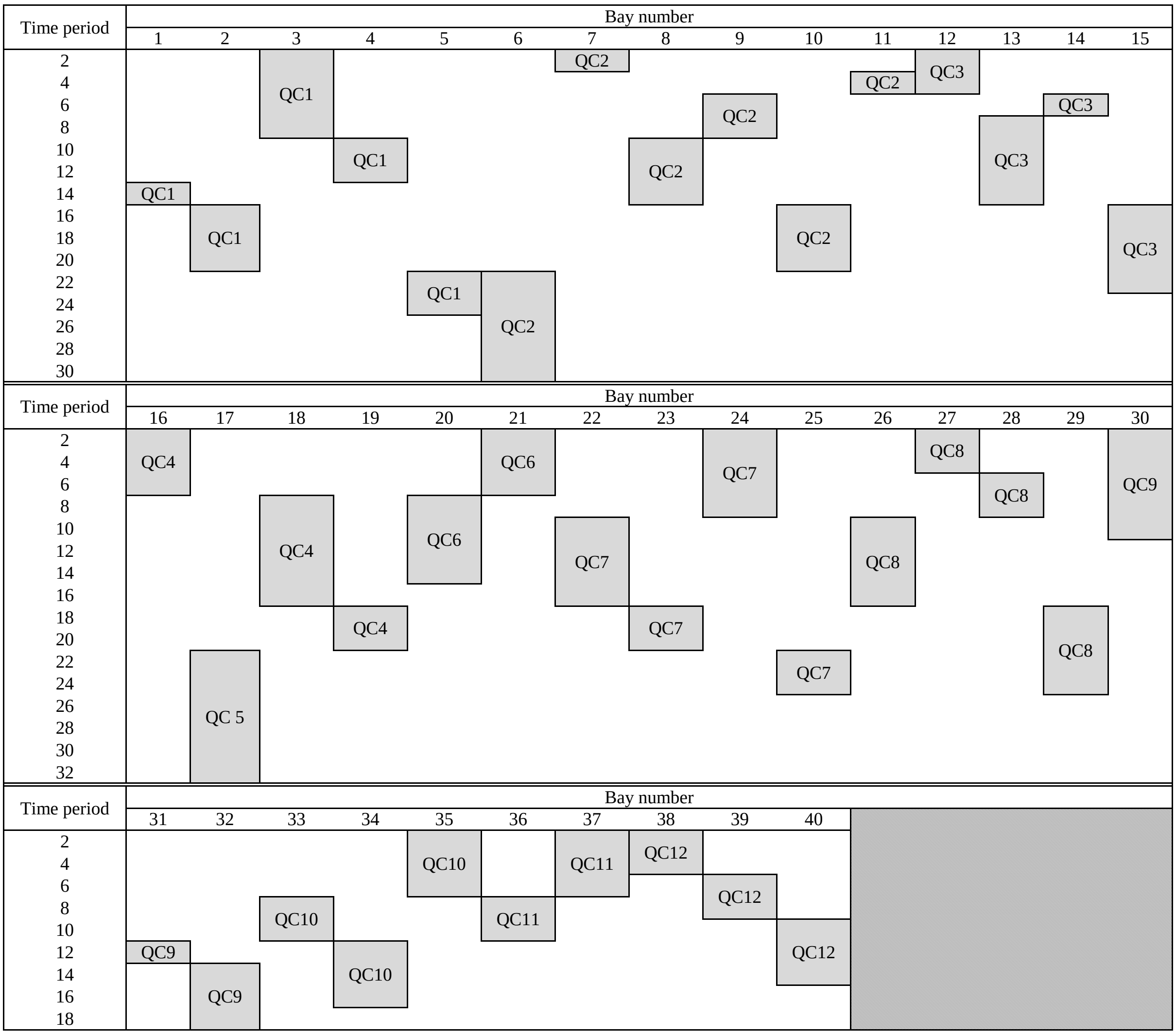

Table 20. Optimal results for sensitivity analysis for Case III.

Crane	1	2	3	4	5	6	7	8	9	10	11	12	Makespan	Total containers	Minimum satisfaction
Base	30	15	35	15	30	35	30	15	35	15	30	35	16.52	5940	81%
Ascending order	15	15	15	15	30	30	30	30	35	35	35	35	21.33	5940	84%
High rates in the middle	15	15	30	30	35	35	35	35	30	30	15	15	31.11	5940	80%
High rates in the sides	35	35	30	30	15	15	15	15	30	30	35	35	29.11	5940	83%

From the previous studies, it is found that:

- The proposed optimization model is found effective in scheduling and sequencing quay cranes operation to achieve stated multiple objectives. Moreover, it considers satisfaction levels on completion times.
- The proposed model can be utilized in determining the optimal quay cranes arrangements. It is found that having the same service rates for all quay cranes provides the best results.
- The proposed model considers more realistic constraints; such as, cranes crossing.

In these regards, the optimization model can provide valuable support to planning engineers in terminal in scheduling and sequencing quay cranes operations in a way that achieves terminal goals.

5. Conclusions

This research proposed an QCASP model to determine the optimal schedule and sequence of quay cranes operations on bays of vessels so that the makespan (latest completion time) of handling all bays is minimized and the utilization of all QCs in the marine container terminal is maximized. The proposed QCASP model was solved for three case studies. The assignment was made for bays of vessels assuming that all bays are ordered from left to right in ascending order. The locations of QCs obtained from solving the model exhibited that the non-crossing condition was not violated at any time, which is an essential requirement in real life as cranes are working on the same rail or track. Also, the cranes process their work on all bays without preemption, meaning that the QC finishes its job on the assigned bay before moving to another one. The results of the model also showed that the tasks on bays were distributed among the available QCs to better utilize them and achieving the shortest possible service time for all vessels so that the terminal could serve additional vessels. In conclusion, utilizing the QCASP model helps in making better utilization of the QCs and shortening the service period by the terminal, which consequently increases the terminal's throughput. Future research will consider developing a heuristic solution to solve large scale quay crane scheduling and sequencing problems.

References

[1] Tu-Chang, K. (1992). Development of a Container Terminal Simulation Model and its Application in and Analysis of Terminal 18, port of Seattle. *Ph.D. Thesis, University of Washington, Washington, 134-135*.

[2] Bierwirth, C. and Meisel, F. (2015). A follow-up survey of berth allocation and quay crane scheduling problems in container terminals. *European Journal of Operational Research*, 244 (3): 675-689.

[3] Agra, A. and Oliveira, M. (2018). MIP approaches for the integrated berth allocation and quay crane assignment and scheduling problem. *EuropeanJournal of Operational Research*, 264 (1): 138-148.

[4] Aras, N. Türkoğulları, Y. Taşkın, Z. C. and Altınel, K. (2014). Simultaneous optimization of berth allocation, quay crane assignment and quay crane scheduling problems in container terminals. *In: Helber, S. Breitner, M. Rösch, D. Schön, C. Graf von der Schulenburg, J.-M. Sibbertsen, P. Steinbach, M. Weber, S. Wolter, A. (Eds.), Operations Research Proceedings* 2012. (pp. 101-107). Springer, Cham.

[5] Hu, Zhi-Hua (2010). A quay crane assignment approach for berth allocation problem in container terminal. *Proceedings of the Third International Symposium on Intelligent Information Technology and Security Informatics (IITSI), Jian, China* 2-4 April, 2010, 17-21.

[6] Lee, D. H. and Qiu Wang, H. (2010). Integrated discrete berth allocation and quay crane scheduling in port container terminals. *Engineering Optimization*, 42 (8): 747-761.

[7] Lee, D. H. and Chen, J. H. (2010). An improved approach for quay crane scheduling with non-crossing constraints. *Engineering Optimization*, 42 (1): 1-15.

[8] Zeng, Q. Yang, Z. and Hu, X. (2011). Disruption recovery model for berth and quay crane scheduling in container terminals. *Engineering Optimization*, 43 (9): 967-983.

[9] Chung, S. H. and Chan, F. T. (2013). A workload balancing genetic algorithm for the quay crane scheduling problem. *International Journal of Production Research*, 51(16): 4820-4834.

[10] Diabat, A. and Theodorou, E. (2014). An integrated quay crane assignment and scheduling problem. *Computers & Industrial Engineering*, 73, 115-123.

[11] Fu, Y. M. Diabat, A. and Tsai, I. T. (2014). A multi-vessel quay crane assignment and scheduling problem: Formulation and heuristic solution approach. Expert *Systems with Applications*, 41 (15): 6959-6965.

[12] Al-Dhaheri, N. and Diabat, A. (2015). The quay crane scheduling problem. *Journal of Manufacturing Systems*, 36, 87-94.16

[13] Msakni, M. K. Al-Salem, M. Diabat, A. Rabadi, G. and Kotachi, M. (2016). An integrated quay crane assignment and scheduling problem using branch-and- price. *Proceedings of the IEEE International conference on computational science and computational intelligence* (CSCI 2016), Las Vegas, Nevada, USA 15-17 December, 2016, 1286-1291.

[14] Chang, D. Fang, T. and Fan, Y. (2017). Dynamic rolling strategy for multi-vessel quay crane scheduling. *Advanced Engineering Informatics*, 34, 60-69.

[15] Chu, Y. Zhang, X. and Yang, Z. (2017). Multiple quay cranes scheduling for double cycling in container terminals. *PLOS ONE*, 12(7): e0180370.

[16] Al-Refaie, A., Haddadin, M., Qabaja, A. (2019). Optimal parameters and tolerances in concurrent product and process design using simulation and fuzzy goal programming.*International Journal of Quality and Reliability Management*, 37(2), 372–392.

[17] Al-Refaie, A., Musallam, A. (2019). Using mixed goal programming to optimize performance of extrusion process for multiple responses of irrigation pipes. *Proceedings of the Institution of Mechanical Engineers, Part E: Journal of Process Mechanical Engineering*, 233(2), 412–424.

[18] Al-Refaie, A., Bani Domi, G., Abdullah, R. (2019). A fuzzy goal programming-regression approach to optimize process performance of multiple responses under uncertainty. *International Journal of Management Science and Engineering Management*, 14(1), 20–32.

[19] Al-Refaie, A. (2015). Optimizing multiple quality responses in the Taguchi method using fuzzy goal programming: Modeling and applications. *International Journal of Intelligent Systems*, 30(6), 651–675.

[20] Al-Refaie, A., Judeh, M., Chen, T. (2018). Optimal multiple-period scheduling and sequencing of operating room and intensive care unit. *Operational Research*, 18(3), 645–670.

JJMIE

Volume 15, Number 2, June. 2021
ISSN 1995-6665
Pages 169 - 180

Jordan Journal of Mechanical and Industrial Engineering

A Rough Multi-Attributive Border Approximation Area Comparison Approach for Arc Welding Robot Selection

Subham Agarwal[a], Santonab Chakraborty[b], Kanika Prasad[c], Shankar Chakraborty[a*]

[a]Department of Production Engineering, Jadavpur University, Kolkata, West Bengal, India

[b]Industrial Engineering and Management Department, Maulana Abul Kalam Azad University of Technology, West Bengal, India

[c]Department of Production and Industrial Engineering, National Institute of Technology, Jamshedpur, India

Received July 3 2020 Accepted May 15 2021

Abstract

In the present day, automated industries, such as arc welding robots have found immense applications in manufacturing of steel furniture, automobile components, agricultural machineries etc. Selection of the most appropriate robot for a specific welding application can be treated as a multi-criteria decision making problem where the best alternative needs to be identified with respect to a set of conflicting evaluation criteria. In this paper, rough numbers are integrated with multi-attributive border approximation area comparison (MABAC) approach for solving an arc welding robot selection problem. The opinions of five decision makers are aggregated together using rough numbers to avoid subjectivity in the decision making process, while MABAC method is employed to rank the candidate alternatives and choose the best robot for the given welding application. The criteria weights are determined using rough entropy method, which reveals that welding performance and payload are the two most important arc welding robot selection criteria, followed by cost of the robot. The application of rough-MABAC method identifies robot A6 as the most suitable choice and robot A2 as the least preferred option.

Keywords: Arc welding robot; MABAC method; Rank; Rough set theory; Selection;

1. Introduction

According to ISO 8373:2012, an industrial robot can be defined as 'an automatically controlled, reprogrammable, multipurpose manipulator programmable in three or more axes, which can be either fixed in place or mobile for use in industrial automation applications'. Due to their ability to perform dangerous, monotonous and repetitive tasks with unswerving precision and accuracy, industrial robots are now of increasing demands in diverse manufacturing applications under challenging environments. As their various functionalities are automatically controlled by programmed software, they can be operated round the clock while releasing the occupied manpower to other activities, and relieving the manpower from those activities which may cause physical strain and injury to them. Their implementation thus increases productivity and profitability of the present day manufacturing industries while reducing delivery time and improving work environment [1, 2].

Although the primary task of industrial robots is to move materials from one place to another, they can also be adopted for carrying out other programmed tasks in different industrial settings, like welding (arc and spot), machine loading and unloading, spray painting, assembly operation, picking, packing and palletizing, machining and cutting operations, etc. At the same time, the number of industrial robot manufacturers has also shown an increasing trend, each offering a wide range of robots to fulfil the customers' end requirements. Thus, with the availability of different types and models of industrial robots having separate specifications, it now becomes a difficult and challenging assignment to the decision makers to identify the most appropriate robot to perform the specified industrial operation. This robot selection task now becomes more and more intricate as diverse complex features and facilities are being continuously added to the robots by different manufacturers. Changing manufacturing environment, investment plan, product design and manufacturing system often influence the industrial robot selection decision. Thus, selection of the best-suited industrial robot having the desired functional ability can be treated as a multi-criteria decision making (MCDM) problem [3]. It has been often noticed that an ill-selected robot may adversely affect the productivity and profitability of a manufacturing organization. The application of an MCDM method for robot selection basically consists of three stages, i.e. identification and assessment of various robot alternatives and evaluation criteria, determination of the criteria weights and prioritization of the candidate robots. Presence of subjective evaluation criteria expressed in linguistic terms, mutually conflicting criteria and large number of selection criteria make the industrial robot selection task more and more difficult. It can be interestingly noted that Bhangale et al. [4] recognized a total of 83 criteria for performance appraisal of industrial robots.

While applying any MCDM method for identification of the most apposite robot for a given industrial application, valuable opinions of the decision makers/experts are often

*Corresponding author e-mail: s_chakraborty00@yahoo.co.in

sought to evaluate the performance of the candidate robots with respect to various criteria. These expert opinions are subjectively expressed using linguistic terms and they also considerably vary from one expert to another. These varied judgements of the participating experts need to be aggregated to arrive at the final selection decision. There also exists ambiguity and uncertainty in evaluating weights of various evaluation criteria. In this paper, a maiden endeavour is put forward to evaluate the performance of arc welding robots and identify the best choice for a given task while applying rough multi-attributive border approximation area comparison (MABAC) approach. In order to avoid any biasness in the decision making process, rough entropy method is implemented to determine the priority weights of the considered selection criteria. Arc welding is a joining process which utilizes an electric arc between an electrode and a metal base. Arc welding robots employ this process to generate intense heat to the metal at a joint, causing the metal to melt and intermix. There are several advantages of arc welding robots over the manual welders. They can provide consistent performance throughout the weld, and have extremely high repeatability, causing high quality welds. They can also save the manual welders from toxic fumes and risk of arc burns. They can significantly reduce cycle time and increase productivity. It has been observed that arc welding robots have typically about 75-80% arc-on time, and for larger parts with long seams, they can have more than 95% arc-on time. On the other hand, human welders have less than 50% arc-on time and with fatigue, it may further decrease as the shift progresses. Arc welding robots have found wide ranging applications in manufacturing of steel furniture, automobile components, agricultural machineries etc.

This paper is organized as follows: After providing a brief introduction on the need of arc welding robot selection in Section 1, Section 2 presents a review on various MCDM methods applied for robot selection. Section 3 highlights the mathematics behind rough set theory and MABAC approach. An arc welding robot selection problem is solved in Section 4. Discussions are provided in Section 5 and conclusions are drawn in Section 6.

2. Literature review

It can be revealed that selection of industrial robots for varying applications has already caught the attention of the researchers since several years. Various MCDM techniques, mainly in the form of weighted sum method (WSM), weighted product method (WPM), simple multi-attribute rating technique (SMART), weighted aggregated sum product assessment (WASPAS), multi-objective optimization on the basic of ratio analysis (MOORA), analytic hierarchy process (AHP), technique for order preference by similarity to the ideal solution (TOPSIS), evaluation based on distance from average solution (EDAS), preference ranking organization method for enrichment evaluation (PROMETHEE), TOmada de Decisao Interativa Multicriterio (TODIM) (an acronym in Portuguese for interative multi-criteria decision making) etc. have been adopted for identifying suitable robots for performing simple pick-n-place operations. Table 1 presents a review of the existent literature on industrial robot selection along with the number of alternative robots, evaluation criteria and MCDM techniques employed for solving those problems.

Those MCDM techniques have been deployed under the circumstances where the performance of the alternative robots with respect to various evaluation criteria can be numerically expressed in absolute units. On the other hand, it can also be noticed that some of those MCDM techniques have been integrated with different models of fuzzy set theory, like interval type-2 fuzzy sets, interval-valued hesitant fuzzy theory, cloud model etc. to quantify the qualitative assessment of different robot selection criteria under group decision making environment. Those fuzzy models usually convert the crisp information into fuzzy values to deal with the vagueness present in the decision making process. In fuzzy set theory, identification of the appropriate membership functions mainly depends of the subjective judgments of the concerned decision makers. Auxiliary information is also required in most of the fuzzy models. The introduction of rough numbers instead of fuzzy numbers can more efficiently address the subjectivity and ambiguity in the data because they mainly confide in the original data without any additional information. Rough numbers are able to deal with the vagueness and uncertainty in the data with the help of boundary region of a set instead of membership functions [20-23]. Application of rough numbers in decision making does not require any preliminary or additional information about the primary data (like, probability distributions, membership functions or possibility value). It has been pointed out that the integration of rough numbers with MCDM methods would provide more acceptable and reliable results while solving complex decision making problems [24, 25]. The above-cited literature review also reveals the fact that the application of MCDM methods for solving welding robot selection problems is really scarce. Thus, in this paper, rough numbers are harmonized with MABAC method to identify the most apposite industrial robot for performing arc welding operations in real time manufacturing environment. The rough-MABAC method also identifies the positive and negative attributes for each of the arc welding robot alternatives. This integrated approach would classify the competing robot alternatives into efficient (best performers) and inefficient (underperformers) ones, and would also identify the relative strengths of the best performing robots and weaknesses of the underperforming robots. It would finally rank the competing arc welding robots from the best to the worst. In order to avoid subjectivity in the decision making process, the priority weights of the considered robot selection criteria are determined using rough entropy method. Compared to other subjective weighting models, like best worst method (BWM), step-wise weight assessment ratio analysis (SWARA), factor relationship (FARE), level based weight assessment (LBWA), full consistency method (FUCOM) etc., the major advantage of entropy weighting method is the avoidance of interference of human factors during estimation of criteria weights, thereby increasing objectivity of weight measurement results [26]. Based on the disorder degree of a system (randomness), it can extract valuable information using the data provided. In a decision matrix, when the difference in performance scores of the candidate alternatives with respect to a specific criterion is high, the corresponding entropy would be low providing more useful information and the weight of that criterion would be set as high. On the other hand, if the difference is small, the entropy is high and the relative weight would be low. Thus, the application of rough-MABAC method would help a manufacturing organization in arriving at the most proactive decision with respect to robot selection for a specific welding task. Based on the identified research gap, this paper contributes to the followings:

1. to assess the relative performance of 14 arc welding robot alternatives with respect to 12 evaluation criteria based on the valued opinions of five decision makers/experts using rough numbers,
2. to propose the application of MABAC method to rank all the alternative robots from the best to the worst based on their calculated performance scores,
3. to segregate all the alternative robots into best performing (efficient) and underperforming (inefficient) clusters using their corresponding criteria function values,
4. to identify the relative strengths and weaknesses of each of the robots with respect to all the evaluation criteria so that the concerned manufacturers can modify/upgrade the existing specifications of the underperforming robots to make them more comparable and appropriate for a specific welding task, and
5. to prove the accuracy of the ranking results derived using rough-MABAC method against other popular rough MCDM techniques.

Table 1. List of alternative robots, evaluation criteria and MCDM techniques considered by the past researchers

Sl. No.	Author(s)	Number of alternative robots	Evaluation criteria	MCDM technique(s)
1.	Sen et al. [5]	7, 14	Velocity, load capacity, cost, repeatability, maximum tip speed, memory capacity, manipulator reach, vendor's service quality, programming flexibility	PROMETHEE II
2.	Ghorabaee [6]	8	Inconsistency with infrastructure, man-machine interface, programming flexibility, vendor's service contract, supporting channel partner's performance, compliance, stability	Fuzzy VIKOR with interval type-2 fuzzy sets
3.	Gitinavard et al. [7]	3	Man-machine interface, programming flexibility, vendor's service contract, load capacity, positioning accuracy, cost	Interval-valued hesitant fuzzy distance-based group decision model
4.	Karande et al. [8]	7,12	Load capacity, maximum tip speed, repeatability, memory capacity, manipulator reach, cost, handling coefficient, velocity	WSM, WPM, WASPAS, MOORA, MULTIMOORA
5.	Sen et al. [9]	7	Load capacity, repeatability, maximum tip speed, memory capacity, manipulator reach, man-machine interface, programming flexibility, vendor's service contract, positioning accuracy, safety, environmental performance, reliability, maintainability	Fuzzy PROMETHEE
6.	Sen et al. [10]	7	Load capacity, repeatability, maximum tip speed, memory capacity, manipulator reach, velocity, cost	TODIM
7.	Xue et al. [11]	3	Man-machine interface, programming flexibility, vendor's service contract, cost, load capacity, positioning accuracy	Linguistic MCDM approach
8.	Breaz et al. [12]	3	Load capacity, reach, weight, repeatability, power consumption, dexterity, service	AHP
9.	Wang et al. [13]	4	Inconsistency with infrastructure, man-machine interface, programming flexibility, vendor's service contract, supporting channel partner's performance, compliance, stability	Cloud TODIM
10.	Liu et al. [14]	3	Freedom, work space, velocity, load capacity, accuracy, warranty period, protection class	Linguistic MCDM model
11.	Yalçin and Uncu [15]	3, 5, 7	Load capacity, repeatability, vertical reach, degrees of freedom, maximum tip speed, memory capacity, manipulator reach, man-machine interface, programming flexibility, vendor's service contract	EDAS
12.	Nasrollahi et al. [16]	4	Cost, load capacity, repeatability, man-machine interface, programming flexibility, velocity ratio	Fuzzy BWM-PROMETHEE
13.	Suszynski and Rogalewicz [17]	5	Lifting capacity, weight, working range, repeatability, range of movement, price, velocity	Fuzzy AHP, fuzzy TOPSIS, SMART
14.	Zhang et al. [18]	3	Price, energy consumption, external configuration, accuracy, speed, work raio, programming difficulty	AHP, TOPSIS
15.	Rashid et al. [19]	5	Load capacity, repeatability, velocity ratio, degree of freedom	BWM-EDAS
16.	This paper	14	Payload, horizontal reach, vertical reach, repeatability, weight, power rating, cost, flexibility, safety, welding performance, maintainability, ease of programming	Rough-MABAC

3. Methods

3.1. Rough set theory

A rough number can be expressed with respect to rough boundary interval, comprising lower limit and upper limit [27]. Suppose, in the universe, U with all the objects, Y is an arbitrary object of U, and R is a set of t classes $\{G_1, G_2, ..., G_t\}$ encompassing all the objects in U. If these t classes are arranged as $\{G_1 < G_2 < ... < G_t\}$, then $\forall Y \in U, G_q \in R$, $1 \le q \le t$, where $R(Y)$ represents the class to which the object belongs. The lower approximation $(\underline{Apr}(G_q))$, upper approximation $(\overline{Apr}(G_q))$ and boundary region $(Bnd(G_q))$ of class G_q can be denoted as follows:

$$\underline{Apr}(G_q) = \{Y \in U / R(Y) \le G_q\} \tag{1}$$

$$\overline{Apr}(G_q) = \{Y \in U / R(Y) \ge G_q\} \tag{2}$$

$$\begin{gathered} Bnd(G_q) = \{Y \in U / R(Y) \ne G_q\} = \\ \{Y \in U / R(Y) > G_q\} \cup \{Y \in U / R(Y) < G_q\} \end{gathered} \tag{3}$$

Then G_q can be defined as rough number ($RN(G_q)$), which can be expressed by its corresponding lower limit $(\underline{Lim}(G_q))$ and upper limit $(\overline{Lim}(G_q))$, as shown below [25]:

$$\underline{Lim}(G_q) = \frac{1}{M_L} \sum \left\{Y \in \underline{Apr}(G_q)\right\} R(Y) \tag{4}$$

$$\overline{Lim}(G_q) = \frac{1}{M_U} \sum \left\{Y \in \overline{Apr}(G_q)\right\} R(Y) \tag{5}$$

$$RN(G_q) = \left[\underline{Lim}(G_q), \overline{Lim}(G_q)\right] = \left[x_{ij}^L, x_{ij}^U\right] \tag{6}$$

where M_L and M_U are the numbers of objects contained in $(\underline{Apr}(G_q))$ and $(\overline{Apr}(G_q))$ respectively, and x_{ij}^L and x_{ij}^U are the lower evaluation and upper evaluation limits of j^{th} criterion with respect to i^{th} alternative respectively.

The difference between the upper and lower evaluation limits is known as the rough boundary interval.

$$IRBnd(G_q) = \overline{Lim}(G_q) - \underline{Lim}(G_q) \tag{7}$$

More vagueness present in the data has a larger rough boundary interval, whereas, more preciseness is represented by the smaller value of this interval.

3.2. Rough number-based entropy method

While solving any MCDM problem, determination of the weights (relative importance) of the considered criteria always plays an important role. Any variation in the criteria weights may result in different ranking orders of the candidate alternatives. It has already been mentioned that the conventional approaches of criteria weight measurement, like AHP, BWM, LBWA, SWARA, FUCOM etc, suffer from a major disadvantage of being affected by the subjective preferences of the decision makers. In order to avoid this subjectivity in human judgements, information entropy theory has now become a well-accepted approach where the estimation of the criteria weights mainly depends on the randomness in the data itself. Thus, rough set theory is combined here with entropy theory to aggregate the individual judgements of the decision makers while estimating the weights of various arc welding robot selection attributes. Determination of the criteria weights based on rough entropy method has the following procedural steps [28]:

- *Step 1*: For k number of decision makers, k number of decision matrices can be developed, each representing the performance of candidate arc welding robots with respect to different attributes under consideration. Based on the information of those decision matrices and rough set theory, the following decision matrix (X) can be formulated:

$$X = \begin{bmatrix} (x_{11}^L, x_{11}^U) & (x_{12}^L, x_{12}^U) & \cdots & (x_{1n}^L, x_{1n}^U) \\ (x_{21}^L, x_{21}^U) & (x_{22}^L, x_{22}^U) & \cdots & (x_{2n}^L, x_{2n}^U) \\ \vdots & \vdots & \ddots & \vdots \\ (x_{m1}^L, x_{m1}^U) & (x_{m2}^L, x_{m2}^U) & \cdots & (x_{mn}^L, x_{mn}^U) \end{bmatrix} \tag{8}$$

where x_{ij} ($1 \le i \le m$, $1 \le j \le n$) is the performance score of i^{th} alternative with respect to j^{th} criterion, m is the number of alternatives and n is the number of attributes.

- *Step 2*: From the initial rough decision matrix (X), the corresponding normalized rough decision matrix, $N = ([r_{ij}^L, r_{ij}^U])_{m \times n}$ is now developed. For this normalization process, any of the following two equations can be deployed depending on the type of the considered criterion.

  For beneficial criteria:

$$r_{ij}^L = \left[x_{ij}^L - \min(x_{ij}^L)\right] / \left[\max(x_{ij}^U) - \min(x_{ij}^L)\right] \tag{9}$$

(for $1 \le i \le m$, $1 \le j \le n$)

$$r_{ij}^U = \left[x_{ij}^U - \min(x_{ij}^L)\right] / \left[\max(x_{ij}^U) - \min(x_{ij}^L)\right] \tag{10}$$

For non-beneficial criteria:

$$r_{ij}^L = \left[\max(x_{ij}^U) - x_{ij}^U\right] / \left[\max(x_{ij}^U) - \min(x_{ij}^L)\right]$$

(for $1 \le i \le m$, $1 \le j \le n$) (11)

$$r_{ij}^U = \left[\max(x_{ij}^U) - x_{ij}^L\right] / \left[\max(x_{ij}^U) - \min(x_{ij}^L)\right] \tag{12}$$

- *Step 3*: *The* entropy of the rough numbers is now computed using the following expressions:

$$E_j^L = -k \sum_{i=1}^{m} f_{ij}^L \ln(f_{ij}^L) \tag{13}$$

$$E_j^U = -k \sum_{i=1}^{m} f_{ij}^U \ln(f_{ij}^U) \tag{14}$$

where $f_{ij}^L = r_{ij}^L / \sum_{i=1}^{m} r_{ij}^U$, $f_{ij}^U = r_{ij}^U / \sum_{i=1}^{m} r_{ij}^U$, $k = 1/\ln(n)$, supposing $f_{ij} = 0$, $f_{ij} \ln f_{ij} = 0$.

Now, the weight for j^{th} criterion can be estimated as follows:

$$w_j^L = \frac{1 - E_j^U}{\sum_{j=1}^{n} \left(1 - E_j^U\right)} \tag{15}$$

$$w_j^U = \frac{1-E_j^L}{\sum_{j=1}^{n}\left(1-E_j^L\right)} \quad (16)$$

where w_j^L and w_j^U respectively represent the lower and upper limits of the entropy weight for j^{th} criterion.

3.3. Rough number-based MABAC method

The implementation procedure of rough number-based MABAC approach for identifying the best alternative based on a set of conflicting criteria has the following steps [29-34]:

- *Step 1*: *Using* the normalized rough decision matrix and rough entropy weights, the corresponding weighted normalized rough decision matrix (*V*) is formulated.

$$\begin{cases} V = \left(\left[v_{ij}^L, v_{ij}^U\right]\right)_{m\times n} \\ v_{ij}^L = w_j^L\left(n_{ij}^L+1\right) \\ v_{ij}^U = w_j^U\left(n_{ij}^U+1\right) \end{cases} \quad (17)$$

where $[n_{ij}^L, n_{ij}^U]$ are the elements of the normalized rough decision matrix (*N*) and $[w_j^L, w_j^U]$ are the rough entropy weights of j^{th} criterion.

- *Step 2*: Based on the geometric aggregation procedure for interval numbers, the border approximation area (BAA) for each criterion is calculated as follows:

$$\begin{cases} G = [g_1, g_2, ..., g_n], \text{ where } g_j = [g_j^L, g_j^U] \\ g_j^L = \left(\prod_{i=1}^{m} v_{ij}^L\right)^{1/m} \\ g_j^U = \left(\prod_{i=1}^{m} v_{ij}^U\right)^{1/m} \end{cases} \quad (18)$$

- *Step 3*: Calculate the distances of the candidate alternatives from the BAA to obtain the related distance matrix (*Q*) while employing the Euclidean distance operator for interval numbers.

$$Q = (q_{ij})_{m\times n} = ([q_{ij}^L, q_{ij}^U])_{m\times n}$$

(19)

where for beneficial criteria:

$$q_{ij} = \begin{cases} d_E(v_{ij}, g_j) & \text{if } RN(v_{ij}) > RN(g_j) \\ -d_E(v_{ij}, g_j) & \text{if } RN(v_{ij}) < RN(g_j) \end{cases}$$

(20)

For non-beneficial criteria:

$$q_{ij} = \begin{cases} -d_E(v_{ij}, g_j) & \text{if } RN(v_{ij}) > RN(g_j) \\ d_E(v_{ij}, g_j) & \text{if } RN(v_{ij}) < RN(g_j) \end{cases}$$

(21)

and

$$d_E(v_{ij}, g_j) = \sqrt{(v_{ij}^L - g_j^U)^2 + (v_{ij}^U - g_j^L)^2}$$ for beneficial criteria (22)

$$d_E(v_{ij}, g_j) = \sqrt{(v_{ij}^L - g_j^L)^2 + (v_{ij}^U - g_j^U)^2}$$

for non-beneficial criteria (23)

where $[g_j^L, g_j^U]$ is the BAA for j^{th} criterion.

Now, if $q_{ij} = 0$, an alternative A_i belongs to the BAA (*G*); if $q_{ij} > 0$, it belongs to upper approximation area (G^+), and if $q_{ij} < 0$, it belongs to lower approximation area (G^-). The ideal alternative (A^+) should be positioned in the upper approximation area (G^+), and location of the anti-ideal alternative (A^-) should be in the lower approximation area (G^-). An alternative (A_i) with as many criteria belonging to the upper approximation area (G^+) should be treated as the best choice.

- *Step 4*: For *determination* of the criteria function values (final scores) of the alternatives, the distances of the alternatives from the BAA vector are added together.

$$S(A_i) = \sum_{j=1}^{n} q_{ij}, \; i = 1,2,...,m \quad (24)$$

The candidate alternatives are now ranked based on the descending values of $S(A_i)$. Hence, the alternative having the highest $S(A_i)$ value is obviously the best suited option.

4. Selection of an arc welding robot

Due to wide ranging applications of arc welding robots in various manufacturing industries, it becomes an ardent need for the decision makers to evaluate the performance of the available robots with respect to some of the important criteria, and to identify the most apposite robot for a said welding application. As the deployment of an arc welding robot is a capital intensive task, any wrong decision during the robot procurement and installation stage may negatively affect the productivity and goodwill of the manufacturing organizations. While selecting an arc welding robot, the judgments of the individual decision makers (experts) are often predisposed. Hence, in order to avoid this biasness in the decision making process, the opinions of five decision makers are sought. These decision makers, engaged in an automobile industry and having more than 10 years of industrial experience, have enough expertise in joining/welding processes, operation and control of arc welding robots, robot programming, part/product geometry, safety and environmental hazards during the welding operation. Each of those decision makers has to assess the performance of 14 candidate arc welding robots with respect to 12 evaluation criteria based on a 9-point scale (where 1 = very low, 3 = low, 5 = moderate, 7 = high and 9 = very high). For this arc welding robot selection problem, the considered evaluation criteria are payload (PL), horizontal reach (HR), vertical reach (VR), repeatability (R), weight (W), power rating (PR), cost (C), flexibility (FL), safety (S), welding performance (WP), maintainability (M) and ease of programming (EP). Amongst these 12 evaluation criteria, PL, HR, VR, R, FL, S, WP, M and EP are beneficial attributes, always requiring their higher values. On the other hand, W, PR and C are non-beneficial criteria where lower values are preferred. Performance of an arc welding robot by the concerned decision makers is usually appraised based on the manufacturers' brand name, service facility provided, features in the robot, complexity of the welding operation to be performed, compactness of the robot etc. Payload is the maximum weight that a robot can lift and manipulate over a specified working space with ease and desired repeatability. It includes weight of the end arm tooling with the necessary welding attachments. Horizontal reach can be defined as the distance from the centre of the robot to the fullest extension of its arm in horizontal direction. On the other hand, vertical reach is the maximum work envelope in vertical direction where a robotic arm with the welding attachments can reach. Repeatability is the measure of variability of a robotic arm's positioning under the specified conditions of load, temperature etc. Weight is the overall weight of an arc welding robot. It plays a crucial role when there is a load constraint in the job floor. Power rating signifies the amount of power required by a robot for performing a seamless welding operation. Cost of an arc welding robot consists of the expenditure incurred during its procurement and installation. Flexibility is the ability of an arc welding robot to perform a variety of different welding tasks regardless of the size, shape or position of the job. Safety is determined on the basis of various safety features present in an arc welding robot to allow safe human-robot interaction. Welding performance indicates the quality and consistency of the welding operation by a robot. Maintainability represents the ease with which it can be ensured that the robots are welding/functioning properly and can be repaired in case of any failure/malfunction. Ease of programming is an important feature for an arc welding robot through which it is instructed to perform a sequence of steps. The robot can be easily reprogrammed to perform a different set of steps as and when desired.

Thus, based on the evaluation of the candidate arc welding robots with respect to 12 assessment criteria by the five decision makers, five decision matrices are developed. Table 2 shows one such decision matrix representing the preference of the first decision maker while evaluating the performance of the considered arc welding robots. Other four decision matrices are also similarly formed. Thus, the first decision maker assesses the performance of robot A_1 with PL = very low (1), HR = very low (1), VR = very low (1), R = very low (1) and so on. Rough set theory is now applied to aggregate the individual judgments of the five decision makers. For example, the set of performance ratings of robot A_1 with respect to PL as evaluated by the five decision makers is represented as x_{11} = {very low, very low, low, low, very low} = {1, 1, 3, 3, 1}. Using Eqs. (4)-(6), this set of subjective linguistic information is transformed into the corresponding rough numbers, as explained below:

For the element $\tilde{x}_{11}$ = {1, 1, 3, 3, 1}

$$\underline{Lim}(1) = 1.00, \overline{Lim}(1) = \frac{1}{5}(1+1+3+3+1) = 1.80$$

$$\underline{Lim}(3) = \frac{1}{5}(1+1+3+3+1) = 1.80, \overline{Lim}(3) = 3.00$$

$$RN(x_{11}^1) = [1.00, 1.80], RN(x_{11}^2) = [1.00, 1.80],$$
$$RN(x_{11}^3) = [1.80, 3.00], RN(x_{11}^4) =$$
$$[1.80, 3.00], RN(x_{11}^5) = [1.00, 1.80]$$

$$x_{11}^L = \frac{x_{11}^1 + x_{11}^2 + x_{11}^3 + x_{11}^4 + x_{11}^5}{5} =$$
$$\frac{1.00 + 1.00 + 1.80 + 1.80 + 1.00}{5} = 1.32$$

$$x_{11}^U = \frac{x_{11}^1 + x_{11}^2 + x_{11}^3 + x_{11}^4 + x_{11}^5}{5} =$$
$$\frac{1.80 + 1.80 + 3.00 + 3.00 + 1.80}{5} = 2.28$$

Based on the above-demonstrated calculations, all the entries from the decision matrices of the five individual decision makers are converted into a rough decision matrix, $X = ([x_{ij}^L, x_{ij}^U])_{14\times12}$, as provided in Table 3. It is worthwhile to mention here that among the 12 evaluation criteria, some are beneficial (larger-the-better) in nature and some are non-beneficial (smaller-the-better) attributes. Thus, while taking into consideration both these types of attributes, the rough decision matrix is now normalized applying Eqs. (9)-(12). The corresponding normalized rough decision matrix $N = ([r_{ij}^L, r_{ij}^U])_{14\times12}$ is shown in Table 4. Similarly, while employing Eqs. (13)-(16), the rough entropy weights for the 12 arc welding robot selection criteria are estimated, as exhibited in Table 5. Amongst these 12 robot selection criteria, WP and PL are observed to have maximum rough entropy weights, followed by C and S. On the other hand, WP is identified having the maximum rough boundary interval, where the five decision makers have opined quite differently.

After developing the normalized rough decision matrix and calculating the rough entropy weights for the considered assessment criteria, the corresponding weighted normalized rough decision matrix is formulated, as shown in Table 6. This matrix is developed by multiplying rough entropy weights with the elements of the normalized rough decision matrix, using Eq. (17). Now, rough-MABAC method is implemented to identify the best arc welding robot from a set of 14 candidate alternatives. Using the geometric aggregation operator for rough numbers and Eq. (18), the related border approximation area (BAA) for each of the robot selection criteria is computed, as presented in Table 7. For example,

g_1^L =
(0.038×0.040×0.048×0.069×0.046×0.056×0.037×0.039×0.036×0.056×0.036×0.036×0.055×
0.036)$^{(1/14)}$ = 0.0439

g_1^U =
(0.447×0.469×0.548×0.757×0.531×0.627×0.436×0.497×0.409×0.627×0.409×0.428×0.640×
0.412)$^{(1/14)}$ = 0.5070

g_1 = [0.0439,0.5070]

The distances of all the arc welding robot alternatives from the BAA are now calculated to form the corresponding distance matrix, Q, while employing the rough-valued Euclidean distance operator of Eqs. (20)-(23). This distance matrix is provided in Table 8, from which the final score, $S(A_i)$ for each of the arc welding robots is computed. The $S(A_i)$ values are then arranged in descending order to provide a ranking list of the robots from the best to the worst. For example,

S(AR700) = –0.6186 – 0.3759 – 0.4031 – 0.4030 – 0.0822 – 0.0300 + 0.0953 + 0.5566 – 0.5303 + 0.9243 + 0.6042 + 0.6022 = 0.3394

S(AR900) = –0.6321 – 0.3759 – 0.4137 – 0.4030 – 0.0899 – 0.0300 + 0.0953 – 0.4789 + 0.6156 – 0.7685 + 0.6101 + 0.6085 = –1.2624

The final scores of all the 14 arc welding robot alternatives are exhibited in Table 9. Based on these scores as computed using rough-MABAC method, it can be revealed that A_6 robot occupies the top position in the ranking list, followed by robot A_3. The entire ranking list is obtained as $A_6 \rightarrow A_3 \rightarrow A_{13} \rightarrow A_{10} \rightarrow A_5 \rightarrow A_9 \rightarrow A_4 \rightarrow A_{11} \rightarrow A_1 \rightarrow A_{14} \rightarrow A_7 \rightarrow A_{12} \rightarrow A_8 \rightarrow A_2$. The positions of all these alternative arc welding robots in the lower, upper and border approximation areas are depicted in Figure 1. From this figure, it can be noticed that there are two arc welding robots, i.e. A_7 and A_{14} almost positioning on the border approximation area, and the locations of three robots, i.e. A_2, A_8 and A_{12} are in the lower approximation area. The remaining nine arc welding robots are positioned in the upper approximation area. Based on the positions of the alternative robots in the upper and lower approximation areas, they can be definitely categorized as efficient and inefficient ones respectively for the given welding task. Thus, it can be concluded that the arc welding robots, A_6, A_3, A_{13}, A_{10}, A_5, A_9, A_4, A_{11} and A_1 can be efficiently deployed to perform the required welding task in a real time manufacturing environment.

Table 2. Arc welding robot performance evaluation matrix by decision maker 1

Arc welding robot	PL	HR	VR	R	W	PR	C	FL	S	WP	M	EP
A_1	1	1	1	1	1	1	7	7	3	7	7	7
A_2	1	1	1	1	1	1	7	3	7	3	7	7
A_3	3	3	3	3	3	1	3	3	3	7	3	7
A_4	9	5	5	3	5	3	3	3	9	3	3	7
A_5	3	5	5	5	5	3	3	7	3	3	3	7
A_6	7	5	5	3	5	3	9	9	7	7	7	9
A_7	1	3	3	5	3	1	7	7	3	9	9	3
A_8	3	5	5	5	5	3	3	3	3	3	7	3
A_9	1	9	9	9	9	5	3	3	3	7	7	3
A_{10}	7	9	9	9	9	9	7	7	7	7	3	3
A_{11}	1	3	3	5	3	1	9	7	9	3	9	7
A_{12}	1	3	3	5	3	1	7	7	7	3	9	3
A_{13}	7	5	5	5	7	7	3	7	3	7	3	3
A_{14}	1	3	3	5	3	1	7	7	3	7	9	3

Table 3. Rough decision matrix for arc welding robot selection problem

Arc welding robot	PL	HR	VR	R	W	PR	C	FL	S	WP	M	EP
A_1	[1.32,2.28]	[1.08,1.72]	[1.08,1.72]	[1.32,2.28]	[1.32,2.28]	[1.08,1.72]	[7.08,7.72]	[7.08,7.72]	[3.08,3.72]	[7.08,7.72]	[5.72,6.68]	[5.72,6.68]
A_2	[1.72,2.68]	[1.08,1.72]	[1.32,2.28]	[1.32,2.28]	[1.08,1.72]	[1.08,1.72]	[7.08,7.72]	[3.32,4.28]	[5.72,6.68]	[3.08,3.72]	[6.28,6.92]	[6.28,6.92]
A_3	[3.08,3.72]	[3.08,3.72]	[3.32,4.28]	[3.32,4.28]	[3.08,3.72]	[1.32,2.28]	[3.32,4.28]	[3.32,4.28]	[3.32,4.28]	[5.72,6.68]	[1.72,2.68]	[5.72,6.68]
A_4	[8.28,8.92]	[5.32,6.28]	[5.08,5.72]	[3.08,3.72]	[4.28,4.92]	[3.32,4.28]	[3.72,4.68]	[3.08,3.72]	[8.28,8.92]	[3.32,4.28]	[1.72,2.68]	[5.32,6.28]
A_5	[3.08,3.72]	[5.32,6.28]	[5.32,6.28]	[5.08,5.72]	[5.32,6.28]	[3.32,4.28]	[3.08,3.72]	[5.72,6.68]	[1.72,2.68]	[3.32,4.28]	[3.08,3.72]	[5.32,6.28]
A_6	[6.28,6.92]	[5.72,6.68]	[5.08,5.72]	[3.08,3.72]	[5.08,5.72]	[3.08,3.72]	[7.72,8.68]	[8.28,8.92]	[5.72,6.68]	[6.28,6.92]	[7.32,8.28]	[7.72,8.68]
A_7	[1.32,2.28]	[3.08,3.72]	[3.32,4.28]	[5.08,5.72]	[3.32,4.28]	[1.08,1.72]	[7.08,7.72]	[6.28,6.92]	[3.08,3.72]	[8.28,8.92]	[8.28,8.92]	[3.08,3.72]
A_8	[3.32,4.28]	[5.08,5.72]	[5.32,6.28]	[5.08,5.72]	[3.72,4.68]	[3.32,4.28]	[3.32,4.28]	[3.08,3.72]	[3.08,3.72]	[3.32,4.28]	[6.28,6.92]	[3.32,4.28]
A_9	[1.08,1.72]	[8.28,8.92]	[8.28,8.92]	[7.72,8.68]	[8.28,8.92]	[3.72,4.68]	[3.72,4.68]	[3.08,3.72]	[3.32,4.28]	[5.72,6.68]	[5.72,6.68]	[3.72,4.68]
A_{10}	[6.28,6.92]	[7.72,8.68]	[7.72,8.68]	[8.28,8.92]	[8.28,8.92]	[7.72,8.68]	[6.28,6.92]	[7.08,7.72]	[5.72,6.68]	[5.72,6.68]	[3.08,3.72]	[3.32,4.28]
A_{11}	[1.08,1.72]	[3.32,4.28]	[3.32,4.28]	[5.08,5.72]	[3.32,4.28]	[1.32,2.28]	[8.28,8.92]	[7.32,8.28]	[7.72,8.68]	[3.32,4.28]	[8.28,8.92]	[5.72,6.68]
A_{12}	[1.32,2.28]	[3.32,4.28]	[3.08,3.72]	[5.08,5.72]	[3.32,4.28]	[1.32,2.28]	[7.08,7.72]	[7.08,7.72]	[7.32,8.28]	[3.72,4.68]	[7.72,8.68]	[3.72,4.68]
A_{13}	[5.72,6.68]	[5.32,6.28]	[5.32,6.28]	[5.32,6.28]	[7.08,7.72]	[7.08,7.72]	[3.08,3.72]	[7.32,8.28]	[3.08,3.72]	[5.72,6.68]	[3.08,3.72]	[3.08,3.72]
A_{14}	[1.08,1.72]	[3.08,3.72]	[3.32,4.28]	[5.32,6.28]	[3.32,4.28]	[1.32,2.28]	[7.32,8.28]	[7.08,7.72]	[3.08,3.72]	[6.28,6.92]	[7.08,7.72]	[3.32,4.28]

Table 4. Normalized rough decision matrix for arc welding robot selection problem

Arc welding robot	PL	HR	VR	R	W	PR	C	FL	S	WP	M	EP
A_1	[0.036,0.181]	[0,0.096]	[0,0.096]	[0.036,0.181]	[0.819,0.964]	[0.904,1.000]	[0,0.096]	[0.904,1.000]	[0.301,0.398]	[0.904,1.000]	[0.699,0.843]	[0.699,0.843]
A_2	[0.096,0.241]	[0,0.096]	[0.036,0.181]	[0.036,0.181]	[0.904,1.000]	[0.904,1.000]	[0,0.096]	[0.337,0.482]	[0.699,0.843]	[0.301,0.398]	[0.783,0.88]	[0.783,0.880]
A_3	[0.328,0.448]	[0.328,0.448]	[0.373,0.552]	[0.373,0.552]	[0.552,0.672]	[0.821,1.000]	[0.448,0.627]	[0.373,0.552]	[0.373,0.552]	[0.821,1.000]	[0.075,0.254]	[0.821,1.000]
A_4	[0.911,1.000]	[0.500,0.633]	[0.467,0.556]	[0.189,0.278]	[0.556,0.644]	[0.644,0.778]	[0.589,0.722]	[0.189,0.278]	[0.911,1.000]	[0.222,0.356]	[0,0.133]	[0.5000,0.633]
A_5	[0.274,0.403]	[0.726,0.919]	[0.726,0.919]	[0.677,0.806]	[0.081,0.274]	[0.484,0.677]	[0.597,0.726]	[0.806,1.000]	[0,0.194]	[0.323,0.516]	[0.274,0.403]	[0.726,0.919]
A_6	[0.548,0.658]	[0.452,0.616]	[0.342,0.452]	[0,0.110]	[0.548,0.658]	[0.890,1.000]	[0.041,0.205]	[0.890,1.000]	[0.452,0.616]	[0.548,0.658]	[0.726,0.89]	[0.795,0.959]
A_7	[0.031,0.153]	[0.255,0.337]	[0.286,0.408]	[0.510,0.592]	[0.592,0.714]	[0.918,1.000]	[0.153,0.235]	[0.663,0.745]	[0.255,0.337]	[0.918,1.000]	[0.918,1.000]	[0.255,0.337]
A_8	[0.063,0.313]	[0.521,0.688]	[0.583,0.833]	[0.521,0.688]	[0.583,0.833]	[0.688,0.938]	[0.688,0.938]	[0,0.167]	[0,0.167]	[0.063,0.313]	[0.833,1.000]	[0.063,0.313]
A_9	[0,0.082]	[0.918,1.000]	[0.918,1.000]	[0.847,0.969]	[0,0.082]	[0.541,0.663]	[0.541,0.663]	[0.255,0.337]	[0.286,0.408]	[0.592,0.714]	[0.592,0.714]	[0.337,0.459]
A_{10}	[0.548,0.658]	[0.795,0.959]	[0.795,0.959]	[0.890,1.000]	[0,0.110]	[0.041,0.205]	[0.342,0.452]	[0.685,0.795]	[0.452,0.616]	[0.452,0.616]	[0,0.110]	[0.041,0.205]
A_{11}	[0,0.082]	[0.286,0.408]	[0.286,0.408]	[0.510,0.592]	[0.592,0.714]	[0.847,0.969]	[0,0.082]	[0.796,0.918]	[0.847,0.969]	[0.286,0.408]	[0.918,1.000]	[0.592,0.714]
A_{12}	[0,0.130]	[0.272,0.402]	[0.239,0.326]	[0.511,0.598]	[0.598,0.728]	[0.870,1.000]	[0.130,0.217]	[0.783,0.87]	[0.815,0.946]	[0.326,0.457]	[0.870,1.000]	[0.326,0.457]
A_{13}	[0.508,0.692]	[0.431,0.615]	[0.431,0.615]	[0.431,0.615]	[0.108,0.231]	[0.108,0.231]	[0.877,1.000]	[0.815,1.000]	[0,0.123]	[0.508,0.692]	[0,0.123]	[0,0.123]
A_{14}	[0,0.089]	[0.278,0.367]	[0.311,0.444]	[0.589,0.722]	[0.556,0.689]	[0.833,0.967]	[0,0.133]	[0.833,0.922]	[0.278,0.367]	[0.722,0.811]	[0.833,0.922]	[0.311,0.444]

Table 5. Rough entropy weights for arc welding robot selection criteria

PL	HR	VR	R	W	PR	C	FL	S	WP	M	EP
[0.036,0.378]	[0.026,0.223]	[0.025,0.236]	[0.025,0.230]	[0.026,0.205]	[0.020,0.142]	[0.036,0.304]	[0.022,0.233]	[0.027,0.282]	[0.020,0.377]	[0.029,0.272]	[0.025,0.271]

Table 6. Weighted normalized rough decision matrix for arc welding robot selection problem

Arc welding robot	PL	HR	VR	R	W	PR	C	FL	S	WP	M	EP
A_1	[0.038,0.447]	[0.026,0.245]	[0.025,0.258]	[0.026,0.271]	[0.047,0.402]	[0.039,0.285]	[0.036,0.333]	[0.042,0.466]	[0.035,0.395]	[0.038,0.755]	[0.049,0.502]	[0.042,0.500]
A_2	[0.040,0.469]	[0.026,0.245]	[0.026,0.278]	[0.026,0.271]	[0.050,0.410]	[0.039,0.285]	[0.036,0.333]	[0.030,0.345]	[0.046,0.520]	[0.026,0.527]	[0.051,0.512]	[0.044,0.510]
A_3	[0.048,0.548]	[0.035,0.323]	[0.034,0.366]	[0.035,0.356]	[0.041,0.342]	[0.037,0.285]	[0.052,0.494]	[0.030,0.361]	[0.037,0.438]	[0.037,0.755]	[0.031,0.341]	[0.045,0.542]
A_4	[0.069,0.757]	[0.039,0.365]	[0.037,0.366]	[0.030,0.293]	[0.041,0.337]	[0.033,0.253]	[0.057,0.523]	[0.026,0.298]	[0.051,0.565]	[0.025,0.511]	[0.029,0.309]	[0.037,0.443]
A_5	[0.046,0.531]	[0.045,0.429]	[0.043,0.452]	[0.042,0.415]	[0.028,0.261]	[0.030,0.239]	[0.057,0.524]	[0.040,0.466]	[0.027,0.337]	[0.027,0.572]	[0.037,0.382]	[0.043,0.521]
A_6	[0.056,0.627]	[0.038,0.361]	[0.033,0.342]	[0.025,0.255]	[0.040,0.339]	[0.038,0.285]	[0.037,0.366]	[0.042,0.466]	[0.039,0.456]	[0.031,0.625]	[0.049,0.515]	[0.044,0.531]
A_7	[0.037,0.436]	[0.033,0.299]	[0.032,0.332]	[0.038,0.365]	[0.042,0.351]	[0.039,0.285]	[0.041,0.375]	[0.037,0.406]	[0.034,0.377]	[0.039,0.755]	[0.055,0.545]	[0.031,0.363]
A_8	[0.039,0.497]	[0.040,0.377]	[0.039,0.432]	[0.038,0.387]	[0.041,0.375]	[0.034,0.276]	[0.060,0.588]	[0.022,0.272]	[0.027,0.329]	[0.021,0.495]	[0.053,0.545]	[0.026,0.356]
A_9	[0.036,0.409]	[0.050,0.447]	[0.048,0.471]	[0.047,0.452]	[0.026,0.221]	[0.031,0.237]	[0.055,0.505]	[0.028,0.311]	[0.035,0.398]	[0.032,0.647]	[0.046,0.467]	[0.033,0.396]
A_{10}	[0.056,0.627]	[0.047,0.438]	[0.045,0.461]	[0.048,0.459]	[0.026,0.227]	[0.021,0.172]	[0.048,0.441]	[0.037,0.418]	[0.039,0.456]	[0.029,0.61]	[0.029,0.302]	[0.026,0.327]
A_{11}	[0.036,0.409]	[0.034,0.315]	[0.032,0.332]	[0.038,0.365]	[0.042,0.351]	[0.037,0.280]	[0.036,0.329]	[0.040,0.447]	[0.050,0.556]	[0.026,0.531]	[0.055,0.545]	[0.039,0.465]
A_{12}	[0.036,0.428]	[0.033,0.313]	[0.031,0.312]	[0.038,0.367]	[0.042,0.354]	[0.038,0.285]	[0.040,0.370]	[0.039,0.435]	[0.049,0.549]	[0.027,0.550]	[0.054,0.545]	[0.033,0.395]
A_{13}	[0.055,0.640]	[0.037,0.361]	[0.036,0.380]	[0.036,0.371]	[0.029,0.252]	[0.022,0.175]	[0.067,0.607]	[0.040,0.466]	[0.027,0.317]	[0.030,0.638]	[0.029,0.306]	[0.025,0.305]
A_{14}	[0.036,0.412]	[0.033,0.305]	[0.033,0.340]	[0.040,0.395]	[0.041,0.346]	[0.037,0.280]	[0.036,0.344]	[0.041,0.448]	[0.034,0.386]	[0.035,0.683]	[0.053,0.523]	[0.032,0.392]

Table 7. BAA matrix for arc welding robot selection problem

PL	HR	VR	R	W	PR	C	FL	S	WP	M	EP
[0.0439, 0.5070]	[0.0363, 0.3388]	[0.0346, 0.3603]	[0.0356, 0.3532]	[0.0374, 0.3205]	[0.0335, 0.2552]	[0.0458, 0.4278]	[0.0346, 0.3942]	[0.0369, 0.4265]	[0.0297, 0.6119]	[0.0427, 0.4412]	[0.0349, 0.4246]

Table 8. Distance matrix for arc welding robot selection problem

Arc welding robot	PL	HR	VR	R	W	PR	C	FL	S	WP	M	EP
A_1	-0.6186	-0.3759	-0.4031	-0.4030	-0.0822	-0.0300	0.0953	0.5566	-0.5303	0.9243	0.6042	0.6022
A_2	-0.6321	-0.3759	-0.4137	-0.4030	-0.0899	-0.0300	0.0953	-0.4789	0.6156	-0.7685	0.6101	0.6085
A_3	0.6815	-0.4183	0.4646	0.4521	-0.0220	-0.0297	-0.0666	-0.4891	0.5594	0.9253	-0.5076	0.6338
A_4	0.8365	0.4447	0.4635	-0.4134	-0.0165	0.0021	-0.0959	-0.4522	0.6475	-0.7595	-0.4908	0.5628
A_5	0.6705	0.4903	0.5243	0.4903	0.0603	0.0167	-0.0970	0.5580	-0.4998	-0.7978	-0.5282	0.6178
A_6	0.7372	0.4428	-0.4487	-0.3944	-0.0191	-0.0299	0.0622	0.5568	0.5711	0.8318	0.6135	0.6253
A_7	-0.6120	-0.4031	-0.4427	0.4562	-0.0308	-0.0300	0.0530	0.5157	-0.5198	0.9241	0.6333	-0.5121
A_8	-0.6515	0.4534	0.5106	0.4721	-0.0550	-0.0207	-0.1613	-0.4411	-0.4953	-0.7518	0.6348	-0.5116
A_9	-0.5959	0.5019	0.5368	0.5172	0.0997	0.0185	-0.0780	-0.4591	-0.5327	0.8467	0.5800	-0.5325
A_{10}	0.7372	0.4963	0.5308	0.5223	0.0940	0.0845	-0.0134	0.5237	0.5711	-0.8222	-0.4874	-0.4944
A_{11}	-0.5959	-0.4131	-0.4427	0.4562	-0.0308	-0.0255	0.0998	0.5436	0.6415	-0.7713	0.6333	0.5774
A_{12}	-0.6074	-0.4124	-0.4309	0.4572	-0.0337	-0.0299	0.0583	0.5352	0.6366	-0.7827	0.6342	-0.5322
A_{13}	0.7485	0.4430	0.4743	0.4615	0.0690	0.0807	-0.1809	0.5579	-0.4881	0.8418	-0.4893	-0.4823
A_{14}	-0.5976	-0.407	-0.4480	0.4770	-0.0255	-0.0251	0.0841	0.5437	-0.5250	0.8719	0.6182	-0.5303

Table 9. Final scores for the arc welding robots

Arc welding robot	A_1	A_2	A_3	A_4	A_5	A_6	A_7	A_8	A_9	A_{10}	A_{11}	A_{12}	A_{13}	A_{14}
Score	0.3394	-1.2624	2.1833	0.7288	1.5054	3.5485	0.0316	-1.0175	0.9026	1.7425	0.6725	-0.5076	2.0361	0.0365
Rank	9	14	2	7	5	1	11	13	6	4	8	12	3	10

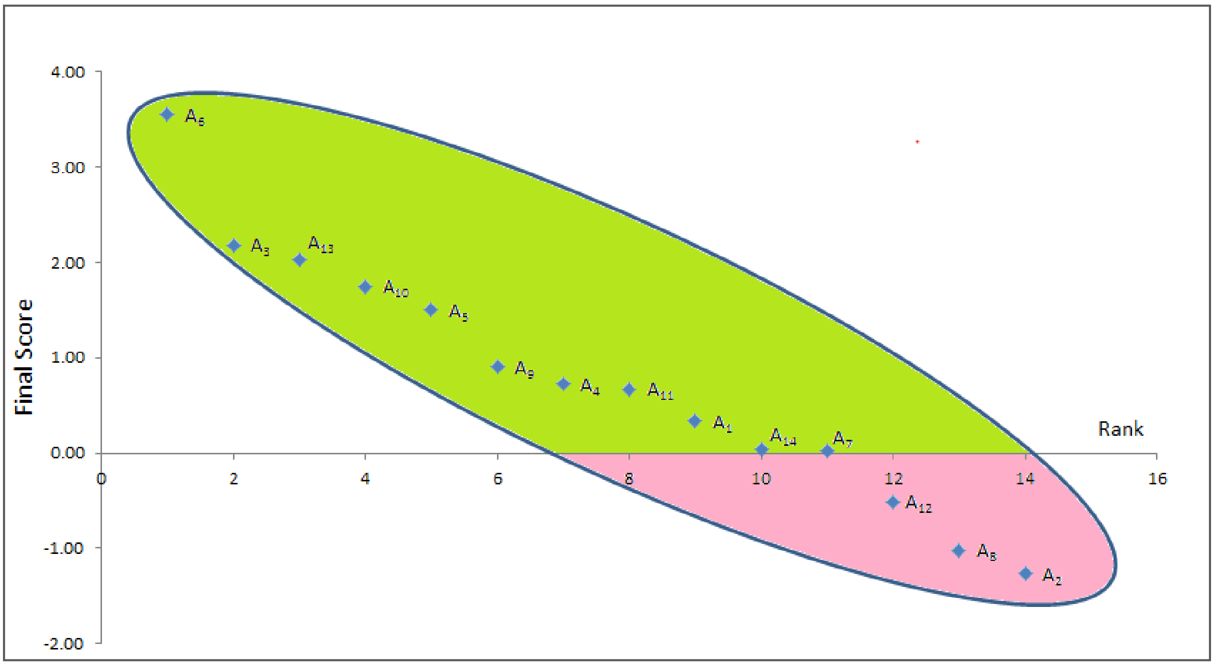

Figure 1. Positions of the arc welding robots in the lower, upper and border approximation areas

Now, in order to analyze the capabilities of each of the considered arc welding robots as well as their strengths and weaknesses, Tables 10 and 11 are developed. In Table 9, the locations of all the arc welding robots in the upper and lower approximation areas with respect to various evaluation criteria are portrayed. In this industrial robot selection problem, it has already been stated that PL, HR, VR, R, FL, S, WP, M and EP are the beneficial criteria, whereas, W, PR and C are the non-beneficial criteria. From Table 10, it can be observed that for the beneficial attributes, the locations of almost all the efficient arc welding robots are in the upper approximation area. In the similar way, those efficient arc welding robots are positioned in the lower approximation area for the non-beneficial criteria. In Table 11, the locations of 12 robot selection criteria in the upper and lower approximation areas for the 14 arc welding robots are shown. For the efficient robots, almost all the beneficial criteria are located in the upper approximation area and the positions of the non-beneficial attributes are in the lower approximation area. It can be propounded that robot A_6 (the top ranked alternative) is quite strong with respect to PL, HR, C, FL, S, WP, M and EP criteria, whereas, it has weaknesses only in VR, R, W and PR criteria. Thus, it has relatively low vertical reach, low repeatability, high weight and high power rating. On the other hand, the major strengths of A_3 (second ranked robot) are with respect to PL, VR, R, S, WP and EP, and it is weak with respect to HP, W, PR, C, FL and M criteria. It has poor horizontal reach, flexibility and maintainability. Similarly, the last ranked arc welding robot A_2 has only four criteria (C, S, M and EP) in its favour. It has major weaknesses with respect to PL, HR, VR, R, W, PR, FL and WP criteria. The identification of the strengths and weaknesses of each of the alternative arc welding robots would thus guide the decision makers in choosing the most appropriate robot for a given welding task.

In order to study the solution accuracy of rough-MABAC method in solving this arc welding robot selection problem, its ranking performance is finally compared with that of other rough-MCDM methods, i.e. rough-WASPAS, rough-SAW, rough-TOPSIS and rough-VIKOR, as shown in Table 12. It can be observed from this table that the positions of the top two and last arc welding robots remain unchanged in most of the rough-MCDM methods, although there are variations in the intermediate rankings of the considered alternatives. It proves the applicability of rough-MABAC method as an effective and sound mathematical tool for solving diverse problems in group decision making environment where the individual judgements of the decision makers are subjectively expressed.

Table 10. Positions of arc welding robots with respect to different evaluation criteria

Evaluation criteria	Position of the arc welding robot	
	Upper approximation area	Lower approximation area
PL	A_3, A_4, A_5, A_6, A_{10}, A_{13}	A_1, A_2, A_7, A_8, A_9, A_{11}, A_{12}, A_{14}
HR	A_4, A_5, A_6, A_8, A_9, A_{10}, A_{13}	A_1, A_2, A_3, A_7, A_{11}, A_{12}, A_{14}
VR	A_3, A_4, A_5, A_8, A_9, A_{10}, A_{13}	A_1, A_2, A_6, A_7, A_{11}, A_{12}, A_{14}
R	A_3, A_5, A_7, A_8, A_9, A_{10}, A_{11}, A_{12}, A_{13}, A_{14}	A_1, A_2, A_4, A_6
W	A_5, A_9, A_{10}, A_{13}	A_1, A_2, A_3, A_4, A_6, A_7, A_8, A_{11}, A_{12}, A_{14}
PR	A_4, A_5, A_9, A_{10}, A_{13}	A_1, A_2, A_3, A_6, A_7, A_8, A_{11}, A_{12}, A_{13}
C	A_1, A_2, A_6, A_7, A_{11}, A_{12}, A_{14}	A_3, A_4, A_5, A_8, A_9, A_{10}, A_{13}
FL	A_1, A_5, A_6, A_7, A_{10}, A_{11}, A_{12}, A_{13}, A_{14}	A_2, A_3, A_4, A_8, A_9
S	A_2, A_3, A_4, A_6, A_{10}, A_{11}, A_{12}	A_1, A_5, A_7, A_8, A_9, A_{13}, A_{14}
WP	A_1, A_3, A_6, A_7, A_9, A_{13}, A_{14}	A_2, A_4, A_5, A_8, A_{10}, A_{11}, A_{12}
M	A_1, A_2, A_6, A_7, A_8, A_9, A_{11}, A_{12}, A_{14}	A_3, A_4, A_5, A_{10}, A_{13}
EP	A_1, A_2, A_3, A_4, A_5, A_6, A_{11}	A_7, A_8, A_9, A_{10}, A_{12}, A_{13}, A_{14}

Table 11. Positions of different evaluation criteria for arc welding robots

Arc welding robot	Position of the evaluation criteria	
	Upper approximation area	Lower approximation area
A_1	C, FL, WP, M, EP	PL, HR, VR, R, W, PR, S
A_2	C, S, M, EP	PL, HR, VR, R, W, PR, FL, WP
A_3	PL, VR, R, S, WP, EP	HR, W, PR, C, FL, M
A_4	PL, HR, VR, PR, S, EP	R, W, C, FL, WP, M
A_5	PL, HR, VR, R, W, PR, FL, EP	C, S, WP, M
A_6	PL, HR, C, FL, S, WP, M, EP	VR, R, W, PR
A_7	R, C, FL, WP, M	PL, HR, VR, W, PR, S, EP
A_8	HR, VR, R, M	PL, W, PR, C, FL, S, WP, EP
A_9	HR, VR, R, W, PR, WP, M	PL, C, FL, S, EP
A_{10}	PL, HR, VR, R, W, PR, FL, S	C, WP, M, EP
A_{11}	R, C, FL, S, M, EP	PL, HR, VR, W, PR, WP
A_{12}	R, C, FL, S, M	PL, HR, VR, W, PR, WP, EP
A_{13}	PL, HR, VR, R, W, PR, FL, WP	C, S, M, EP
A_{14}	R, C, FL, WP, M	PL, HR, VR, W, PR, S, EP

Table 12. Comparison of rankings based on different rough-MCDM methods

Arc welding robot	Rough MCDM method				
	Rough-MABAC	Rough-WASPAS	Rough-SAW	Rough-TOPSIS	Rough-VIKOR
A_1	9	12	11	13	4
A_2	14	14	14	9	14
A_3	2	1	1	6	1
A_4	7	4	4	1	2
A_5	5	3	3	7	6
A_6	1	2	2	2	5
A_7	11	5	10	12	3
A_8	13	9	7	14	8
A_9	6	6	5	10	10
A_{10}	4	8	6	3	13
A_{11}	8	7	8	4	11
A_{12}	12	10	9	5	12
A_{13}	3	13	12	11	9
A_{14}	10	11	13	8	7

5. Discussions

As selection of the most apposite robot for a specific welding operation is a capital intensive task, this decision making process must be formulated seeking opinions of a group of experts to avoid biasness/partiality in the final selection decision. A wrongly selected robot may negatively influence productivity of a manufacturing organization. In this paper, an attempt is put forward to rank 14 arc welding robot alternatives based on 12 evaluation criteria using an integrated approach combining rough numbers and MABAC method. The performances of all the robots are first assessed with respect to the considered criteria using the judgements of five decision makers/experts. As criteria weights play a pivotal role in any decision making process, rough entropy method having the advantage of determining importance of the criteria based on randomness of the dataset itself is employed here. The MABAC is later adopted to provide a complete ranking of the candidate arc welding robots from the best to the worst along with the strengths and weaknesses of each of the alternatives. It is observed that among the considered alternatives, A_6 is the best performing robot, followed by A_3. On the other hand, robot A_2 is the worst preferred choice. Arc welding robot A_6 has the strengths with respect to PL, HR, C, FL, S, WP, M and EP evaluation criteria, whereas, VR, R, W and PR are its major weaknesses. It has low vertical reach and repeatability, and high weight and power rating. Similarly, for robot A_2, C, S, M and EP are its favourable properties and it lags behind with respect to PL, HR, VR, R, W, PR, FL and WP criteria. In the similar direction, application of rough-MABAC method segregates all the candidate robots as the best performing and underperforming ones with respect to each of the evaluation criteria. For example, robots A_3, A_4, A_5, A_6, A_{10} and A_{13} are the best performing alternatives (positioned in upper approximation area) with respect to PL criterion. On the contrary, robots A_1, A_2, A_7, A_8, A_9, A_{11}, A_{12} and A_{14} are underperforming (located in lower approximation area) against criterion PL. Identification of the deficiencies of the inefficient arc welding robots (underperformers) would help the concerned manufacturers to modify the existing specifications and/or add new technical features to make them more comparable and appropriate for a specific welding task. In this context, the advantageous features of the best performing robots can act as an appraisement module (benchmark) to others with respect to product variety, reliability and safe functionality.

Application of this integrated MCDM methodology thus proves itself as an efficient decision making tool while accurately providing complete ranking order of the considered arc welding robots. It can thus assist the decision makers/managers in understanding and improving the selection process of the most suitable arc welding robot from available alternatives along with process enhancement and adaptation of business intelligence leading to conceptualization of Industry 4.0 approach.

6. Conclusions

It has already been pointed out by the previous researchers that integration of rough set theory with any of the MCDM methods would provide more accurate and reliable ranking solutions to varied decision making problems. Keeping this objective in mind, the present paper dealt with the application of rough-MABAC method for evaluation and selection of the most appropriate arc welding robot based on a set of 12 conflicting criteria. In order to avoid subjectivity in human judgements, the weights of the considered evaluation criteria are estimated using rough entropy method. Based on this analysis, all the 14 arc welding robots are classified as efficient and inefficient ones based on their positions in the upper and lower approximation areas respectively. The robot A_6 is identified as the best option for performing the given welding task with eight favourable (PL, HR, C, FL, S, WP, M and EP) and only four unfavourable criteria (VR, R, W and PR). On the other hand, A_2 is the least preferred robot with only four favourable (C, S, M and EP) and eight unfavourable criteria (PL, HR, VR, R, W, PR, FL and WP). A comparison study of the ranking performance with the other rough-MCDM methods proves the efficacy of rough-MABAC approach in solving complex decision making problems. However, rough-MABAC method suffers from some drawbacks. It is unable to provide satisfactory results when the criteria weights are completely unknown. It is assumed that all the evaluation criteria are independent to each other which may not be true in real time welding environment. During information aggregation using rough numbers, it is also supposed that all the participating decision makers have equal importance. But, based on its several attractive advantages, it can be effectively applied as a flexible and comprehensive tool for solving real time decision making problems, such as selection of appropriate machine tool, flexible manufacturing system, cutting fluid, materials for engineering components etc. As a further future scope, the applicability of MABAC method using interval rough number or intuitionistic fuzzy sets may be explored.

References

[1] Khouja, M. The use of data envelopment analysis for technology selection, Computers and Industrial Engineering, 1995, 28(1): pp. 132-132.

[2] Khouja, M., Booth, D.E. Fuzzy clustering procedure for evaluation and selection of industrial robots, Journal of Manufacturing Systems, 1995, 14(4): 244-251.

[3] Goh, C-H., Tung, T-C.A., Cheng, C-H. A revised weighted sum decision model for robot selection, Computers and Industrial Engineering, 1996, 30(2): 193-199.

[4] Bhangale, P.P., Agrawal, V.P., Saha, S.K. Attribute based specification, comparison and selection of a robot, Mechanism and Machine Theory, 2004, 39(12): 1345-1366.

[5] Sen, D.K., Datta, S., Patel, S.K., Mahapatra, S.S. Multi-criteria decision making towards selection of industrial robot: Exploration of PROMETHEE II method, Benchmarking: An International Journal, 2015, 22(3), 465-487.

[6] Ghorabaee, M.K. Developing an MCDM method for robot selection with interval type-2 fuzzy sets, Robotics and Computer-Integrated Manufacturing, 2016, 37, 221-232.

[7] Gitinavard, H., Mousavi, S.M., Vahdani, B., Siadat, A. A distance-based decision model in interval-valued hesitant fuzzy setting for industrial selection problems, Scientia Iranica, Transaction E, Industrial Engineering, 2016, 23(4), 1928-1940.

[8] Karande, P., Zavadskas, E.K., Chakraborty, S. A study on the ranking performance of some MCDM methods for industrial robot selection problems, International Journal of Industrial Engineering Computations, 2016, 7(3), 399-422.

[9] Sen, D.K., Datta, S., Mahapatra, S.S. Extension of PROMETHEE for robot selection decision making: Simultaneous exploration of objective data and subjective (fuzzy) data, Benchmarking: An International Journal, 2016, 23(4), 983-1014.

[10] Sen, D.K., Datta, S., Mahapatra, S.S. Application of TODIM (Tomada de Decisión Inerativa Multicritero) for industrial robot selection, Benchmarking: An International Journal, 2016, 23(7), 1818-1833.

[11] Xue, Y.X., You, J.X., Zhao, X., Liu, H.C. An integrated linguistic MCDM approach for robot evaluation and selection with incomplete weight information, International Journal of Production Research, 2016, 54(18), 5452-5467.

[12] Breaz, R.E., Bologa, O., Racz, S.G. Selecting industrial robots for milling applications using AHP, Procedia Computer Science, 2017, 122, 346-353.

[13] Wang, J.J., Miao, Z.H., Cui, F.B., Liu, H.C. Robot evaluation and selection with entropy-based combination weighting and cloud TODIM approach, Entropy, 2018, 20(5), 19 pages, https://doi.org/10.3390/e20050349.

[14] Liu, H.C., Quan, M.Y., Shi, H., Guo, C. An integrated MCDM method for robot selection under interval-valued Pythagorean uncertain linguistic environment, International Journal of Intelligent Systems, 2019, 34(2), 188-214.

[15] Yalçin, N., Uncu, N. Applying EDAS as applicable MCDM method for industrial robot selection. Sigma Journal of Engineering and Natural Sciences, 2019, 37(3), 779-796.

[16] Nasrollahi, M., Ramezani, J., Sadraei, M. A FBWM-PROMETHEE approach for industrial robot selection. Heliyon, 2020, 6, e03859.

[17] Suszynski, M., Rogalewicz, M., Selection of an industrial robot for assembly jobs using multi-criteria decision making methods. Management and Production Engineering Review, 2020, 11(1), 62-72.

[18] Zhang, N., Zhang, F., Huang, Y., Zhang, H., Zhao, Y., LI, R. Labelling robots selection based on AHP and TOPSIS. UPB Scientific Bulletin, Series D: Mechanical Engineering, 2020, 82(3), 29-40.

[19] Rashid, T., Ali, A., Chu, Y-M. Hybrid BW-EDAS MCDM methodology for optimal industrial robot selection. PLoS ONE, 2021, 16(2), e0246738.

[20] Durmić, E., Stević, Ž., Chatterjee, P., Vasiljević, M., Tomašević, M. Sustainable supplier selection using combined FUCOM-rough SAW model. Reports in Mechanical Engineering, 2020, 1(1), 34-43.

[21] Sharma, H. K., Kumari, K., Kar, S. A rough set theory application in forecasting models. Decision Making: Applications in Management and Engineering, 2020, 3(1), 1-21.

[22] Pamučar, D., Janković, A. The application of the hybrid interval rough weighted power Heronian operator in multi-criteria decision-making. Operational Research in Engineering Sciences: Theory and Applications, 2020, 3(2), 54-73.

[23] Sinani, F., Erceg, Z., Vasiljevic, M. An evaluation of a third-party logistics provider: The application of the rough Dombi-Hamy mean operator. Decision-Making: Applications in Management and Engineering, 2020, 3(1), 92-107.

[24] Božanić, D., Ranđelović, A., Radovanović, M., Tešić, D. A hybrid LBWA-IR-MAIRCA multi-criteria decision-making model for determination of constructive elements of weapons. Facta Universitatis Series: Mechanical Engineering, 2020, 18(3), 399-418.

[25] Roy, J., Chatterjee, K., Bandyopadhyay, A., Kar, S. Evaluation and selection of medical tourism sites: A rough analytic hierarchy process based multi-attributive border approximation area comparison approach, Expert Systems, 2018, 35, 18 pages, DOI:10.1111/exsy.12232.

[26] Stojić, G., Stević, Ž., Antuchevičienė, J., Pamučar, D., Vasiljević, M. A novel rough WASPAS approach for supplier selection in a company manufacturing PVC carpentry products, Information, 2018, 9, 16 pages, DOI:10.3390/info90501212018.

[27] Zhai, L., Khoo, L., Zhong, Z. A rough set enhanced fuzzy approach to quality function deployment, International Journal of Advanced Manufacturing Technology, 2008, 37(5), 613-624.

[28] Hu, J., Zhu, G., Qi, J., Peng, Y., Peng, X. Design concept evaluation based on rough number and information entropy theory, In: Proceedings of the 12th International Conference on Ubiquitous Intelligence and Computing, 2015, 1425-1431.

[29] Biswas, T.K., Das, M.C. Selection of hybrid vehicle for green environment using multi-attributive border approximation area comparison method, Management Science Letters, 2018, 8(2), 121-130.

[30] Chatterjee, P., Mondal, S., Boral, S., Banerjee, A., Chakraborty, S. A novel hybrid method for non-traditional machining selection using factor relationship and multi-attributive border approximation method, Facta Universitatis Series: Mechanical Engineering, 2017, 15(3), 439-456.

[31] Debnath, A., Roy, J., Kar, S., Zavadskas, E.K., Antuchevičiene, J. A hybrid MCDM approach for strategic project portfolio selection of agro by-products, Sustainability, 2017, 9, 33 pages, DOI:10.3390/su9081302.

[32] Pamučar, D., Ćirovic, G. The selection of transport and handling resources in logistics centers using multi-attributive border approximation area comparison (MABAC), Expert Systems with Applications, 2015, 42, 3016-3028.

[33] Pamučar, D., Stević, Ž., Zavadskas, E.K. University integration of interval rough AHP and interval rough MABAC methods for evaluating university web pages, Applied Soft Computing, 2018, 67, 141-163.

[34] Chakraborty, S., Dandge, S.S., Agarwal, S. Non-traditional machining processes selection and evaluation: A rough multi-attributive border approximation area comparison approach, Computers & Industrial Engineering, 2020, 139, 106201.

JJMIE

Volume 15, Number 2, June. 2021
ISSN 1995-6665
Pages 181 - 189

Jordan Journal of Mechanical and Industrial Engineering

Lead-Free Solder Reliability Modeling Using Adaptive Neuro-Fuzzy Inference System (ANFIS)

Azmi Alazzam[a], Tariq Tashtoush[b*]

[a] Computer Information Science- Higher Colleges of Technology - Al-Ain Women's Campus, Al-Ain, Abu Dhabi, UAE.

[b] School of Engineering Texas A&M International University - Laredo, Texas, USA

Received July 8 2020 Accepted April 14 2021

Abstract

Lead-free solder is a new material that has been utilized in manufacturing electronic components and packages; therefore, the material behavior had not been analyzed completely. This paper summarizes our effort to model the change in lead-free solder hardness behavior with respect to aging time and temperature as a measure of the components' reliability. ANFIS is a modeling technique that had been used in analyzing the current trend and predicting future progression. The ANFIS model was developed based on the BPN-ANN structure with two inputs and one output using Matlab®. The developed model was compared to different regression models that are being used frequently in the literature. The well-trained ANFIS model gave very accurate results for predicting the hardness (output) with a small Root Mean Square Error (RMSE) compared to the Minitab® regression models. ANFIS is one of the best techniques in modeling non-linear data, and it can give better and more accurate data representation and future prediction.

Keywords: Fuzzy Logic, Neural Network, Behavior Modeling, Lead-Free Solder, Aging, Reliability, Electronic packages, Matlab, Minitab;

1. Introduction

Fuzzy Logic and Artificial Neural Networks (ANN) are very common techniques used for soft computing. While Fuzzy Logic depends mainly on the knowledge from the expert, the neural network is based on the system data that has been collected. Nowadays, there are new techniques that combine neural machine learning with fuzzy systems; these are called "Neuro-Fuzzy" approaches, developed first at Matsushita laboratories for consumer appliances where the ANN learning technique was used to design the fuzzy model itself. In other words, the neural and the fuzzy components are not two separate design components anymore, but rather two different aspects of the same component.

ANFIS stands for Adaptive Network-based Fuzzy Inference System, whichis one example of a neuro-fuzzy approach that uses a hybrid-learning algorithm to identify parameters of Sugeno-type fuzzy inference systems. It applies a combination of the least-squares method and the back propagation gradient descent method for training FIS membership function parameters to emulate a given training data set [1].

In this paper, the reliability of lead-free solder will be modeled using ANFIS. The proposed model will be designed and implemented using Matlab as a software platform. The paper is organized as follows: section 2 is the literature review which includes the Adaptive Neuro-Fuzzy Interface System and a description of the system of interest, section 3 deals with data used for modeling purposes, section 4 provides alternative modeling approaches for comparison, section 5 shows the modeling results, and section 6 concludes the paper and describes the authors' future plan.

2. Literature Review

2.1. Adaptive Neuro-Fuzzy Inference System (ANFIS)

In the last decade, Artificial intelligence (AI) techniques became an important approach, which plays a significant role in multiple fields. AI techniques consist of several intelligent methods, such as genetic fuzzy systems, neuro-fuzzy systems, genetic programming, and neural networks, etc. A Neuro-fuzzy system (ANFIS) is an approach that consists of an Artificial Neural Network (ANN) and a Fuzzy Logic Inference System (FIS). The neuro-fuzzy system implements the principle of fuzzy logic-based learning capabilities and neural network techniques, which is a hybrid technique used in soft computing, that utilizes a hybrid-learning algorithm to identify parameters of Sugeno-Type Fuzzy Inference Systems [2].

Fuzzy rules are developed based on a sample dataset training, while ANFIS applies a combination of the least-squares and the back propagation gradient descent methods for training FIS membership function parameters to emulate a given training data set. Neuro-fuzzy systems (ANIFS) are widely used in healthcare applications such as predicting and modeling cardiac disease, brain disorder, and breast cancer [3]. In addition, the neuro-fuzzy system had been used intensively in the production environment, quality control, emergency responses and traffic management, and

* Corresponding author e-mail: Tariq.Tashtoush@tamiu.edu.

material analysis [4-15]. The FIS, ANN, and the ANFIS structure will be explained in the following subsections [2].

2.1.1. Fuzzy Inference System (FIS)

Fuzzy logic was first introduced by Lotfi Zadeh's proposal of fuzzy set theory in 1965. Since then, fuzzy logic and several applications for fuzzy set theory were developed. Fuzzy logic is a form that has more than two values; it was derived from fuzzy set theory to deal with approximate logic rather than real facts. In contrast with "crisp logic" where binary sets have binary logic, fuzzy logic variables may have a logical value that ranges between "0 and 1" and is not limited to two values (0, 1) like in the binary logic. Furthermore, when linguistic variables are used, these degrees may be managed by specific functions, usually called membership functions [16].

Since Fuzzy logic was a proposal of the fuzzy set theory, it is important to explain what fuzzy set is and how it is different from the classical set. A fuzzy set is a set with a fuzzy boundary, which means that there is a gradual transition in defining whether the element belongs to one set or another; this transition is different due to the difference of the membership function. The membership functions are functions that map each system element of the domain (the input) to a membership value between zero and one. This will allow the fuzzy sets to be flexible in expressing the fuzzy relation in linguistic terms. Figure1illustrates the concept of fuzzy sets and fuzzy relations. In this relation, the membership functions are defined for the linguistic variable X (age) as three membership functions for a different level of age, and those levels are subjective. Choosing these membership functions could be different from one person to another, but this choice will depend on the heuristic knowledge and the common sense, which is usually not random [16-17]. There are differences between binary and fuzzy logic; in binary logic, values can be either zero or one for the values. However, in fuzzy logic, you can find any value between zero and one, so there are more variations and more flexibility for modeling and design.

In Figure 1, the fuzzy relation consists of five membership functions. The X-axis represents the life span of the human being (0-100 years). The Y-axis represents the membership grade (0-1). The membership grade is different from probability, which also takes the same values (0-1), and this is what makes the fuzzy logic different from the probability theory [18]. At the value of x=20 years, the membership grade from the y-axis is $0.5(\text{young}) + 0.2(\text{very young}) + 0.5(\text{Middle} - \text{Aged})$.

Fuzzy inference is the concept of using fuzzy logic to map the output of each fuzzy input. The mapping then provides a reference to make decisions about what the output will be. The process of fuzzy inference requires the use of Membership Functions, Logical Operations (mostly or/and), and If-Then rules [16].

There are different types of fuzzy inference systems; this research will utilize the "Takagi-type", the "Sugeno-type", the "Takagi-Sugeno-type", and the "TSK-type" (for Takagi-Sugeno-Kang) FIS. It can also be called a "1st order Sugeno Model". In this type of FIS, three terms (S, M, and L as abbreviations for small, medium, and large) for the various variables will be used. In a TSK-style FIS, the rules would look like the following:

Rule #1: IF x is S1 AND x2 is S2 THEN f = c10 + c11x + c12x2.

Rule #2: IF x is S1 AND x2 is M2 THEN f = c20 + c21x + c22x2.

Rule #3: IF x is S1 AND x2 is L2 THEN f = c30 + c31x + c32x2.

Rule #4: IF x is M1 AND x2 is S2 THEN f = c40 + c41x + c42x2.

Rule #5: IF x is M1 AND x2 is M2 THEN f = c50 + c51x + c52x2.

Rule #6: IF x is M1 AND x2 is L2 THEN f = c60 + c61x + c62x2.

Rule #7: IF x is L1 AND x2 is S2 THEN f = c70 + c71x + c72x2.

Rule #8: IF x is L1 AND x2 is M2 THEN f = c80 + c81x + c82x2.

Rule #9: IF x is L1 AND x2 is L2 THEN f = c90 + c91x + c92x2.

Fuzzy inference systems have been successfully applied in different fields of industry, such as automatic control, data classification, decision analysis, expert systems, and computer vision. Fuzzy inference systems have different names, such as fuzzy-rule-based systems, fuzzy expert systems, fuzzy modeling, fuzzy associative memory, fuzzy logic controllers, and simple (and ambiguously) fuzzy systems [16].

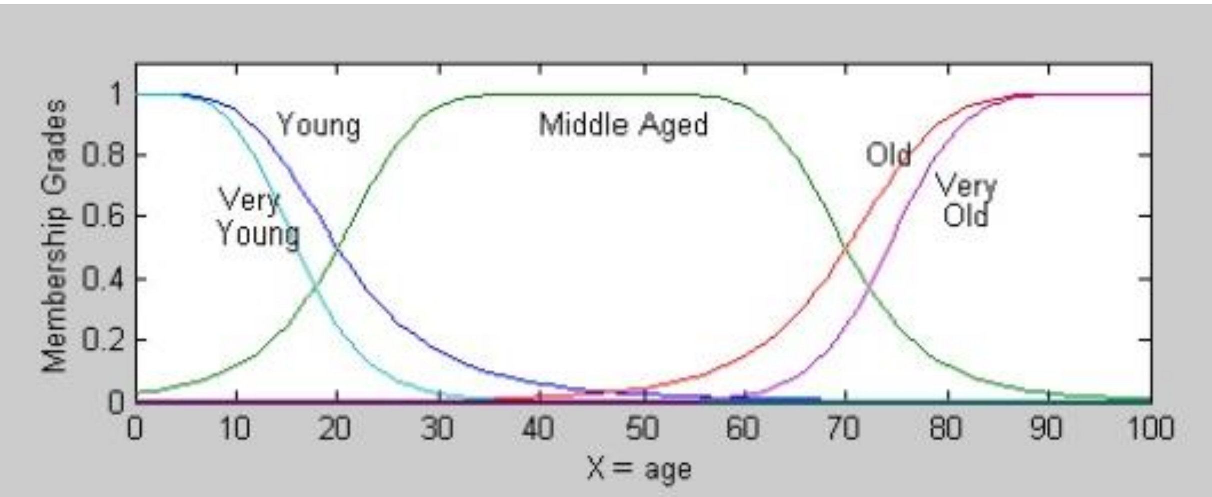

Figure 1. Fuzzy relation for age variable

2.1.2. Artificial Neural Network

The human mind/brain is an amazing complicated network of neurons that can process incomplete and imprecise sensor information very effectively through different neurons. The Artificial Neural Network mimics at a simple level the way that the biological neurons learn or get trained to learn, and this is how it was given a similar name. These models are also known as connectionist models that try to use the principle of learning in the human brain. The ANN consists of several independent processors (neurons) that communicate with each other. The neurons communicate with each other via weighted connections. Current research has been in the development of architectures of the ANN, learning algorithms, and application of these models to information processing tasks [18].

There are different types of neural networks; most of them have common terminologies, like the input layers, hidden layers, and output layers. Neural networks aim to predict the future based on weights assigned to the network layer. Training the network will be done by changing the weights to minimize the error between the predicted and true values. Once these neural networks are trained, the weights will be fixed, and the neural network will be ready to be used for prediction. In this paper, the Back Propagation Neural Network will be used to mode the hardness data as a function of the aging time and temperatures.

2.1.3. Back Propagation Neural Network (BPN)

Back Propagation Neural Network (BPN) is a multilayer network that has a mathematical foundation. The design of a BPN-NN consists of three separate layers as shown in Figure 2 [19]. The input layer is the set of source nodes (sensor units), while the second layer is single or multiple numbers of the hidden layer. The output layer gives the response of the network based on the activation patterns applied to the input layer. The input will be propagating from the left to the right. Sometimes BPN is also called feed-forward networks, as there is no feedback to adjust the system. Each arrow between the input layers and hidden layers, as well as between the hidden layers and output layers, is associated with weight; the value of the weights is the main concern and objective behind training the BPN network. The hidden nodes will use a linear basis function to sum the weighted inputs, and then this sum will go through the sigmoid activation function.

To teach a training set of input-output samples, the BPN provides a computationally efficient method for changing the weights in a feed-forward network, having differentiable activation function units, thereby reducing the computing time [18]. The BPN can be used for prediction after it is trained. The training method for such networks is applying some data samples, assuming first random initial weights, and then the output will be calculated and compared to the real output to calculate the error. Multiple algorithms to minimize this error exist, but the most common is the gradient descent method, which calculates the error function and finds the value of the parameters (weights) that will minimize it using the partial derivative method. Each time the weights are changed, the error is calculated, and then weights should be updated accordingly. These iterations will be conducted until the error is minimized. The Final weights will be saved, and the network is ready for perdition use. One important step besides the training is validation, which is done by using one part of the data that have not been used in training, and the validation error will be calculated. To avoid overtraining, which is also known as memorizing the data, the validation error at each iteration will be checked, and once it starts to increase, training will stop to avoid overtraining.

2.1.4. ANFIS Structure

The structure of the ANFIS model, which is used in this paper, is shown in Figure 3 [20-22]. The structure of the ANFIS has two inputs and one output. Each of the two inputs has three fuzzy terms associated with its value (L, M, and H). This will result in a TSK fuzzy of nine rules as follows [2]:

Rule #1: IF x is S1 AND y is S2 THEN f = c10 + c11x + c12y.

Rule #2: IF x is S1 AND y is M2 THEN f = c20 + c21x + c22y.

Rule #3: IF x is S1 AND y is L2 THEN f = c30 + c31x + c32y.

Rule #4: IF x is M1 AND y is S2 THEN f = c40 + c41x + c42y.

Rule #5: IF x is M1 AND y is M2 THEN f = c50 + c51x + c52y.

Rule #6: IF x is M1 AND y is L2 THEN f = c60 + c61x + c62y.

Rule #7: IF x is L1 AND y is S2 THEN f = c70 + c71x + c72y.

Rule #8: IF x is L1 AND y is M2 THEN f = c80 + c81x + c82y.

Rule #9: IF x is L1 AND y is L2 THEN f = c90 + c91x + c92y.

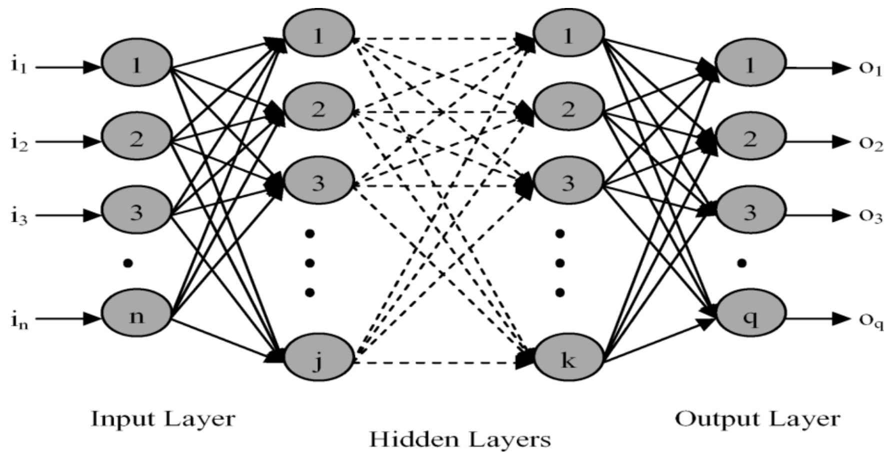

Figure 2. BPN-ANN structure

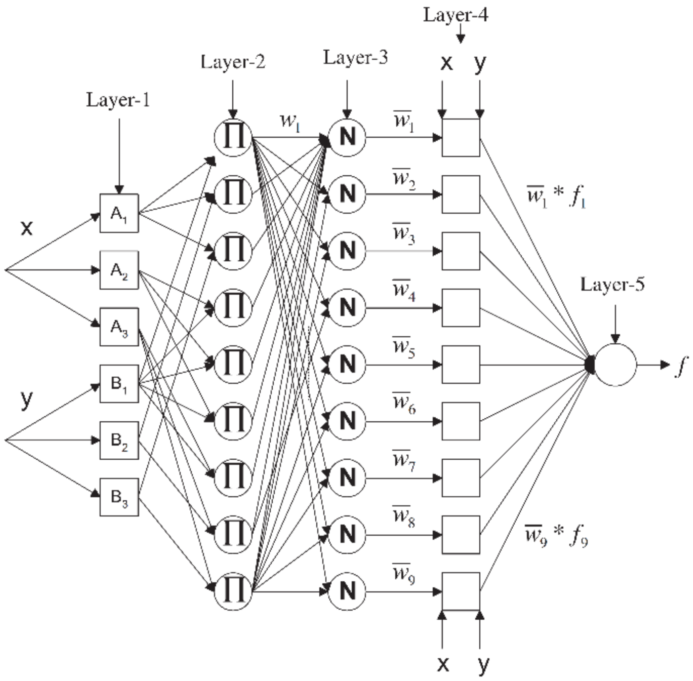

Figure 3. ANFIS two-input one output structure

The membership function that is used to represent each term of the inputs L1, M1 is a generalized Bell function, which has the following mathematical form

$$\mu_{genbell}(x;\ \alpha,\beta,\gamma) = \frac{1}{1+\left|\frac{x-y}{\alpha}\right|^{2\beta}} \tag{2}$$

For this model, eighteen (18) parameter will be needed for each fuzzy term (α,β,γ) because each of the inputs has 3 terms, so the total number of the membership functions will be (6 × 3=18). Since nine rules will be used, Twenty-seven (9 × 3 =27) parameters for the constant values in the outputs (c_{10}, c_{11}…) will be needed.

In the ANFIS training, an initial approximation of the membership functions based on data will be used rather than generating them randomly. This practice usually gives better convergence, and less training will be needed. However, to find the values for the C’s, the least square error method will be used to solve the system of the linear equations to minimize this error. The systems consist of a derivative of the error concerning each value of the C’s with a matrix of coefficients of 34 × 34, which was solved utilizing Matlab. After finding the C’s values, they were fixed, and another epoch through the data was made to fine-tune the (α,β,γ) values using the gradient descent method, followed by another epoch to find the new values of the C’s.

2.2. System Description

The reliability of the lead-free solder is the system that will be modeled in this paper. Since 2002, most of the developed countries started to ban Lead use in the electronic packaging industry because of the toxic effect on the health of humans, animals, and the environment. Soldering is the process in which two or more metals are joined together by melting and flowing a filler metal into the joint, the filler metal having a relatively low melting point compared to the other two alloys [23].

The filler material used in such a process is called solder. One major application of soldering is assembling electronic components in printed circuit boards (PCB) [23]. It was not until recently that the ban on the lead began. However, before this, most of the solder materials were based on the SnPb, which is an alloy that contains both Tin and Lead with different percentages. Many types of research in the past have been conducted to measure the reliability of the Lead solders, and it was somehow stable in terms of reliability. However, following the ban of the lead, there was a need to replace the soldering material with different alloys that do not contain lead: lead-free solders [24-29].

Most of the alloys that are used in today’s electronic industry are a mixture of tin, copper, and silver with different percentages. One major alloy that is being used currently in the manufacturing system is SAC305; this solder alloy is a mixture of 96.5 % Tin (Sn), 3% Silver (Ag), and 0.5% Copper (Cu). However, since this alloy SAC305 is relatively new in the industry, a lot of reliability research is being conducted to compare with other mixtures [24-29]. Our purpose in this report is to model the reliability of this alloy by applying an aging experiment and then checking the hardness as one measure of reliability.

2.2.1. Experiment Description

The experiment was conducted to measure the hardness of SAC305 solder spheres under an aging experiment of different storage temperatures and times. In reality, the solder material will become weaker over time, making the material more prone to failures such as cracks. Therefore, in this experiment, the solder balls had been aged at different times. However, only a short time can be afforded to see these cracks; therefore, another approach had been used. This approach is a controlled accelerated aging test, which had been used intensively in the literature, and it involves heating the solder at different temperatures in a controlled oven for some time (dwell). Aging temperature and dwell time will be utilized through acceleration factors calculation to represent the real-life storage conditions. After the solder spheres had been aged for different periods, a hardness test will be conducted using the Knoop hardness tester shown in Figure 4.

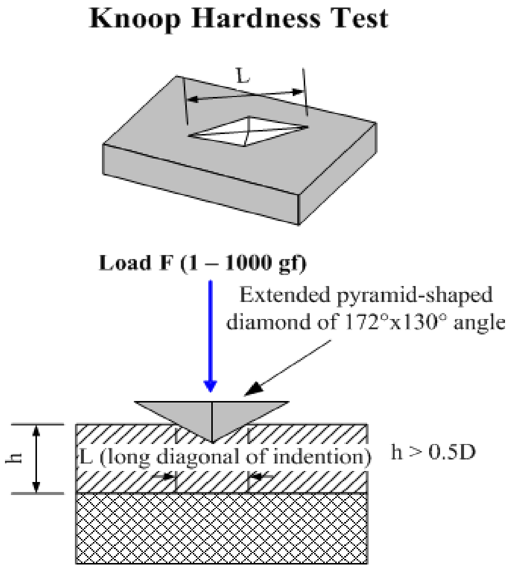

Figure 4. Knoop Hardness Test

2.2.2. Hardness Test:

After the solder material was aged for different times, they had been subjected to a hardness test using a Knoop hardness machine. This machine works as follows:

- A pyramidal diamond point is pressed into the polished surface of the test material with a known force
- The resulting indentation is measured using a microscope
- The Knoop hardness is calculated using the following formula:

$$HK = \frac{Load(kgf)}{Impression\ Area\ (mm^2)} = \frac{P}{C_p L^2} \quad (1)$$

Where

L = Length of the indentation along its long axis

C_p = Correction factor related to the shape of the indenter = 0.070279

P = Load

The hardness test results shown in Figure 5 were collected by measuring the hardness values of different aged solder samples. The figure represents one phase of the experiment where some of the data were collected; hardness decreased as aging temperature increased while hardness decreased with increasing the aging (dwell) period at a fixed temperature. This indicates that as solder ages, it will get less hard (softer), but authors planned to model this relationship and see how long it will take this solder to become relatively not hard enough to withstand regular operation settings. For this purpose, the authors have used the two inputs temperature and time and the output (hardness) to model this relationship using the Adaptive Neuro-Fuzzy Inference System (ANFIS), and they have compared it to the linear regression model, which is being used frequently. The comparison of both models will be shown in the results section.

3. Data for ANFIS Modeling

Table 1summarizes the data obtained for SAC305 solder material that were aged at different aging temperatures and the time spent (dwell time) in the controlled oven. The first thirty-four (34) data points were utilized to train the ANFIS using Matlab while another 8 points of the data were used for verification to avoid overtraining.

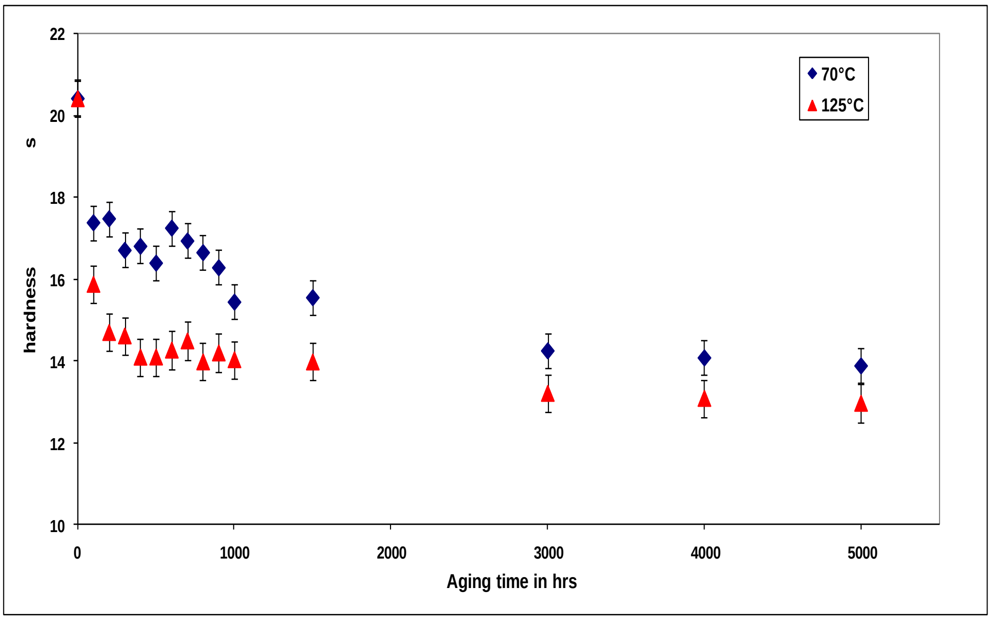

Figure 5. Hardness change with aging time

Table 1. ANFIS Development Data

Temp. (C)	Time (hrs.)	Knoop Hardness	Temp. (C)	Time (hrs.)	Knoop Hardness	Temp. (C)	Time (hrs.)	Knoop Hardness
70	0	20.1	100	0	20.1	125	0	20.1
70	24	19.23	100	24	19.02	125	24	18.21
70	48	18.44	100	48	18.23	125	48	17.54
70	72	18.09	100	72	17.85	125	72	16.23
70	100	17.39	100	100	15.05	125	100	15.88
70	200	17.49	100	200	14.97	125	200	14.7
70	300	16.71	100	300	15.59	125	300	14.62
70	400	16.81	100	400	15.28	125	400	14.1
70	500	16.4	100	500	14.76	125	500	14.1
70	700	16.94	100	700	15.61	125	700	14.5
70	1000	15.45	100	1000	14.5	125	1000	14.04
70	1500	15.56	100	1500	14.34	125	1500	13.98
70	3000	14.26	100	3000	13.11	125	3000	13.21
70	5000	14.22	100	5000	13.09	125	5000	13.09

4. Alternative Approach (Regression)

The regression approach was used to compare and validate the ANFIS model developed. In this case, Minitab was used to fit the input data into multiple models:

4.1. Original Data:

4.1.1. Linear regression model: the output of the Minitab regression model is shown below:

- Regression Equation

Knoop Hardness = 19.15 - 0.0207 Temp. (C)- 0.001013 Aging Time (hrs.)

- **Coefficients**

Term	Coef	SE Coef	T-Value	P-Value	VIF
Constant	19.15	1.16	16.45	0.000	
Temp. (C)	-0.0207	0.0120	-1.73	0.093	1.04
Aging Time (hrs.)	-0.001013	0.000190	-5.33	0.000	1.04

- **Model Summary**

S	R-sq	R-sq(adj)	R-sq(pred)
1.40315	48.36%	45.03%	36.61%

- **Analysis of Variance**

Source	DF	Adj SS	Adj MS	F-Value	P-Value
Regression	2	57.150	28.575	14.51	0.000
Temp. (C)	1	5.903	5.903	3.00	0.093
Aging Time (hrs.)	1	56.035	56.035	28.46	0.000
Error	31	61.033	1.969		
Total	33	118.183			

- **Fits and Diagnostics for Unusual Observations**

Obs	KnoopHardness	Fit	Resid	Std Resid	
14	14.220	12.633	1.587	1.41	*Unusual*
28	13.090	12.011	1.079	0.97	*Unusual*

This model provided the following error parameters:

SE	78.89843
MSE	1.87853
RMSE	1.37060

4.2. Normalized Data: data were normalized by diving every value by the largest available as shown in the equations below and Table 2.

$$Normalized\ Aging\ Temperature = \frac{Temp}{125^oC}$$

$$Normalized\ Aging\ Time = \frac{Time}{5000\ hrs.}$$

$$Normalized\ Knoop\ Hardness = \frac{Knoop\ Hardness}{Knoop\ Hardness\ (at\ time = 0\ \&\ temp = 22^oC)}$$

The de-normalized hardness can be calculated using the equation below:

$$Denormalized\ Dardness = (Normalized\ Hardness * Hardness\ (at\ t = 0\ \&\ RT))$$

4.2.1. Linear regression model: the output of the Minitab regression model is as follow

- **Regression Equation**

Normalized Measurements =0.9854 - 0.1856 Normalized Aging Temp- 0.2305 Normalized Aging Time

- **Coefficients**

Term	Coef	SE Coef	T-Value	P-Value	VIF
Constant	0.9854	0.0515	19.14	0.000	
Normalized Aging Temp	-0.1856	0.0631	-2.94	0.005	1.00
Normalized Aging Time	-0.2305	0.0413	-5.59	0.000	1.00

- **Model Summary**

S	R-sq	R-sq(adj)	R-sq(pred)
0.0735721	50.55%	48.01%	42.81%

- **Analysis of Variance**

Source	DF	Adj SS	Adj MS	F-Value	P-Value
Regression	2	0.21576	0.107881	19.93	0.000
Normalized Aging Temp	1	0.04681	0.046814	8.65	0.005
Normalized Aging Time	1	0.16895	0.168947	31.21	0.000
Error	39	0.21110	0.005413		
Total	41	0.42686			

- **Fits and Diagnostics for Unusual Observations**

Obs	Normalize Measurements	Fit	Resid	Std Resid	
14	0.7075	0.6510	0.0565	0.90	*Unusual*
15	1.0000	0.8369	0.1631	2.26	*Large Residual*
28	0.6512	0.6064	0.0448	0.70	*Unusual*
29	1.0000	0.7998	0.2002	2.82	*Large residual*
42	0.6512	0.5693	0.0819	1.30	*Unusual*

This model provided the following error parameters:

SE	85.28701
MSE	2.030643
RMSE	1.425006

4.2.2. Nonlinear regression model: the output of the Minitab regression model is illustrated below

- **Equation**

Normalized Hardness = -2.33776 *(Normalized Aging Temp^ 0.0777865) + 15.7782 * (Normalized Aging Time^ -0.00218908) - 12.8074

- **Parameter Estimates**

Normalized Measurements = A * 'Normalized Aging Temp' ^ B + C * 'Normalized Aging Time' ^ D +E

Parameter	Estimate	SE Estimate
A	-2.3378	54.317
B	0.0778	1.850
C	15.7782	411.575
D	-0.0022	0.057
E	-12.8074	415.155

- **Summary**

Iterations	200
Final SSE	0.0586358
DFE	37
MSE	0.0015848
S	0.0398089

This model provided the following error parameters:

SE	23.66744
MSE	0.56351
RMSE	0.750673

Table 3. Parameter Summary for All Regression Models

	Original Data Linear Regression	Normalized Data Linear Regression	Normalized Data Nonlinear Regression
SE	78.89843	85.28701	23.66744
MSE	1.87853	2.030643	0.56351
RMSE	1.3706	1.425006	0.750673

As seen in Table 3, the minimum value of the Root Mean Square Error (RMSE) was obtained from all the regression models developed for the hardness measurements. The smallest RMSE value was about 0.75, which is associated with the nonlinear regression model of the normalized data set. This result shows that assuming a linear relationship between the inputs and the outputs is not justified, and a nonlinear relationship exists as shown previously in Figure 5. Therefore, the authors developed an ANFIS model that resulted in a much smaller error, and it will be discussed in the next section.

Table 2. ANFIS Development Normalized Data

Temp. (C)	Time (hrs.)	Knoop Hardness	Temp. (C)	Time (hrs.)	Knoop Hardness	Temp. (C)	Time (hrs.)	Knoop Hardness
0.560	0.000	1.000	0.800	0.000	1.000	1.000	0.000	1.000
0.560	0.005	0.957	0.800	0.005	0.946	1.000	0.005	0.906
0.560	0.010	0.917	0.800	0.010	0.907	1.000	0.010	0.873
0.560	0.015	0.900	0.800	0.015	0.888	1.000	0.015	0.807
0.560	0.020	0.865	0.800	0.020	0.749	1.000	0.020	0.790
0.560	0.040	0.870	0.800	0.040	0.745	1.000	0.040	0.731
0.560	0.060	0.831	0.800	0.060	0.776	1.000	0.060	0.727
0.560	0.080	0.836	0.800	0.080	0.760	1.000	0.080	0.701
0.560	0.100	0.816	0.800	0.100	0.734	1.000	0.100	0.701
0.560	0.140	0.843	0.800	0.140	0.777	1.000	0.140	0.721
0.560	0.200	0.769	0.800	0.200	0.721	1.000	0.200	0.699
0.560	0.300	0.774	0.800	0.300	0.713	1.000	0.300	0.696
0.560	0.600	0.709	0.800	0.600	0.652	1.000	0.600	0.657
0.560	1.000	0.707	0.800	1.000	0.651	1.000	1.000	0.651

5. Results

The hardness of lead-free solder (SAC 305) was modeled as one output measure of the solder material reliability. The hardness was measured for two variables inputs aging temperature and aging time. Using ANFIS to model that data, the results were very reasonable since, after only ten epochs of training, the Root Mean Square Error (RMSE) for the calculated output (hardness) was calculated for the different models based on the formula below:

$$\text{RMSE} = \sqrt{\sum_{i=1}^{n} \frac{(\hat{y}_i - y_i)}{n}^2}$$

$where\ \hat{y} = harndess\ value\ from\ the\ mode\ (predicted)$

$y = actual\ observed\ value$

$n = 42$

The ANFIS model's RMSE value was less than 5%, which is very promising and indicates the ANFIS is a very good choice for modeling this type of output.

Epoch	Training error	Validation error	Epoch	Training error	Validation error
1	0.9099	1.1673	9	0.1351	0.3691
2	0.6974	0.7116	10	0.1093	0.3579
3	0.5631	0.6017	11	0.0891	0.3515
4	0.4431	0.5367	12	0.073	0.3489
5	0.3444	0.4858	13	0.0604	0.3494
6	0.2686	0.4436	14	0.0506	0.3525
7	0.2115	0.4105	15	0.0435	0.3576
8	0.1683	0.3861			

Per Figures 6 and 7, the RMSE from the Matlab output shows that the error was decreasing as more epochs of training were used. However, to avoid the problem of overtraining, the training was stopped after 20 epochs or iterations. Furthermore, the ANFIS output was compared with the linear and non-linear regression models, and it was found that the ANFIS model outperformed the other models with a smaller error of 0.35 for the validation.

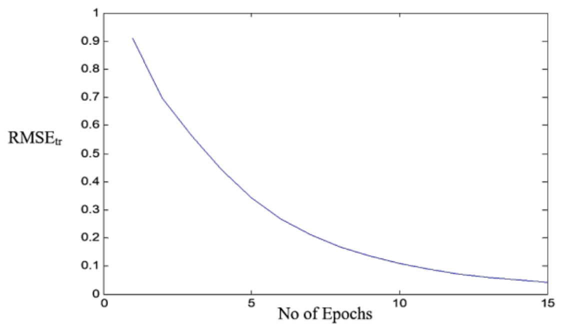

Figure 6. ANFIS Training Error

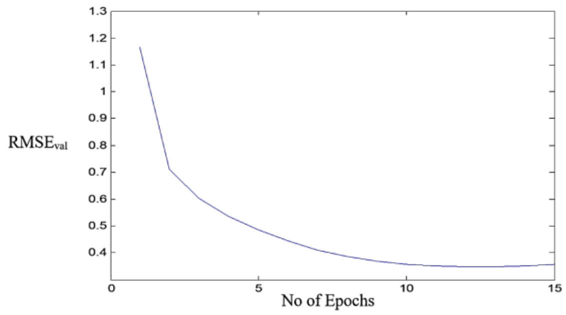

Figure 7. ANFIS Validation Error

6. Conclusion

In this work, the relationship that represents the lead-free solder hardness with respect to the aging temperature and the aging time was modeled using ANFIS. The model gave accurate results in predicting the output (hardness) with a small root mean square error compared to the Minitab linear regression model. Because of this comparison, the ANFIS is a very good technique in modeling non-linear data and it can give a better representation for the data.

ANFIS is a powerful technique in modeling the nonlinear system since in some cases it is difficult to come up with an exact analytical model (ex: differential equations). If the ANFIS is well-trained with small errors, then it can be used for output prediction without measuring the real output, which will save time and cost. It is easy to train the ANFIS again if there is any doubt in the data. Once the ANFIS model is developed, new data could be integrated and the model could be trained again to determine the required parameters, which means there is no need to start from scratch again.

One of the challenges for the ANFIS is to determine the initial values for the parameters, especially for the generalized bell function (membership function) because these values change with the choice of the data. However, developing a code to find these initial values, or by choosing these initial values at random will ease this challenge as the ANFIS model converges, which might require additional epochs.

In the future, the authors are planning to consider other approaches to model the data, comparing these modeling techniques with ANFIS, and utilizing other types of ANFIS configuration.

Conflict of interest

The authors declare that they have no conflict of interest.

References

[1] Mathworks, "Fuzzy Inference Systems", https://www.mathworks.com/help/fuzzy/fuzzy-inference-process.html

[2] Lewis, H. W. (2013). The foundations of fuzzy control (Vol. 10). Springer Science & Business Media.

[3] Çomak, Emre, Ahmet Arslan, and İbrahim Türkoğlu. "A decision support system based on support vector machines for diagnosis of the heart valve diseases." Computers in Biology and Medicine 37.1 (2007): 21-27.

[4] Yu, Jiaqian, and Haibin Duan. "Artificial bee colony approach to information granulation-based fuzzy radial basis function neural networks for image fusion." Optik-International Journal for Light and Electron Optics 124.17 (2013): 3103-3111.

[5] Esfe, Mohammad Hemmat. "Thermal conductivity modeling of aqueous CuO nanofluids by adaptive neuro-fuzzy inference system (ANFIS) using experimental data." Periodica Polytechnica Chemical Engineering 62.2 (2018): 202-208.

[6] Iravani, Pejman, and Chris Brace. "Driving Style Modelling with Adaptive Neuro-Fuzzy Inference System and Real Driving Data." Advances in Human Aspects of Transportation: Proceedings of the AHFE 2018 International Conference on Human Factors in Transportation, July 21-25, 2018, Loews Sapphire Falls Resort at Universal Studios, Orlando, Florida, USA. Vol. 786. Springer, 2017.

[7] Iravani, Pejman, and Chris Brace. "Driving Style Modelling with Adaptive Neuro-Fuzzy Inference System and Real Driving Data." Advances in Human Aspects of Transportation: Proceedings of the AHFE 2018 International Conference on Human Factors in Transportation, July 21-25, 2018, Loews Sapphire Falls Resort at Universal Studios, Orlando, Florida, USA. Vol. 786. Springer, 2017.

[8] Dehaghani, Amir Hossein Saeedi, and Mohammad Hasan Badizad. "A soft computing approach for prediction of P-ρ-T behavior of natural gas using an adaptive neuro-fuzzy inference system." Petroleum 3.4 (2017): 447-453.

[9] Srokosz, Piotr E., and Marta Bagińska. "Application of adaptive neuro-fuzzy inference system for numerical interpretation of soil torsional shear test results." Advances in Engineering Software 143 (2020): 102793.

[10] Naderpour, Hosein, Masoomeh Mirrashid, and Kohei Nagai. "An innovative approach for bond strength modeling in FRP strip-to-concrete joints using adaptive neuro-fuzzy inference system." Engineering with Computers (2019): 1-18.

[11] Bhiradi, Ishwar, Leera Raju, and Somashekhar S. Hiremath. "Adaptive neuro-fuzzy inference system (ANFIS): modelling, analysis, and optimisation of process parameters in the micro-EDM process." Advances in Materials and Processing Technologies 6.1 (2020): 133-145.

[12] Vafaeenezhad, H., et al. "Application of constitutive description and integrated ANFIS–ICA analysis to predict hot deformation behavior of Sn-5Sb lead-free solder alloy." Journal of Alloys and Compounds 697 (2017): 287-299.

[13] Naderpour, H., and S. A. Alavi. "A proposed model to estimate the shear contribution of FRP in strengthened RC beams in terms of Adaptive Neuro-Fuzzy Inference System." Composite Structures 170 (2017): 215-227.

[14] Manogaran, Gunasekaran, R. Varatharajan, and M. K. Priyan. "Hybrid recommendation system for heart disease diagnosis based on multiple kernel learning with adaptive neuro-fuzzy inference system." Multimedia tools and applications 77.4 (2018): 4379-4399.

[15] Foroutan, Rauf, et al. "Influence of chitosan and magnetic iron nanoparticles on chromium adsorption behavior of natural clay: adaptive neuro-fuzzy inference modeling." International Journal of Biological Macromolecules 151 (2020): 355-365.

[16] Mamdani, E. H., & Assilian, S. (1993). An experiment in linguistic synthesis with a fuzzy logic controller. In Readings in Fuzzy Sets for Intelligent Systems (pp. 283-289). Morgan Kaufmann.

[17] Wikipedia, “Fuzzy Logic”, https://en.wikipedia.org/wiki/Fuzzy_logic

[18] Application of Neuro-Fuzzy Systems to Behavioral Representation in Computer Generated Forces

[19] Malleswaran, M., Vaidehi, V., Deborah, S. A., & Manjula, S. (2010). Comparison of RBF and BPN neural networks applied in INS and GPS integration for vehicular navigation. Int. J. Electron. Eng. Res, 2, 753-763.

[20] Jang, J. S. R., Sun, C. T., & Mizutani, E. (1997). Neuro-fuzzy and soft computing a computational approach to learning and machine intelligence. IEEE Transactions on automatic control, 42(10), 1482-1484.

[21] J.-S.R.Jang, C.-T.Sun, E.Mizutani. “Neuro-Fuzzy and Soft Computing”PublishedBy Asoke K. Ghosh, PHI Learning Private Limited. 2009

[22] Jantzen, J. (2007). Foundations of fuzzy control (Vol. 209). West Sussex: John Wiley & Sons.

[23] Wikipedia, ”Soldering”, http://en.wikipedia.org/wiki/Soldering

[24] Albrecht, H. J., Brodie, D. S., Gunn, A. J., Muller, W. H., & Reuben, R. L. (2002). A study of microstructural change of lead-containing and lead-free solders. Journal of Surface Mount Technology, 15(2), 30-39.

[25] Meilunas, M., et al., “Resistance Monitoring ofLead-Free Solder Alloys”, Universal InstrumentsArea Array Consortium, October 2000.

[26] Meilunas, M., Primavera, A., & Dunford, S. O. (2002, November). Reliability and failure analysis of lead-free solder joints. In Proc. IPC Conf. (pp. 1-15).

[27] Barbini, D., & Meilunas, M. (2011). Reliability of lead-free LGAs and BGAs: Effects of solder joint size, cyclic strain, and microstructure. SMTA International Proceedings, Fort Worth, Texas, 292.

[28] Tunga, K., Kacker, K., Pucha, R. V., & Sitaraman, S. K. (2004, June). Accelerated thermal cycling: Is it different for lead-free solder? In 2004 Proceedings. 54thElectronic Components and Technology Conference (IEEE Cat. No. 04CH37546) (Vol. 2, pp. 1579-1585). IEEE.

[29] Alghoul, T. M., Yadav, M., Thekkut, S., Sivasubramony, R. S., Greene, C. M., Poliks, M. D., & Shaddock, D. M. (2018, May). Low-Temperature Solder Attach of SnAgCu Bumped Components for a Flexible Hybrid Electronics Based Medical Monitor. In 2018 IEEE 68th Electronic Components and Technology Conference (ECTC) (pp. 948-953). IEEE.

JJMIE

Volume 15, Number 2, June. 2021
ISSN 1995-6665
Pages 191 - 197

Jordan Journal of Mechanical and Industrial Engineering

Numerical Investigation of the Cooling Performance of PCM-based Heat Sinks Integrated with Metal Foam Insertion

Ahmad K. AL-Migdady*, Ali M. Jawarneh, Amer Khalil Ababneh, Hussein N. Dalgamoni

Department of Mechanical Engineering, The Hashemite University,Zarqa 13133 Jordan.

Received July 24 2020 *Accepted December 14 2020*

Abstract

In this study, numerical simulations were carried out to analyze the cooling behavior of PCM-based heat sinks integrated with Aluminum foam. The performance of the PCM based heat sink is investigated under various operating parameters including: metal foam porosity (ε =100%, 97% and 90%), Two different PCMs (RT35HC and RT44HC) and three different values of convective heat transfer coefficient (10, 20, 30 W/m2.K) while keeping the heat flux input constant at 3200 W/m2. Better cooling characteristics were achieved in the heat sink filled with RT35HC when compared to RT44HC based heat sink. The Aluminum foam insertion further decreased the base temperature by almost (6 and 5)°C for the (ε =97% and 90%) respectively when compared to the no-metal foam case (ε =100%). likewise, in the RT44HC based heat sink, a further decrease in the base temperature by almost (5 and 4)°C was reported for the (ε =97% and 90%) cases respectively when compared to the no-metal foam case (ε =100%). The increase in the convective heat transfer coefficient resulted in longer time needed for PCM melting.

Keywords: Aluminum-foam, heat sink, Phase change material "PCM", Electronic cooling;

Nomenclature

Roman Letters			Greek Letters	
A_{mush}	The mushy zone constant		α	Liquid fraction
C_p	Specific heat		β	Thermal expansion coefficient
H, h^*	Enthalpy		ε	porosity
h	Convective heat transfer coefficient		ρ	Density
k	Thermal conductivity		μ	Viscosity
K	Permeability			
L_f	Latent heat of fusion			
p	Pressure			
S_x S_y	Darcy's Momentum sink			
t	Time			
T	Temperature			
T_s	Solidus Temperature			
T_l	Liquidus Temperature			
u	Velocity in x–direction			
v	Velocity in y–direction			

* Corresponding author e-mail: a.k.almigdady@hu.edu.jo.

1. Introduction

The production of multi-purpose compact electronic devices was enormously increased in the past few decades. The performance of these devices is significantly reduced when their temperature is notably increased, and the challenge is to provide these components with effective thermal management systems to prevent overheat. In fact, the failure rate of electronic components is proportional to the temperature rise and according to Mithal [1], the failure decreases by 4% with a temperature rise reduction of only 1 ºC. The conventional forced or natural air-cooled heat sinks that are equipped with fins are the most common ways used for electronic cooling. However, during the past few years many innovative cooling techniques had emerged including heat sinks incorporated with phase-change materials "PCM". PCMs have many advantages including: low cost, wide range of phase temperature transition and large latent heat of fusion which give these materials the ability to absorb large amount of energy with the heat sink being maintained at an almost constant temperature.

The selection for a PCM is dependent on the temperature control needs of the electronic components; since different PCMs would have various thermophysical properties including: the melting range, density, volume expansion, thermal conductivity, specific heats and latent heat of fusion.[2, 3, 4, 5, 6, 7, 8, 9]

Tan et. al [10] numerically studied the effect of power level on metallic enclosure containing PCM " n-eicosane ", Tan et. al [10] numerically studied the effect of power level on metallic enclosure containing PCM " n-eicosane ", the melting rate as well as the temperature rise and melting rate of the metallic casing was proportional to the power dissipation and for very low power level temperature rise was too small to cause melting, and the PCM use inside the heat sink as unjustified. Yang et al. [11] carried out a numerical study to investigate the performance of PCM-based heat sinks for various power levels, they reported that a more stable operation temperature was achieved upon the use of PCM.

Kandasamy et al. [12]numerically and experimentally investigated a heat sink filled with paraffin wax, they considered varying power dissipation levels, orientation of package to gravity, and various melting/freezing times under cyclic steady conditions. They demonstrated that melting rate is proportional to the power input, whereas the thermal performance of the heat sink was insignificantly affected by the package orientation. They also indicated that improvements of the thermal resistance of the PCM will lead to a smaller PCM package for the same cooling requirements.

The main disadvantage of PCMs is that they have low thermal conductivities, and this leads to slow heat transfer rate. To overcome this difficulty, two techniques are mainly used; the first one is concerned with increasing the heat transfer surface area, and this can be achieved mainly by equipping the heat sink with fins with various sizes, shapes and spacing, using multiple PCMs, adding metal matrix, such as metal pipes and Lessing rings to the PCM cavity and increasing the fill volume ratio. The second technique is concerned with improving the overall thermal conductivity of the integrated heat sink, and this is usually done by inserting nano-particles/nano-tubes with high thermal conductivity into the pcm[7].

Hosseinizadeh et al. [13]carried out an experimental and numerical study on the performance of heat sink equipped with internal fins, so the effects of power level, number of fins and the fin thickness were all investigated. The heat sink performance was improved with the increase of the fins number and fins height; however, such performance was little influenced by the fin thickness. Arshad et al. [14] built and tested a heat sink integrated with PCM and equipped with pin fins with square cross section. They considered three heat sinks with different fins number and thickness, but kept the volume fraction of fins to PCM at 9%. The optimum fin thicknesses were estimated for different operating conditions including input dissipating power and PCM volume fractions.

Shatikian et al. [15]performed a numerical study on a PCM based heat sink with internal fins, paraffin wax was used in this study and the results showed that the heat sink performance is highly dependent on the fin geometry as well as the fin efficiency.

Mahmoud et al. [16]experimentally studied a PCM based heat sink with different inserts. They considered six different types of PCMs and six different heat sink configurations, and they found out that heat sinks performance is enhanced with increasing number of fins, in fact, it was observed that the peak temperature was reduced with increasing the fins number. Besides, it was observed that employing honeycomb inserts with lower melting point PCM reduced the operating temperature of the heat sink and hence, honeycomb inserts can be considered as a good alternative for replacing machined fins.

Metal foam insertions; which have low density, high porosity with high surface area to volume ratio as well as high thermal conductivity, are considered excellent thermal conductivity enhancer "TCE" for most PCM based applications such as low temperature [17, 18, 19, 20] and high temperature Latent Heat Thermal Energy Storage units "LHTES" [21, 22, 23].

In this study, the commercial Ansys-Fluent software 15.0 was used to investigate the performance of a two-dimensional configuration of a heat sink integrated with PCM and metal foam composite under three main different operating parameters: metal foam porosity, PCM type and convective heat transfer coefficient between the heat sink boundaries and the surroundings, which is to the best of the authors' knowledge, was not addressed in this approach before.

2. Physical description and mathematical formulation

The proposed configuration of the two-dimensional heat sink is illustrated in Figure 1, the heat sink is composed of a rectangular cavity (46 mm × 30 mm) that is filled with PCM and metal foam composite and is surrounded by uniform solid enclosure of a thickness of 2 mm. A uniform, constant heat flux of 3200 W/m^2 is applied on the lower side of the metal enclosure, whileall other boundaries are subjected to convection heat transfer; three values of convection heat transfer coefficient (h) were chosen in this simulation: h =10, 20 and 30 W/m^2.K. Also, two types of PCM were selected; RT35HC and RT44HC, Furthermore, to account for the metal foam variation three values of metal foam porosity were considered, ε = 1.00, 0.97 and 0.90, where ε = 1.00 refers to no-metal foam case.

Aluminum was selected for both the metal container as well as the porous media due to low density and high thermal conductivity. The thermophysical properties of RT44HC, RT35HC, and Aluminum are listed in Table 1, while the geometric specifications of the porous media used in this study are listed in Table 2.

The size of such heat sink can be applied in practice to many electronic packages that requires cooling like microprocessors and printed circuit boards, besides, the chosen PCMs as well as metal foams are available at reasonable prices.

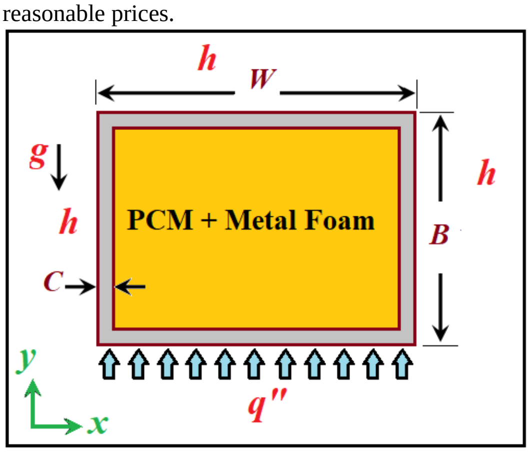

Figure 1.PCM-based heat sink configuration.

Table 1. Thermophysical properties of RT35HC, RT44HC, and Aluminum [24]

	RT35HC	RT44HC	Aluminum
Melting range (°C)	34–36	41–44	–
Latent heat (kJ/kg)	240	250	–
Density (kg/m^3)	*Solid :* 880 *Liquid :* 770	*Solid :* 800 *Liquid :* 700	2719
Specific heat (J/kg-K)	2000	2000	871
Thermal conductivity (W/m-K)	0.2	0.2	202.4
Volume expansion coefficient (1/K)	0.000865	0.00259	–
Dynamic viscosity (Pa s)	*Liquid :* 0.0044	*Liquid :*0.008	–
Thermal diffusivity (m^2/s)	1.33 × 10$^{–7}$	1.21 × 10$^{–7}$	8.2 × 10$^{–5}$

Table 2. Geometric specification of porous media [25]

Porosity	PPI	Fiber Dia (m)	Pore Dia (m)	Inertia coefficient	Permeability m^2
0.9726	5	0.00050	0.00402	0.097	2.7×10^{-7}
0.9005	20	0.00035	0.00258	0.088	0.9×10^{-7}

2.1. The governing equations

The physical domain was modeled based on the following assumptions:

- All materials are considered homogeneous and isotropic throughout, besides metal foams are considered rigid with open cell configuration.
- The liquid phase of PCM is considered as Newtonian and incompressible fluid with an unsteady flow; however, Boussinesq approximation was applied to account for buoyancy effects induced by density.
- PCM density is temperature independent while all other thermophysical properties are not.
- Negligible effects of viscous dissipation as well as radiation heat transfer.

Based on the above, the governing equations will be:

Mass conservation:

$$\frac{\partial u}{\partial x}+\frac{\partial v}{\partial y}=0 \quad (1)$$

Momentum Conservation equations in horizontal and vertical directions are expressed by equation (2) and (3)respectively.

$$\frac{\rho}{\varepsilon}\frac{\partial v}{\partial t}+\frac{\rho}{\varepsilon^2}\left(u\frac{\partial u}{\partial x}+v\frac{\partial u}{\partial y}\right) = -\frac{\partial p}{\partial x}+\frac{\mu}{\varepsilon}\left(\frac{\partial^2 u}{\partial x^2}+\frac{\partial^2 v}{\partial y^2}\right) - \left(\frac{\mu}{K}u+\frac{\rho\, C_f|\vec{V}|}{\sqrt{K}}u\right)-S_x \quad (2)$$

$$\frac{\rho}{\varepsilon}\frac{\partial u}{\partial t}+\frac{\rho}{\varepsilon^2}\left(u\frac{\partial v}{\partial x}+v\frac{\partial v}{\partial y}\right) = -\frac{\partial p}{\partial y}+\frac{\mu}{\varepsilon}\left(\frac{\partial^2 u}{\partial x^2}+\frac{\partial^2 v}{\partial y^2}\right)+\varepsilon\rho\beta g(T-T_{ref}) - \left(\frac{\mu}{K}v+\frac{\rho\, C_f|\vec{V}|}{\sqrt{K}}v\right)-S_y \quad (3)$$

Where: ε, $C_f$and K are porosity, inertial coefficient, and permeability of the metal foam, respectively. While the terms $S_x$and$S_y$stand for source terms added to the momentum equations to account for the liquid fraction in pore volume and computed as:

$$S_x=\frac{(1-\alpha)}{\alpha^3+\sigma}A_{mush}u \;\ldots(4a)\quad and \quad S_y=\frac{(1-\alpha)}{\alpha^3+\sigma}A_{mush}v \quad (4b)$$

Where: $A_{mush}$is known as the mushy zone constant, which controls the amplitude of velocity damping and it also influences the heat transfer and flow characteristics during melting and solidification, and its value has been set at 10^5 and it usually varies within(10^4 - 10^7), while $\sigma$is anotherconstant with small value, usually 0.001, to avoid division by zero, α : the liquid fraction, and it is calculated according to

$$\alpha=\begin{cases}0 & for\ T<T_s\\ \dfrac{T-T_s}{T_l-T_s} & T_s<T<T_l\\ 1 & for\ T>T_l\end{cases} \quad (5)$$

Conservation of energy for the PCM/metal foam composite can be written as

$$\left(\varepsilon\rho C_p+(1-\varepsilon)\rho_m C_{pm}\right)\frac{\partial T}{\partial t}+\varepsilon\rho L_f\frac{\partial\alpha}{\partial t}+\frac{\partial(\rho uH)}{\partial x}+\frac{\partial(\rho vH)}{\partial y}= k_{eff}\left(\frac{\partial^2 T}{\partial x^2}+\frac{\partial^2 T}{\partial y^2}\right) \quad (6)$$

Where $\rho$and $C_p$are the density, specific heat of the PCM, while $\rho_m$and $C_{pm}$are the density, specific heat of the metal foam, and $k_{eff}$is the effective thermal conductivity of the PCM/metal foam composite, although the literature contains numerous formulas for the effective thermal conductivity, Fluent software uses the following simple relation:

$$k_{eff}=\varepsilon k_{PCM}+(1-\varepsilon)k_m \quad (7)$$

$H$is the enthalpy and it is the sum of sensible enthalpy “ h^*”and the latent heat*“ΔH*”*

$$H=h^*+\Delta H^* \quad (8)$$

The sensible enthalpy “ h^*”and the latent heat“ΔH”* *are calculated using the following equations:*

$$h^*=h^*_{ref}+\int_{T_{ref}}^{T}c_{p,eff}dT \quad (9)$$

$$\Delta H=\alpha L_f \quad (10)$$

Where Cp,effis the effective specific heat of the PCM/metal foam composite

$$\rho_{eff}c_{p,eff}=\varepsilon\rho_{PCM}c_{p,PCM}+(1-\varepsilon)\rho_m c_{p,m} \quad (11)$$

Where ρeff is the effective density of the PCM/metal foam composite, which is written as:

$$\rho_{eff}=\varepsilon\rho_{\ PCM}+(1-\varepsilon)\rho_m \quad (12)$$

The specific heat of PCM is given by the following equation

$$C_p = \begin{cases} C_{ps} & for\ T \leq T_s \\ C_{ps}(1-\alpha) + C_{ps}(\alpha) + \dfrac{\Delta H}{T_l - T_s} & T_s < T < T_l \\ C_{pl} & for\ T \geq T_l \end{cases} \qquad 13)$$

Here, C_{ps}, C_{pl}, T_s, T_l, and ΔH are the specific heat of solid, specific heat of liquid, solidus temperature, liquidus temperature, and latent heat of the PCM, respectively.

2.2. Numerical setup: initial and boundary conditions

At the start of the simulation the whole arrangement is in thermal equilibrium with surroundings at T_∞=298 K, also horizontal and vertical components of velocity are zero; u = v = 0.

As simulation proceeds, the following boundary conditions are considered:

- At the container walls, horizontal and vertical components of velocity are zero; u = v = 0
- Continuous heat flux at the outer "cold" enclosure boundaries; *cold boundaries: upper, left and right sides of the enclosure and the hot boundary: the heated lower side.*

$$-k\frac{\partial T}{\partial n} = h\,(T - T_\infty) \qquad (14)$$

- Continuous heat flux between the inner container boundaries and PCM-foam composite interfaces, as:

$$-\left(k\frac{\partial T}{\partial n}\right)_{PCM} = -\left(k\frac{\partial T}{\partial n}\right)_{Al} \qquad (13)$$

The physical problem described above was modeled, and governing equations were solved using Ansys Fluent 15.0 commercial software which uses the enthalpy-porosity technique to model the phase change process. In this technique, the liquid fraction, which is associated with each control volume in the domain, is computed at each iteration by applying enthalpy balance. The liquid-solid mushy zone is treated as a porous zone with porosity equal to the liquid fraction, and appropriate momentum sink terms are added to the momentum equations to account for the pressure drop caused by the presence of solid material.

Initially, both the system and the surroundings are in thermal equilibrium at 298 K; this thermal equilibrium is disturbed by imposing a constant heat flux of 3200 W/m^2 at the lower side of the metal enclosure and the convective heat transfer boundary condition was applied on all the other enclosure sides. A quadrilateral mesh of about 13600 elements was suitable of all cases with time step of 0.2 seconds.

2.3. Model Validation

The numerical approach was validated by simulating an independent model and comparing to the work of Sunuku et al.[24]. Their work included the simulation of a two-dimension heat sink(30 cm × 50 cm) with an Aluminum enclosure of 2.0 mm thickness, the heat sink was further subdivided by 2 vertical slabs of 2.0 mm thickness each and space created by the enclosure was filled with RT44HC with the base being subjected to a constant heat flux. The time evolution of melt fraction for three values of constant heat flux for the current work and that of Sunuku[24] are presented in Figure2 and a satisfactory agreement between the results of the two works exists.

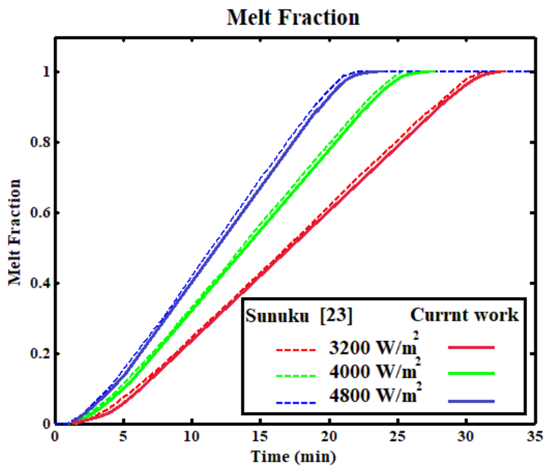

Figure 2. Average melt fraction variation with time, comparison between this study and that of Sunuku[24] .

3. Data and results

As mentioned earlier, the PCM based heat sink was studied for a fixed heat flux of 3.2 kW/m^2, two PCM types: RT35HC and RT44HC and three porosity values: ε = 1.00, 0.97 and 0.90, where ε = 1.00 refers to no-metal foam case. Besides, convection heat transfer takes place at outer enclosure cold sides with the surroundings, three values of the convective heat transfer coefficient were considered: h= 10, 20 and 30 W/m^2.K. Figures 3 and 4 show the time evolution of melt fraction and the average base temperature variation with time for the RT35HC and RT44HC heat sinks integrated with metal foam (ε = 1.00, 0.97 and 0.90) and convective heat transfer coefficient of 10 W/m^2.K. In the no-metal foam case (ε = 1.00), PCM starts receiving heat from the adjacent hot surface and its temperature rises in that vicinity and once the melting temperature is reached, it starts melting. At the early stages of melting conduction heat is much significant and as melting continues, the solid region size gets smaller and conduction is present in the solid matrix while convection dominates the heat transfer process within the molten region. In fact, convection currents are formed due to buoyancy effects caused by temperature gradients and consequently mixing is enhanced and the PCM is eventually totally melted. During the melting process, the PCM temperature rise is limited by its solidus and liquids temperature range and accordingly the base temperature variation is low, and the base temperature profile has a small slope during melting.

Melting starts sooner in the no-metal foam case (ε = 1.00) since metal foam insertion enhances heat transfer from the base and the PCM cavity to the cold sides of the container, in other words, the thermal conductivity is enhanced with the addition of the porous media. Indeed, melting time is inversely proportional to porosity, besides, the base temperature rise during melting is inversely proportional to porosity as well. The time required for melting was (47, 37, 34) minutes for (ε = 1.00, 0.97 and 0.90) cases respectively. However, base temperature variation within the melting region was approximately between (42°C and 43°C), (37°C and 38°C) and (36°C and 37°C) for (ε = 1.00, 0.97 and 0.90) cases respectively. In other words, a base temperature reduction of about (5–6)°C was achieved by using high porosity metal foams. However, the base temperature difference during melting between the (ε = 0.97 and 0.90) cases was only 1°C.

A similar behavior was noted in the RT44HC cases, where base temperature variation within the melting region was approximately between (48 °C and 50°C), (44 °C and 45°C) and (43 °C and 44°C) for (ε = 1.00, 0.97 and 0.90) cases respectively and a base temperature reduction of about (4–5) °C was achieved by using high porosity metal foams and again the base temperature difference during melting between the (ε = 0.97 and 0.90) cases was about only 1°C. However, the estimated time for melting was (44, 39, 37) minutes for (ε = 1.00, 0.97 and 0.90) cases respectively.

Figure 5 illustrates the effect of heat transfer coefficient on the cooling performance of heat sink filled with RT35HC. As the convective heat transfer increases, the rate of heat rejection from the heat sink increases and the PCM needs more time to melt. For the convective heat transfer coefficient value of 20 W/m^2.K the melting time was (50, 40,37) minutes for the (ε = 1.00, 0.97 and 0.90) cases respectively. whereas for the 30 W/m^2.K value the melting time was (43, 40) minutes for (ε = 0.97 and 0.90) cases respectively, however, the simulation was terminated for the (ε = 1.00) case at 50 minutes and melt fraction was about 92%.

Figure 6 shows the time evolution of temperature distribution within the RT35HC based heat sink for cases of ε = 1.00 and ε = 0.97 at convective heat transfer coefficient of 20 W/m^2.K. In the no-metal foam case, heat is transferred from heat source and container boundaries to the cavity, and PCM starts melting in the outer region towards the center. In fact, the container boundaries contribute to a significant amount of heat to be transferred to the PCM due to the high thermal conductivity of the Aluminum enclosure compared to that of the PCM. At the same time, the rest of heat is dissipated at the container outer cold sides by convection. With continuous heating, the PCM at the cavity boundaries is totally molten and its temperatures rises, nevertheless, less heat is received by the center of the PCM due to its low thermal conductivity hence slight increase in temperature is observed with slow propagation rate of the molten region.

Upon the addition of metal foam, thermal conductivity of the PCM is remarkably enhanced as well as heat transfer rate through the PCM towards the container boundaries, as a result the temperature distribution within PCM and enclosure boundaries becomes more uniform. Besides, as it can be noted from figure 6, the container base temperature as well as that of the container boundaries are reduced when compared to the no-metal foam case. In fact, upon the addition of metal foam, thermal conductivity within the PCM cavity is enhanced and consequently heat flow towards the container cold sides is significantly improved and hence better cooling is achieved upon enhanced heat rejection at the outer sides of the enclosure.

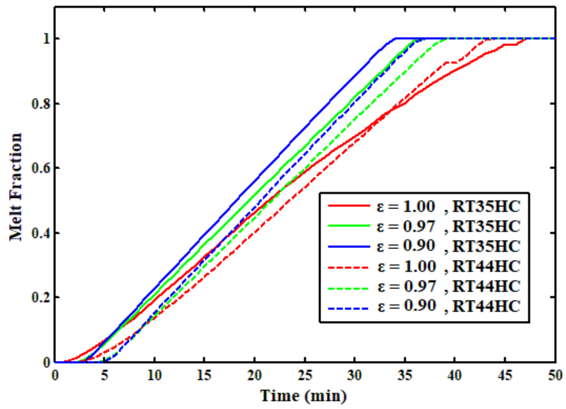

Figure 3. Time variation of Average melt fraction at h=10W/m^2.K.

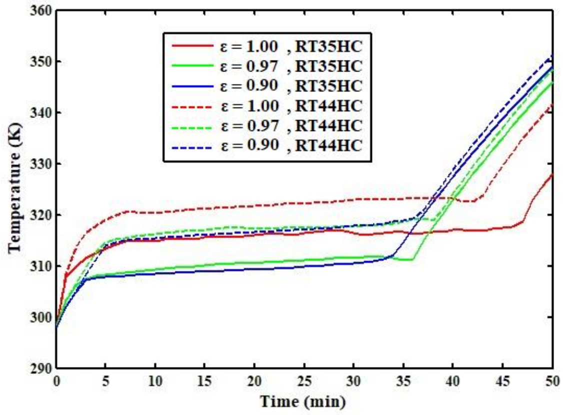

Figure 4. Time variation of the average base temperature at h=10W/m^2.K.

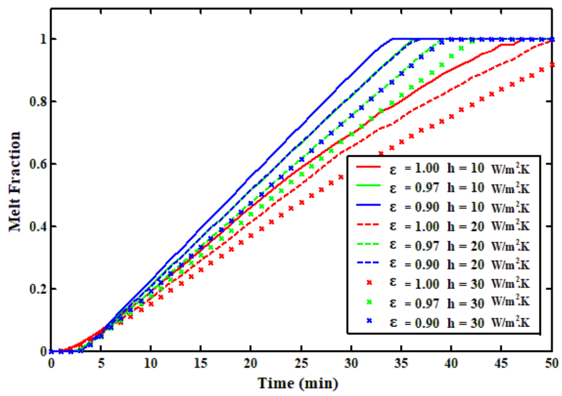

Figure 5. Time variation of the average melt fraction for the RT35HC based heat sink for different values of convective heat transfer coefficients.

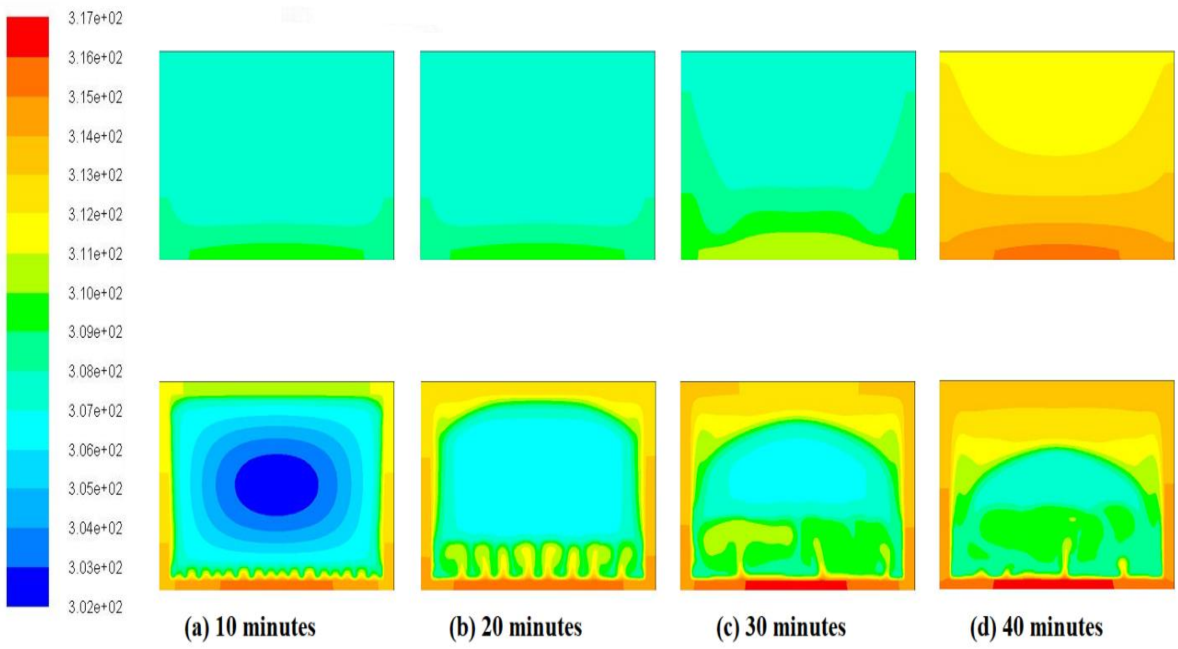

Figure06. Evolution of temperature contours for the RT35HC based heat sink at a convective heat transfer coefficient of 20 W/m^2.K; ε= 0.97 top row , ε=1.00 bottom row.

Conclusions

The metal foam insertion significantly enhanced the performance of the heat sink, it improved the overall thermal conductivity within the enclosure cavity, increased the heat transfer rate from the hot surface towards the cold sides of the metal enclosure and caused a more uniform temperature distribution within the PCM. In fact, the improved heat transfer out of the heat sink resulted in temperature reduction in both the hot and cold sides of the enclosure, besides, the melting time was also reduced as well.

In the RT35HC based heat sink, the Aluminum foam insertion of (0.97 and 0.90)porosity caused a base temperature reduction of (5 and 6)°C respectively when compared to that of no-metal foam case with the three values of convective heat transfer coefficient.

In the RT44HC based heat sink, the Aluminum foam insertion of (0.97 and 0.90) porosity caused a base temperature reduction of (4 and 5)°C respectively when compared to that of no-metal foam case with the three values of convective heat transfer coefficient.

Increasing the convective heat transfer coefficient reduced the melting rate of the PCM due to the heat rejection increase from clod sides of the heat sink and kept the base at reduced temperature for longer duration.

References

[1] P. Mithal, "Design of experimental based evaluation of thermal performance of a flichip electronic assembly," *ASME EEP Proceedings. New York: ASME,* vol. 18, p. 109–15, 1996.

[2] S. Sahoo, M. Das and P. Rath, "Application of TCE-PCM based heat sinks for cooling of electronic components: A review," *Renewable and Sustainable Energy Reviews,* vol. 59, pp. 550-582, 2016.

[3] M. Kensarian, "High-temperature phase change materials for thermal energy storage," *Renewable Sustainable Energy Reviews,* vol. 14, p. 955–970, 2010.

[4] H. Ge, H. Li, S. Mei and J. Liu, "Low melting point liquid metals as a new class of phase change material: an emerging energy frontier," *Renewable Sustainable Energy Reviews,* vol. 21, p. 331–346, 2013.

[5] S. Khare, M. Dell'Amico, C. Knight and S. McGarry, "Selection of materials for high temperature latent heat energy storage," *Solar Energy Materials & Solar Cells,* vol. 107, p. 20–27, 2012.

[6] M. A. Y. C. Wang X. Q., "Effect of orientation for phase change material (PCM)-based heat sinks for transient thermal management of electric components," *International Communications in Heat and Mass Transfer,* vol. 34, no. 7, p. 801–808, 2007.

[7] A. K. AL-Migdady, A. M. Jawarneh, H. N. Dalgamoni and M. Tarwaneh, "Combined Effects of Eccentricity and Internal Fins on the Shell and Tube Latent Heat Storage Systems," *International Journal of Recent Technology and Engineering (IJRTE), Volume-9 Issue-1, May 2020,* vol. 9, no. 1, pp. 230-236, 2020.

[8] M. Hamdan, M. Shehadeh, A. Al Aboushi, A. Hamdan and E. Abdelhafez, "Photovoltaic Cooling Using Phase Change Material," *Jordan Journal of Mechanical and Industrial Engineering,* vol. 12, no. 3, pp. 167-170, 2018.

[9] M. M. Al-Maghalseh, "Investigate the Natural Convection Heat Transfer in A PCM," *Jordan Journal of Mechanical and Industrial Engineering,* vol. 11, no. 4, pp. 217-223, 2017.

[10] F. Tan and C. Tso, "Cooling of mobile electronic devices using phase change materials," *Applied Thermal Engineering,* vol. 24, p. 159–169, 2004.

[11] Y. Yang and Y. Wang, "Numerical simulation of three-dimensional transient cooling application on a portable

electronic device using phase change material," *International Journal of Thermal Sciences,* vol. 51, p. 155–162, 2012.

[12] R. Kandasamy, X. Wang and A. Mujumdar, "Application of phase change materialsin thermal management of electronics," *Applied Thermal Engineering,* vol. 27, p. 2822–2832, 2007.

[13] S. Hosseinizadeh, F. Tan and S. Moosania, "Experimental and numerical studies on performance of PCM-based heat sink with different configurations of internal fins,," *Applied Thermal Engineering,* vol. 31, no. 17-18, p. 3827–3838., 2011.

[14] A. Arshad, H. Ali, W. Yan, A. Hussein and M. Ahmadlouydarab, "An experimental study of enhanced heat sinks for thermal management using n-eicosane as phase change material,," *Applied Thermal Engineering,* vol. 132, no. 5, pp. 52-66, 2018.

[15] V. Shatikian, M. Ziskind and R. Letan, "Numerical investigation of a PCM-based heat sink with internal fins,," *International Journal of Heat and Mass Transfer,* vol. 48, p. 3689–3706, 2005.

[16] S. Mahmoud, A. Tang, C. Toh, R. AL-Dadah and S. Soo, "Experimental investigation of inserts configurations and PCM type on the thermal performance of PCM based heat sinks," *Applied Energy,* vol. 112, p. 1349–1356, 2013.

[17] W. Li, Z. Qu, Y. He and W. Tao, "Experimental and numerical studies on melting phase change heat transfer in open-cell metallic foams filled with paraffin," *Applied Thermal Engineering,* vol. 37, p. 1–9, 2012.

[18] S. Mancin, A. Diani, L. Doretti, K. Hooman and L. Rossetto, "Experimental analysis of phase change phenomenon of paraffin waxes embedded in copper foams," *International Journal of Thermal Sciences,* vol. 90, pp. 79-89, 2015.

[19] B. Zalba, J. Marín, L. Cabeza and H. Mehling, "Review on thermal energy storage with phase change:materials, heat transfer analysis and applications," *Applied Thermal Engineering,* vol. 23, no. 3, p. 251–283, 2003.

[20] C. Zhao, W. Lu and Y. Tian, "Heat transfer enhancement for thermal energy storage using metal foams embedded within phase change materials (PCMs)," *Solar Energy,* vol. 84, no. 8, p. 1402–1412, 2010.

[21] J. Yang, X. Du, L. Yang and Y. Yang, "Numerical analysis on the thermal behavior of high temperature latent heat thermal energy storage system," *Solar Energy,* vol. 98, p. 543–552, 2013.

[22] J. Yang, L. Yang, C. Xu and X. Du, "Numerical analysis on thermal behavior of solid-liquid phase change within copper foam with varying porosity," *International Journal of Heat and Mass Transfer,* vol. 84, p. 1008–1018, 2015.

[23] C. Zhao and Z. Wu, "Heat transfer enhancement of high temperature thermal energy storage using metal foams and expanded graphite.," *Solar Energy Materials & Solar Cells,* vol. 95, p. 636–643., 2011.

[24] J. Sunku Prasad, R. Anandalakshmi and P. Muthukumar, "Numerical investigation on conventional and PCM heat sinks under constant and variable heat flux conditions. ," *Clean Techn Environ Policy,* 2020.

[25] V. V. Calmidi and M. R. L., "Forced convection in high porosity metal foams," *Journal of Heat Transfer,* vol. 122, no. 3, pp. 557-565, 2000.

JJMIE

Volume 15, Number 2, June. 2021
ISSN 1995-6665
Pages 199 - 207

Jordan Journal of Mechanical and Industrial Engineering

Optimization of Performance and Exhaust Emissions of a PFI SI Engine Operated with Iso-stoichiometric GEM Blends Using Response Surface Methodology

Farooq Sk[a*], D. Vinay Kumar[b]

[a]*Assistant Professor , Department of Mechanical Engineering , Vignan's Foundation for Science Technology and Research, Vadlamudi-522213, Andhra Pradesh, India.*

[b]*Associate Professor, Department of Mechanical Engineering , Vignan's Foundation for Science Technology and Research, Vadlamudi-522213, Andhra Pradesh, India.*

Received June 24 *2020* *Accepted* May *1 2021*

Abstract

The present work aimed at optimizing the performance and emission characteristics of a Port Fuel Injection (PFI) SI engine fueled with Gasoline-Ethanol-Methanol (GEM) blends using Response Surface Methodology (RSM). Test fuels used in the study are pure gasoline (E0), E10, E10 equivalent iso-stoichiometric GEM blend (E10_Eq), E20, E20 equivalent iso-stoichiometric GEM blend (E20_Eq). Formulated E10 and E20 equivalent blends have identical air-fuel ratios, lower heating values, density, and octane number as target binary blends (E10, E20). The test engine was operated with different fuel blends by varying the engine speed from 1700 to 3300 rpm at a constant engine load of 5 kg. For optimization of the engine, speed and fuel blends were considered as input parameters and brake thermal efficiency (B_The), brake specific fuel consumption (BSFC) and, nitrogen oxide (NOx) emissions as responses. Optimization was carried out using the desirability approach with a target of maximizing the B_The and minimizing the BSFC and NOx. From the results, it was observed that the E10_Eq GEM blend operation of the test engine has optimized values of B_The, BSFC, and NOx emissions with values of 33.17%, 251 g/kW-hr, and 1389.8 ppm respectively at an engine speed of 2416 rpm. A composite desirability value of 0.64 obtained from the regression model shows that RSM can be conveniently employed to determine the significant factors that could impact engine performance and emissions.

Keywords: GEM blends, Response surface methodology, Analysis of variance, Equivalent blends;

Nomenclature

Abbreviations

ANOVA	Analysis of Variance
A/F	Air Fuel ratio
BSFC	Brake specific fuel consumption
B_The	Brake thermal efficiency
CO	Carbon monoxide
DoE	Design of experiments
Eq	Equivalent
E0	Gasoline 100%
E10	Gasoline 90% + Ethanol 10%
E10_Eq	Gasoline 91.6% + Ethanol 5% + Methanol 3.35%
E20	Gasoline 80% + Ethanol 20%
E20_Eq	Gasoline 83% + Ethanol 10% + Methanol 7%
GEM	Gasoline-Ethanol-Methanol
HC	Hydrocarbons
NO_x	Nitrogen oxides
ppm	parts per million
RSM	Response surface methodology
RPM	Revolutions per minute

Symbols

p-value	Probability value
R^2	Coefficient of determination
R^2-(Adj)	Adjusted R^2 value
R^2-(Pred)	Predicted R^2 value

1. Introduction:

Fossil fuels are being consumed worldwide in enormous amounts especially in transportation sector, leading to increase in their demand every year. And also, fast depletion of conventional fossil fuel reserves along with the threat of global warming made research community to explore the alternative eco-friendly bio fuels. Alcohols are an important category of bio fuels which can be produced from variety of biomass in different ways. Also, alcohols are oxygenated fuels and have high latent heat of vaporization and octane number compared to gasoline. Among various alcohols, ethanol and methanol have the potential to be used in internal combustion engines due to fuel properties that are close to gasoline [1].Ethanol is generally produced from biomass feedstock such as sugarcane, potatoes, corn, sugar beets, etc. Although the high demand and utilization of

* Corresponding author e-mail: farooq.314@gmail.com.

ethanol in the present scenario, it is not regarded as a possible effective alternative to fossil fuels in the long run, due to the limitations in biomass of each country [2]. In contrast to this, methanol can be produced from a wide variety of renewable sources such as agricultural by-products, gasification of wood, coal gas, municipal waste, animal and human waste, etc, and at a cheaper price compared to ethanol.

A good amount of literature is available on the usage of alcohol fuels, especially on ethanol and methanol usage in internal combustion engines [3-7]. In almost all the cases, it was reported that the blending of alcohol fuels, at lower volume fractions, improved the efficiency of the test engine while also resulting in improved emission characteristics. Also, because of the expensive nature of the engine experimentation, design of experiments and optimization studies have become popular in the engine research community. There is also a significant amount of literature available on the optimization of various engine parameters. Some authors have reported various models developed in-house for the purpose, while others used different optimization software tools for the same purpose. While each optimization method has its own advantages depending upon the problem complexity, Response Surface Methodology (RSM) is gaining popularity because of its simplicity in modeling and analysis.RSM is a collection of statistical methods that can be used to solve many engineering problems based on modeling and optimization influenced by experimental variables. This method simultaneously analyzes the effects of different factors and the relationship between variables to find an optimum performance condition [8,9].Najafi et al. [10] experimentally studied the performance and emissions of the SI engine using gasoline ethanol blends of E5 to E20 (5%, 10% 15% and 20% (v/v)).Their test results using the blended fuels found to have increased brake thermal efficiency, volumetric efficiency and NOx emissions and, decreased CO and HC emissions.

Elfasakhany [11] experimentally investigated the performance and emission characteristics on a single-cylinder SI engine using gasoline-ethanol, gasoline-methanol, and gasoline-ethanol-methanol blended fuels. The volume fraction of ethanol and methanol was varied from 3%, 7%, and 10% volume. It was reported that the ternary blend EM10 (Gasoline 80% +Ethanol 10%+Methanol10%) showed a significant reduction in CO and HC emissions, by about 46% and 23% respectively compared to other binary gasoline-ethanol and gasoline-methanol blends. Yusuf et al. [12] experimentally investigated the engine emissions, performance, and combustion characteristics of a four-stroke petrol engine using Mbwazirume bio-ethanol blends (5%, 10%, and 15%) with gasoline. The experiments were conducted at different engine speeds, from 1800 to 3000 rpm at 8.5:1 CR with wide-open throttle (WOT) and at a BMEP of 6.7 barat low ambient temperature. The results showed that B_The of the engine increases by 6.7% for E15 blend at an engine speed of 2700 rpm compared to gasoline and the rate of formation of NOx emissions was observed higher for E5 and E10 blends due to advance in combustion timing. Agarwal et al. [13] investigated the performance, combustion, emission characteristics, and particle size distribution of an SI engine using 10% and 20% methanol (M10, M20) blended with pure gasoline fuel. The engine was operated at different torques and speeds, and it was reported that the methanol blended fuels increased the thermal efficiency of the engine and also produced lower CO emissions compared to pure gasoline.

Yusri et al. [14] optimized the performance and emissions of a single-cylinder SI engine operated with gasoline-2 butanol blends of 5%, 10%, and 15% using RSM. The experiments were carried out at a constant torque, 50% wide open throttle, and at various engine speeds, from 2000 to 4000 rpm. It was concluded that the desirability approach of RSM was found to be an efficient optimization technique and the optimum condition was observed at 3205 rpm with a fuel blend of 15%. Abdalla et al. [15] applied RSM to optimize engine performance in terms of brake power, BSFC, NOx, and CO emissions using fuel blends of fusel oil, 10% and 20% with gasoline. The experiments were conducted at engine speeds of 1500-4500 rpm and at15%, 30% 45%, and 60% of wide-open throttle (WOT) positions. A desirability approach was used to determine the optimal multi-response parameters to maximize the brake power and minimize the BSFC, NO_x, and CO emissions. The optimization results were obtained for the engine operation using 20% fusel oil, at 60% WOT, and at an engine speed of 4500 rpm. Ardebili et al. [16] used RSM to optimize the performance and emission characteristics of a port fuel injected gasoline engine using gasoline-fusel oil blends (0%, 20%, 50% 75%, and 100%) at different engine loads at a constant engine speed of 2500 rpm. The engine load and fusel oil content (%) were considered as effective factors and engine performance and emissions as response parameters. Statistical analysis was performed using analysis of variance. It was reported that the optimal fusel oil ratio and the engine load were found at 25% and 47.21% respectively with a desirability value of 0.63. Najafi et al. [17] employed the RSM to optimize the engine performance for different gasoline-ethanol blends. Ethanol volume concentrations of 5%, 7.5%, 10%, and 15% were added to gasoline and engine speed was varied from 2000 to 4000 rpm. The engine speed and fuel blends were identified as input factors whereas the engine performance, emissions were taken as responses. The desirability approach was used to determine the optimum values of the input parameters. It was reported that the test condition with 10% ethanol at an engine speed of 3000 rpm resulted in the optimum performance and emission values with a desirability value of 0.74.

Extensive experimental investigations have been carried out by researchers using gasoline alcohol binary fuels, in which ethanol was widely used in low to moderate concentrations as a blend component in many parts of the world. Ethanol and methanol have high octane number, high latent heat of vaporization compared to gasoline. Because of this, a concept of ternary blends of Gasoline, Ethanol, and Methanol (GEM) was proposed by Turner et al. [18] in which each ternary blend has iso-stoichiometric air-fuel ratio, identical to that of a conventional equivalent binary gasoline-ethanol blend. The iso-stoichiometric air-fuel ratio property is essential for the formulated blends, to be used as drop-in fuels, not to cause engine operation to become stray outside the pre-determined limits of air to fuel ratio[19]. Sileghem et al. [20] experimentally investigated the E85 (Gasoline 15% + Ethanol 85%) equivalent three GEM blends on 1.8 L SI PFI 4-cylinder engine by varying the engine speed from 1500 to 3500 rpm at a fixed torque of 40 and 80 N-m. It was reported that all the three E85 equivalent GEM blends have nearly the same brake thermal efficiencies, volumetric efficiencies, and heat release rates when compared with binary E85 blend operation of the engine. Chaichan [21] reported the results of an experimental study using a ternary blend of gasoline, ethanol, and methanol (37% gasoline + 20% ethanol+ 43% methanol) on a multi cylinder Mercedes Benz engine. It was reported that the exhaust emissions of CO, HC, and $NO_x$are lower by 46.49%, 25.16%, and 1.75% respectively compared to pure gasoline operation.

From the literature, it is evident that alcohols, as alternate fuels, have a significant potential to improve the performance and reducing the emissions from IC engines. The concept of iso-stoichiometric blends facilitates formulating the various volume fraction combinations of ethanol and methanol by blending with gasoline, based on the availability. Only a limited amount of literature is available on GEM blends potential use in SI engines and addition of experimental knowledge using this concept might result in widespread exploration of use of iso-stoichiometric multi-component alcohol blends in SI engines that could help reduce the fossil gasoline consumption. Therefore, the objective of the present work is to optimize the performance and emission characteristics of a PFI engine fueled with E10, E20 binary blends, and its equivalent GEM blends using response surface methodology (RSM). The fuel blends formulated for the present study are E10 and E20 binary blends along with their equivalent iso-stoichiometric GEM blends (E10_Eq, E20_Eq). The effect of input parameters (fuel blends (%) and engine speed (rpm)) was analyzed on the response parameters (B_The (%), BSFC (g/kW hr), NO_x (ppm)). Response surface methodology was employed to optimize fuel blend composition and engine speed to maximize the B_The and minimize the BSFC and NO_x.

2. Experimental setup and procedure:

The experiments were performed on a single-cylinder, Port fuel injection (PFI), four-stroke SI engine; model Honda GX 200, fitted with an eddy current type dynamometer for loading the engine. The advantage of using PFI is that the engine emits low particulate matter emissions into the environment than a direct injection engine [22]. The detailed schematic diagram of the engine is shown in Fig. 1 and the specification of the engine is shown in Table 1. The engine performance parameters were calculated by measuring the time taken by the engine to consume 20 cc of fuel for a given engine speed. Data acquisition system using 'I.C.Engine soft 9.0' software was used to acquire and analyze the performance data obtained from the engine at different test conditions. The operating parameters of the engine such as spark timing and fuel injection timing were controlled by an open Electronic control unit (ECU), developed by Performance Electronics Ltd, PE3 series system connected to windows based operating system through an Ethernet port. The PE software is installed on a computer for controlling the ignition timing for every engine cycle. The spark timing sweep tests were conducted to determine the maximum brake torque (MBT) at each engine speed for each fuel blend.

Table 1. Engine Specifications

Item Description	Specifications
No. of cylinders	01
No. of Strokes	04
Fuel	Gasoline
Rated Power	4.1 kW @3600 rpm
Cylinder Diameter	68mm
Stroke Length	54mm
Connecting rod length	105mm
Compression Ratio	8.5: 1
Cooling type	Air Cooled

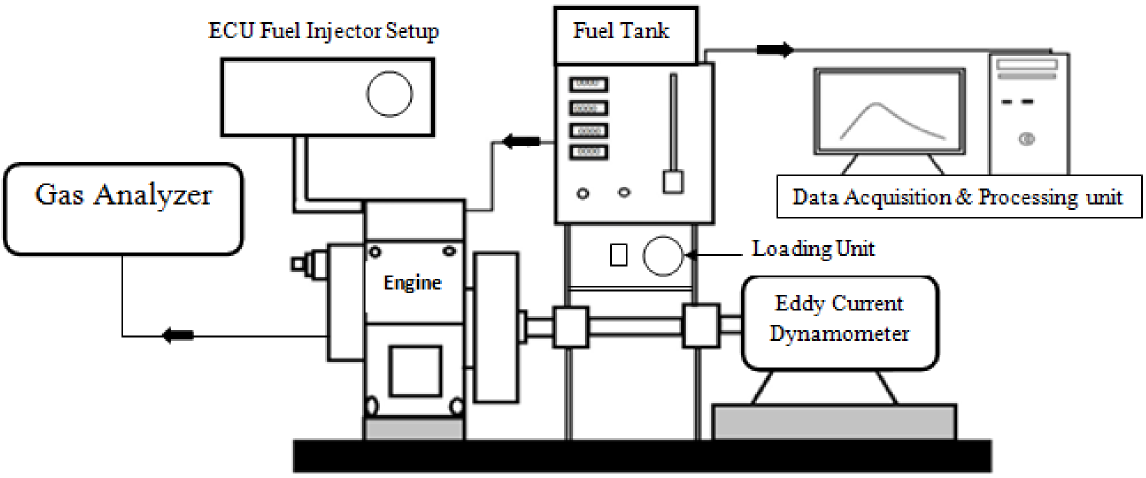

Figure 1. Schematic diagram of single cylinder SI engine

The exhaust emissions were measured using a 5-gas analyzer; model AVL Digas 444N which uses the techniques of Non-Dispersive Infrared (NDIR) absorption, Chemiluminescence and Flame Ionization to measure Carbon monoxide (CO), Nitrogen oxide (NO_x) and unburned Hydro carbons (HC) from the engine. Exhaust gases were purged completely from the stabilizing tank after each measurement.

The tested ethanol and methanol were industrial grade with 99.9% purity. The ethanol and methanol fuels were splash blended with gasoline before filling in the fuel tank. Different properties of gasoline, ethanol, and methanol are presented in Table 2. The basic formulation of iso-stoichiometric blends was carried out using the mathematical formulation given by Pearson et al. [19] in Appendix 2. And also for the determination of binary and ternary blend fuel properties such as iso-stoichiometric air to fuel ratios, lower heating values, and octane number same reference has been followed. The experiments were performed at dry ambient conditions. Five fuel samples were used for the tests namely, pure gasoline, binary E10, and E20, and their equivalent iso-stoichiometric GEM blends on a volume % basis (E10_Eq, E20_Eq).In equivalent GEM blends, the volume of ethanol was reduced to half of its volume than in binary blend. The reduced quantity of ethanol is taken care of by adding gasoline and methanol in suitable proportions to maintain the identical air to fuel ratio as the target binary blend. It can be observed from Table 3 that two formulated equivalent GEM (E10_Eq, E20_Eq) blends have an identical air-fuel ratio, lower heating value, and octane numbers as conventional binary E10 and E20 blends. The experiments were conducted at a constant engine load of 5 kg while varying the engine speed from 1700 to 3300 rpm. During the experiment at each speed, the engine was kept running till it attained a steady state condition. The engine performance and emissions data were recorded for each speed after attaining engine stable operating conditions. The performance tests and emission measurement were repeated 3 times per test and the averaged data value was considered for the investigation.

2.1. Response Surface Methodology (RSM)

RSM can be used to establish the relationship between output responses of the engine to its input parameters using statistical methods and mathematical equations. The input variables can be indicated as X1, X2, X3 ………Xk and response of interest (output) as y as in Eq. (a)

$$Y= f '(X) \beta + \varepsilon \quad \text{(a)}$$

Where X = (X1, X2, X3 ………Xk)', f(x) is a vector function of p elements that consists of powers and cross-products of powers of X1, X2, X3 ………Xkup to a certain degree denoted by d (>1), β is a vector of p unknown constant coefficients referred to as parameters, and ε is a random experimental error assumed to have a zero mean. For a first order polynomial (d = 1), the equation can be described as in

$$y = \beta_o + \sum_{i=1}^{k} \beta_i X_i + \varepsilon \quad \text{(b)}$$

And if the model predicted a curvature, then a polynomial of higher degree is necessary to be used, such the second order model (d=2) can be described as in

$$y = \beta_o + \sum_{i=1}^{k} \beta_i X_i + \sum \sum_{i<j} \beta_{ij} X_i X_j + \sum_{i=1}^{k} \beta_{ii} X_i^2 + \varepsilon \quad \text{(c)}$$

Where‘y’ is the predicted response, ‘i’ is the linear coefficient, ‘j’ is thequadratic coefficient, ‘β’ is the regression coefficient, ‘k’ is the number of factors [16].

In the present work, the engine speed and fuel blend composition were taken as input parameters and the output responses were performance and emission values, B_The, BSFC, and NO_x respectively as shown in Tables 4 and 5. Design of Experiments (DoE) with the multilevel factorial design was used in this study and the modeling and analysis were carried out using Minitab software (Version 17). Engine tests were carried out as per the run order given in Table 6 and the obtained experimental results were analyzed using ANOVA. Regression analysis was carried out to determine the coefficients of the equations which can be used to predict the engine output responses. The optimum combination of engine speed and blend composition was obtained using the desirability approach of RSM. To validate the optimized response parameters, experimental tests were conducted at identified optimum input parameters.

Table 2. Fuel Properties [17]

	Gasoline	Ethanol	Methanol
Molecular Formula	C_4-C_{12}	C_2H_5OH	CH_3OH
Molecular Weight	95-120	46	32
Oxygen content (%)	0	34.73	49.9
Density (kg/m^3)	731	789	791
Lower Heating Value, LHV (MJ/kg)	45.2	26.9	20.09
Research Octane number	95.3	109	109
Motor Octane number	85	92	88.6
Stoichiometric A/F ratio	14.8	9.0	6.5
Latent heat of vaporization (kJ/kg)	305	840	1100
Boiling point, °C	38-204	79	65

Table 3. Properties of Blended fuels

Fuel Component	E0 (G 100)	E10 (G90 E10)	E10_Eq (G 91.65 E 5 M 3.35)	E20 (G 80 E20)	E20_Eq (G 83 E 10 M7)
Stoichiometric A/F ratio	14.8	14.3	14.35	13.8	13.9
Density (kg/m^3)	731	736.3	736	742	741.6
Lower Heating Value (MJ/kg)	45.2	43.3	43.25	41.55	41.6
Research Octane Number, RON	95.3	98.3	98.2	100.5	100.38
Motor Octane Number, MON	85	86.58	86.41	87.7	87.3
Octane Number, ON	90.15	92.44	92.305	93.78	93.705

Table 4

S.No	Input Parameters	Parameters Type	Code	Level				
				1	2	3	4	5
1	Engine Speed (RPM)	Numerical	Speed	1700	2100	2500	2900	3300
2	Fuel Blends (%)	Numerical	Blend	E0	E10	E10_Eq	E20	E20_Eq

Table 5

S.No	Response Factors	Type	Code	Target
1	Brake Thermal Efficiency (%)	Numeric	B_The	Maximization
2	Brake Specific Consumption (g/kW hr)	Numeric	BSFC	Minimization
3	Nitrogen Oxide (ppm)	Numeric	NO_x	Minimization

Table 6. Experimental Design Matrix

Run	Speed (RPM)	Blend (%)	B_The (%)	BSFC (g/kW hr)	NO_x (ppm)
1	3300	E10_Eq	34.30	238.00	1550
2	2900	E10_Eq	34.90	243.00	1680
3	2900	E0	32.50	245.00	1892
4	3300	E20_Eq	35.34	245.10	1990
5	1700	E10_Eq	24.70	325.00	254
6	2500	E10	32.87	265.00	1325
7	3300	E0	33.20	239.90	1700
8	1700	E20	26.29	329.60	350
9	2900	E20	36.10	240.00	1985
10	2500	E0	30.30	261.13	1525
11	2100	E20	32.25	268.70	955
12	2500	E20_Eq	33.17	261.19	1770
13	2100	E20_Eq	32.18	269.23	1050
14	3300	E10	34.10	241.50	1590
15	2500	E20	34.04	254.50	1698
16	2100	E0	28.13	274.64	850
17	2100	E10	30.40	263.50	780
18	2900	E20_Eq	35.26	245.73	2110
19	3300	E20	35.74	244.00	1855
20	1700	E0	23.10	334.65	320
21	2900	E10	34.51	240.00	1700
22	2500	E10_Eq	31.29	262.00	1385
23	1700	E20_Eq	25.16	344.37	360
24	1700	E10	24.90	320.00	245
25	2100	E10_Eq	29.55	265.00	750

3. Results and Discussion:

3.1. Model analysis and evaluation:

The analysis of the developed model was carried out using ANOVA to give the numerical interpretation of the p-value. Table 7 indicates that the model is stable with the p-value being less than 0.0001 and the regression performance indicators like R^2 and R^2 –Adj being in agreement with each other. A high R^2 value, near 100, is desirable and a reasonable agreement with R^2 (Adj) is necessary. ANOVA results of the test data in Table 7 revealed that the values of R^2, R^2 (Adj), and R^2 (Pred) are in the range of 88.34% to 97.1% which indicates that the generated models are accurate. Fig. 2 shows the normal probability plots of residuals for engine response parameters (B_The, BSFC, NO_x). It can be observed from the figure that the majority of the data points form a straight line, signifying the correlation accuracy of regression equations with that of experimental data. The regression equations developed for different response parameters with different input parameters like speed and blend are expressed as below:

B_The = 15.05 + 7.172 Speed + 1.969 Blend - 0.792 Speed*Speed - 0.200 Blend*Blend - 0.0202 Speed*Blend (1)

BSFC = 393.1 - 67.75 Speed - 8.08 Blend + 8.03 Speed*Speed + 1.56 Blend*Blend - 0.250 Speed*Blend (2)

NO_x = -482 + 1090.2 Speed - 272.7 Blend - 124.7 Speed*Speed + 48.8 Blend*Blend + 14.7 Speed*Blend (3)

Table 7. ANOVA outcome for engine responses factors

Responses	B_The	BSFC	NO_x
p	0.00	0.00	0.00
R^2	95.91%	93.72%	97.10%
R^2 (Adj)	94.83%	92.07%	96.34%
R^2 (Pred)	93.24%	88.34%	95.21%

3.2. Effect of input parameters on Brake thermal efficiency (B_The)

Brake thermal efficiency variation with engine speed for different fuel blends is shown in Fig. 3. As it can be observed from the figure, the B_The is lower at lower engine speed and subsequently increases with engine speed. And also, it can be observed that the obtained B_The values of E10_Eq and E20_Eq equivalent ternary blends are identical to the binary E10 and E20 blends test data satisfying the hypothesis proposed by Turner et al. [11] that iso-stoichiometric blends have similar B_The as target binary blends at all engine speeds. Similarly, surface and contour plots presented in Fig. 4 a&b depict the combined effects of fuel blend composition and engine speed on B_The. The B_The of the engine is observed higher for E20 blends at all engine speeds compared to other fuels. This is because the higher alcohol content increases the oxidizing nature of blended fuel and its high latent heat of vaporization causes an increase in brake power and volumetric efficiency of the engine. And also, high laminar burning velocities of alcohols contribute to quick and near complete combustion of the air-fuel mixture by decreasing heat loss from cylinder walls [1]. The average increase in B_The for E10, E10_Eq, E20, and E20_Eq is 6.4%, 5.98%, 11.6%, and 10.8% compared to E0 for a given range of speeds and are in agreement with the results reported by Geo et al.[23].

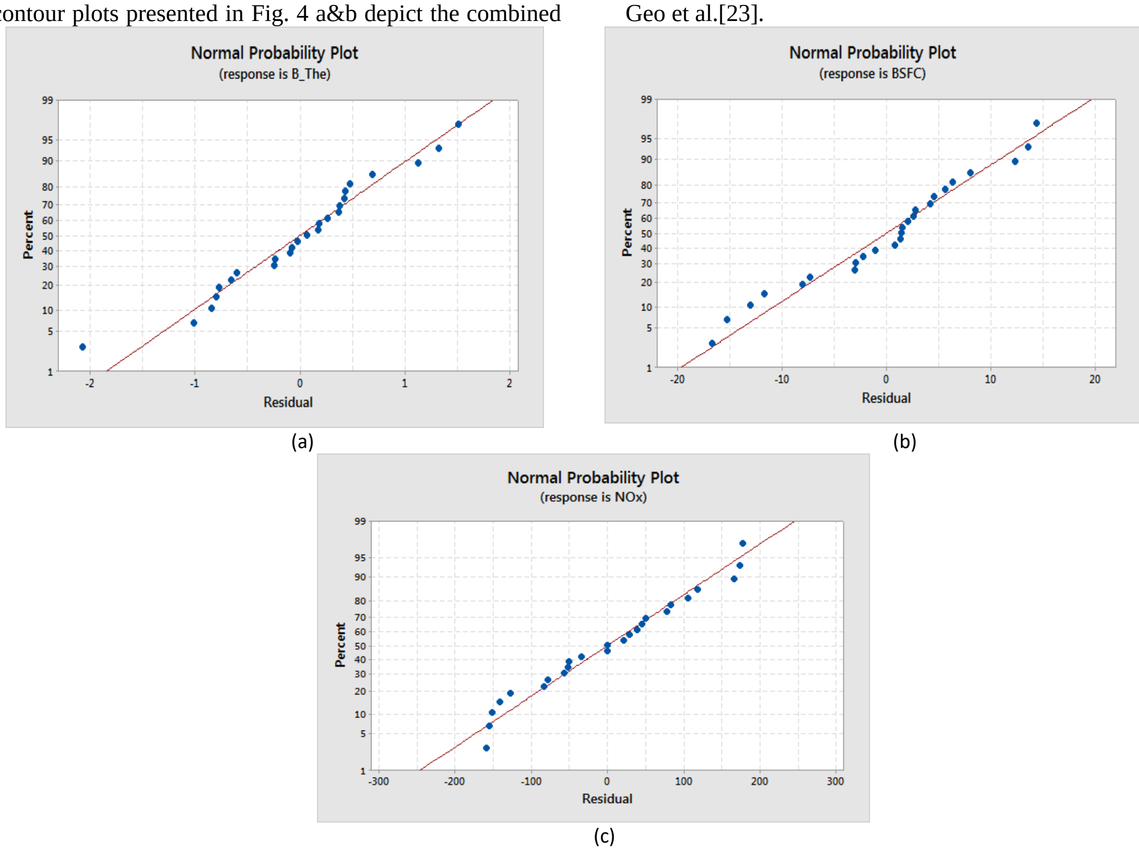

Figure 2. Normal probability plots of residual for (a) B_The, (b) BSFC, (c) NO_x

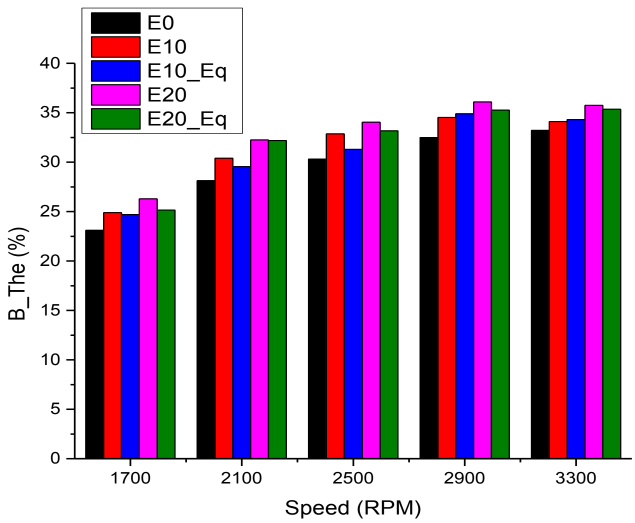

Figure 3. Comparison of B_The of engine for different speeds and blends

3.3. Effect of input parameters on Brake Specific Fuel Consumption (BSFC)

BSFC is defined as the ratio of the rate of fuel consumption to brake power of the engine. Fig. 5 depicts the effect of engine speed and fuel blend on BSFC. From the surface plot, it can be observed that BSFC decreases with an increase in engine speed, whereas the addition of alcohol has a varying effect on it. For E10 and its E10_Eq blends, BSFC decreases by 1.8% and 2.1% when compared to pure gasoline (E0). This is due to the high latent heat of vaporization of alcohols, which increases the density of the air-fuel mixture in an engine cylinder. This causes an increase in the brake power of the engine compared to pure gasoline [5]. But with an increase in ethanol content to 20%, the lower heating value of the blended fuel decreases further compared to pure gasoline, this dominates the increase in brake power of engine for alcohol blended fuels. Thus, to maintain the same speed, the engine consumes more fuel for higher alcohol blended fuels (i.e; E20 and E20_Eq). The average increase in BSFC for E20 and E20_Eq are 1.3% and 1.24% for a given range of speeds compared to E0.

3.4. Effect of input parameters on Nitrogen Oxides (NOx)

Nitrogen oxides (NO_x) formation in the engine cylinder mainly depends on the availability of excess oxygen, in-cylinder temperatures, and engine operating conditions. During the combustion process, nitrogen molecule dissociates at high in-cylinder temperatures and reacts with oxygen molecules, and results in the formation of NO_x emissions [24]. Fig. 6 shows the effect of engine speed and fuel blend composition on the variation of NO_x by using surface and contour plots. It can be observed from the figure that, NO_x emissions decrease by 10.29% and 11.21% for E10 and its equivalent blends compared to pure gasoline. This is due to the high latent heat of vaporization of alcohol blended fuel, which results in lower in-cylinder temperatures inside the engine combustion chamber [23]. But with the further addition of ethanol to 20% by volume and for its equivalent blend, NO_x formation increases compared to pure gasoline. This is due to the increase in excess oxygen concentration inside the cylinder, because of the oxygenated nature of alcohol blended fuels [9]. The average increase in NO_x for E20 and E20_Eq is 9.2% and 10.3% for a given range of speeds compared to E0.

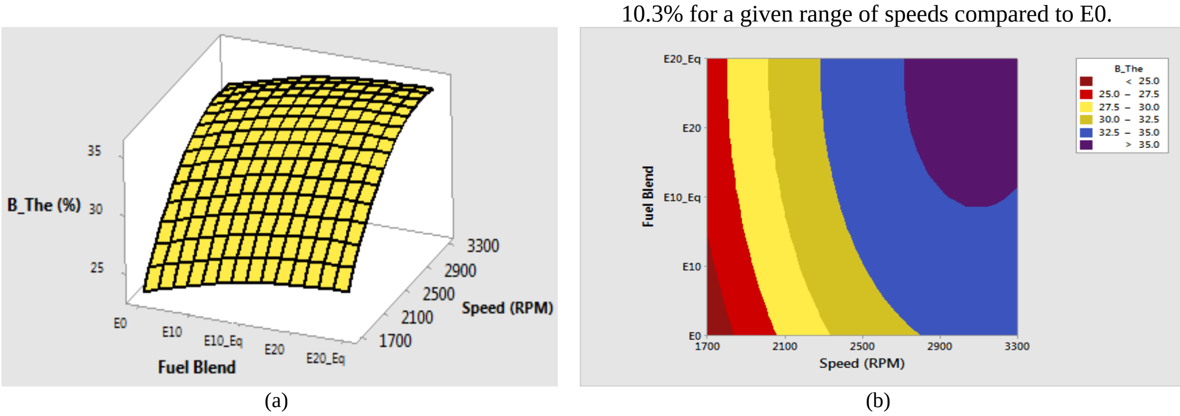

Figure 4. Surface plot and Contour plot of B_The

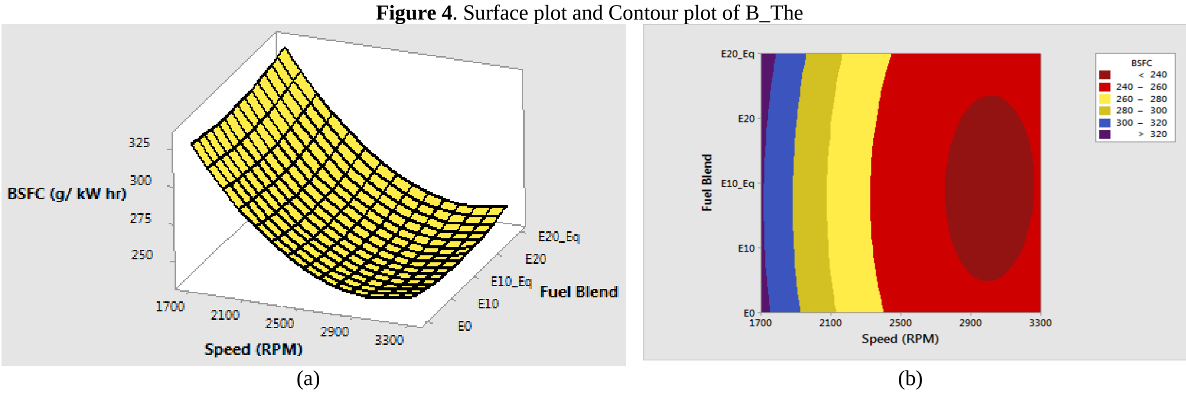

Figure 5. Surface plot and Contour plot of BSFC

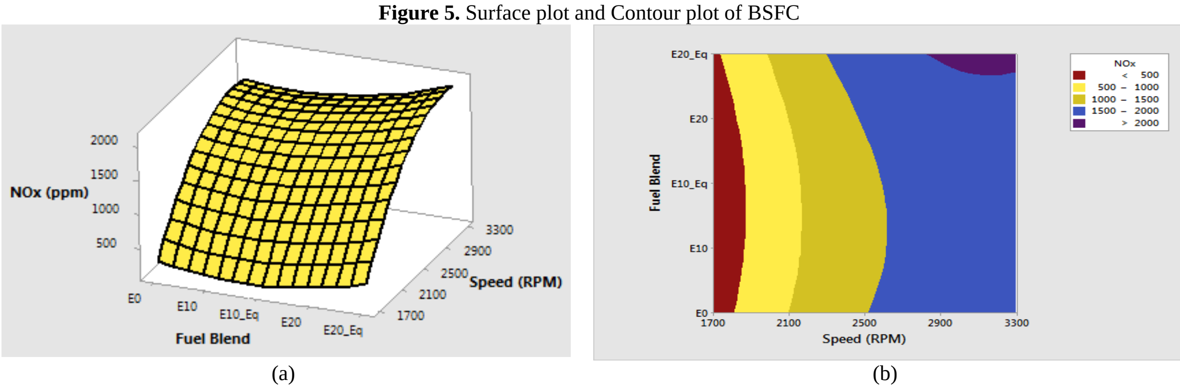

Figure 6. Surface plot and Contour plot of NO_x

3.5. Response optimization:

In the present work, an RSM optimizer was used to determine the optimum combination of B_The, BSFC, and NO_x, with an objective of maximizing the B_The and minimizing BSFC and NO_x. Fig. 7 shows the results of RSM and as it can be seen, optimum values of B_The, BSFC, and NO_x emissions are 33.17%, 251 g/kW-hr, 1389.8 ppm respectively. These optimum values are obtained with a composite desirability value of 0.6401, at input parameters, 2416 rpm of engine speed with E10_Eq blended fuel. The obtained value of composite desirability is similar to the composite desirability value reported by [15, 25].

3.6. Experimental Validation:

To validate the RSM optimum results, engine experiments were carried out at 2416 rpm for E10_Eq blended fuel. The details of the engine experimental responses are shown in Table. 8. The obtained results were compared with the optimized values and it is noticed that the optimized values are in good agreement with the experimental data with an error less than 1.5 %.

Table 8. Validation experiments

Speed (rpm)	Blend	Value	B_The (%)	BSFC (g/kW hr)	NO_x(ppm)
2416	E10_Eq	Predicted	33.17	251	1389.8
		Actual	32.68	248	1361.5
		Error (%)	1.47	1.19	1.01

4. Conclusion:

The present work aimed to find out the optimum engine operating state as to maximize its performance and minimize emission by using RSM. Different gasoline-ethanol-methanol binary and ternary fuel blends and engine speed were considered as input parameters while considering B_The, BSFC, and NO_x as response parameters. The engine tests were performed at constant load and varied speeds from 1700 to 3300 rpm. The obtained results of the gasoline alcohol blend were compared with pure gasoline. The following conclusions have been drawn from the obtained results:

1. Formulated E10 and E20equivalent iso-stoichiometric blends, namely E10_Eq, E20_Eq have identical air to fuel ratio, lower heating values, RON, MON, and Octane number as target E10 and E20 blends.
2. B_The of the engine is similar for equivalent blends at different engine speeds due to the same air to fuel ratios and lower heating values as target binary blends.
3. Adding ethanol and methanol to gasoline increased the brake thermal efficiency of the engine to a maximum of 11.6% for the E20 binary blend.
4. BSFC and NO_x were observed to be decreasing for E10 and its equivalent blends, whereas it was found to be increasing for E20 and its equivalent ternary blends.
5. ANOVA study revealed that the values of R^2, R^2 (Adj), and R^2 (Pred) are in the range of 88.34% to 97.1% for the response factors.
6. The optimized values of B_The, BSFC, and NO_x emissions are 33.17%, 251 g/kW-hr, 1389.8 ppm respectively, when the input parameters are at an engine speed of 2416 rpm using E10_Eq blended fuel with composite desirability of 0.6401.
7. RSM optimum results were confirmed by conducting validation experiments at optimized input conditions namely, at an engine speed of 2416 using E10_Eq fuel blend. The difference between the experimental results and optimized values are in good agreement with other with an error of less than 1.5%.

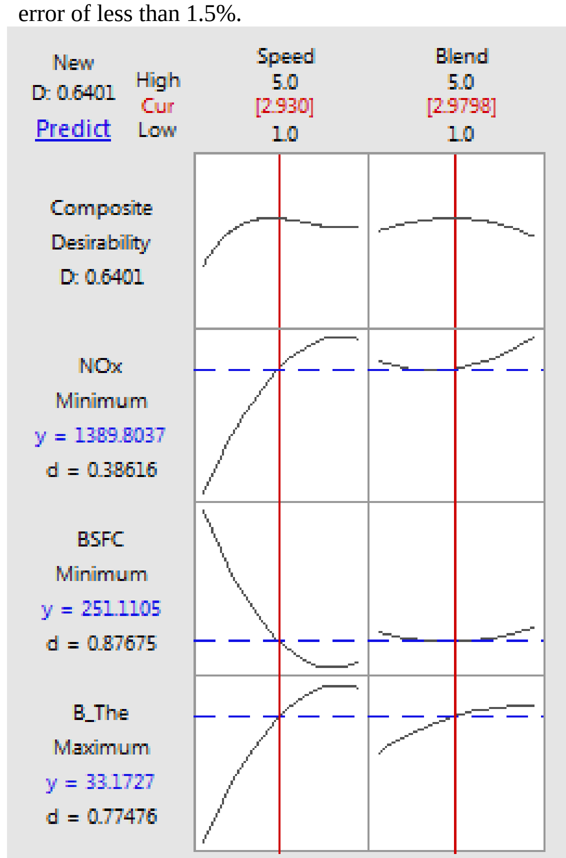

Figure 7. RSM optimizer

References:

[1] Yusuf AA, Inambao FL. Progress in alcohol-gasoline blends and their effects on the performance and emissions in SI engines under different operating conditions. International Journal of Ambient Energy. 2018 Oct 13:1-7.

[2] Turner JW, Pearson RJ, Dekker E, Iosefa B, Johansson K, Ac Bergström K. Extending the role of alcohols as transport fuels using iso-stoichiometric ternary blends of gasoline, ethanol and methanol. Applied Energy. 2013 Feb 1;102:72-86.

[3] Thakur AK, Kaviti AK, Mehra R, Mer KK. Progress in performance analysis of ethanol-gasoline blends on SI engine. Renewable and Sustainable Energy Reviews. 2017 Mar 1;69:324-40.

[4] Awad OI, Mamat R, Ali OM, Sidik NA, Yusaf T, Kadirgama K, Kettner M. Alcohol and ether as alternative fuels in spark ignition engine: A review. Renewable and Sustainable Energy Reviews. 2018 Feb 1;82:2586-605.

[5] Yusuf AA, Inambao FL, Farooq AA. Impact of n-butanol-gasoline-hydrogen blends on combustion reactivity, performance and tailpipe emissions using TGDI engine parameters variation. Sustainable Energy Technologies and Assessments. 2020 Aug 1;40:100773.

[6] Niven RK. Ethanol in gasoline: environmental impacts and sustainability review article. Renewable and sustainable energy reviews. 2005 Dec 1;9(6):535-55.

[7] Verhelst S, Turner JW, Sileghem L, Vancoillie J. Methanol as a fuel for internal combustion engines. Progress in Energy and Combustion Science. 2019 Jan 1;70:43-88.

[8] Yusri IM, Majeed AA, Mamat R, Ghazali MF, Awad OI, Azmi WH. A review on the application of response surface method and artificial neural network in engine performance and exhaust emissions characteristics in alternative fuel. Renewable and Sustainable Energy Reviews. 2018 Jul 1;90:665-86.

[9] Dwivedi SP, Sahu R. Effects of SiC Particles Parameters on the Corrosion Protection of Aluminum-based Metal Matrix Composites using Response Surface Methodology. Jordan Journal of Mechanical & Industrial Engineering. 2018 Dec 1;12(4).

[10] Najafi G, Ghobadian B, Tavakoli T, Buttsworth DR, Yusaf TF, Faizollahnejad M. Performance and exhaust emissions of a gasoline engine with ethanol blended gasoline fuels using artificial neural network. Applied Energy. 2009 May 1;86(5):630-9.

[11] Elfasakhany A.: Investigations on the effects of ethanol–methanol–gasoline blends in a spark-ignition engine: performance and emissions analysis, Engineering Science and Technology, an International Journal, Vol. 18, No. 4, pp. 713-719, 2015.

[12] Yusuf AA, Inambao FL. Effect of low bioethanol fraction on emissions, performance, and combustion behavior in a modernized electronic fuel injection engine. Biomass Conversion and Biorefinery. 2019 Nov 4:1-9.

[13] Agarwal AK, Karare H, Dhar A. Combustion, performance, emissions and particulate characterization of a methanol–gasoline blend (gasohol) fuelled medium duty spark ignition transportation engine. Fuel processing technology. 2014 May 1;121:16-24.

[14] Yusri IM, Mamat R, Azmi WH, Omar AI, Obed MA, Shaiful AI. Application of response surface methodology in optimization of performance and exhaust emissions of secondary butyl alcohol-gasoline blends in SI engine. Energy Conversion and Management. 2017 Feb 1;133:178-95.

[15] Abdalla AN, Tao H, Bagaber SA, Ali OM, Kamil M, Ma X, Awad OI. Prediction of emissions and performance of a gasoline engine running with fusel oil–gasoline blends using response surface methodology. Fuel. 2019 Oct 1;253:1-4.

[16] Ardebili SM, Solmaz H, Mostafaei M. Optimization of fusel oil–Gasoline blend ratio to enhance the performance and reduce emissions. Applied Thermal Engineering. 2019 Feb 5;148:1334-45.

[17] Najafi G, Ghobadian B, Yusaf T, Ardebili SM, Mamat R. Optimization of performance and exhaust emission parameters of a SI (spark ignition) engine with gasoline–ethanol blended fuels using response surface methodology. Energy. 2015 Oct 1;90:1815-29.

[18] Turner J, Pearson R, Purvis R, Dekker E, Johansson K, ac Bergström K. GEM ternary blends: Removing the biomass limit by using iso-stoichiometric mixtures of gasoline, ethanol and methanol. SAE Technical Paper; 2011 Sep 11.

[19] Pearson RJ, Turner JW, Bell A, De Goede S, Woolard C, Davy MH. Iso-stoichiometric fuel blends: characterization of physicochemical properties for mixtures of gasoline, ethanol, methanol and water. Proceedings of the Institution of Mechanical Engineers, Part D: Journal of automobile engineering. 2015 Jan;229(1):111-39.

[20] Sileghem L, Coppens A, Casier B, Vancoillie J, Verhelst S. Performance and emissions of iso-stoichiometric ternary GEM blends on a production SI engine. Fuel. 2014 Jan 30;117:286-93.

[21] Chaichan MT. Gasoline, Ethanol and Methanol (GEM) Ternary Blends utilization as an Alternative to Conventional Iraqi Gasoline to Suppress Emitted Sulfur and Lead Components to Environment. Al-Khwarizmi Engineering Journal. 2016;12(3):38-51.

[22] Yusuf AA, Inambao FL. Effect of cold start emissions from gasoline-fueled engines of light-duty vehicles at low and high ambient temperatures: recent trends. Case Studies in Thermal Engineering. 2019 Sep 1;14:100417.

[23] Geo VE, Godwin DJ, Thiyagarajan S, Saravanan CG, Aloui F. Effect of higher and lower order alcohol blending with gasoline on performance, emission and combustion characteristics of SI engine. Fuel. 2019 Nov 15;256:115806.

[24] Masum BM, Masjuki HH, Kalam MA, Fattah IR, Palash SM, Abedin MJ. Effect of ethanol–gasoline blend on NOx emission in SI engine. Renewable and Sustainable Energy Reviews. 2013 Aug 1;24:209-22.

[25] Sharma A, Ansari NA, Pal A, Singh Y, Lalhriatpuia S. Effect of biogas on the performance and emissions of diesel engine fuelled with biodiesel-ethanol blends through response surface methodology approach. Renewable Energy. 2019 Oct 1;141:657-68.

JJMIE

Volume 15, Number 2, June. 2021
ISSN 1995-6665
Pages 209 - 214

Jordan Journal of Mechanical and Industrial Engineering

Design and Development of a promising Biochar-based Copper Catalyst

Mohammad Hossein Nargesi[a], Reza Yeganeh[a*], Fatemeh Valizadeh kakhki[b], Maryam Hajjami[c]

[a]Department of Biosystems Engineering, Faculty of Agriculture, Ilam University, Ilam, Iran

[b]Department of Soil and Water Engineering, Faculty of Agriculture, Ilam University, Ilam, Iran

[c]Department of Chemistry, Faculty of Sciences, Ilam University, Ilam, Iran

Received September 18 2020 Accepted May 15 2021

Abstract

As about 70 percent of the air pollution comes from vehicles, automotive companies have always been seeking novel catalytic converters to reduce engine emissions. However, so far, a comprehensive research on the impact of copper catalytic converters on biochar has not been conducted. This research aims to study the effect of biochar-based catalytic converter on the amount of exhaust emissions in an XU7 engine. Two thicknesses of the biochar-based catalysts, 7 and 14 cm and Cu (No3)2 in two densities of 1 and 2 mmol were applied for the experiments. Five types of contaminants (i.e., CO, CO2, HC, O2 and NOx) were measured for the evaluation of exhaust emissions. In this study, the XU7 engine, which was produced in 2011, was used to perform the tests. The results showed that the levels of exhaust gases from combustion of the XU7 engine were low and acceptable in all treatments in comparison to the environmental standard. In addition, the catalyst used in the XU7 engine had a significant impact on the absorption of exhaust gas from the engine, especially for CO and the level of its concentration was significantly different in comparison with a new catalyst, biochar-based catalysts and control and also, for HC the levels of concentration were shifted applying biochar-based catalysts comparing to the new catalyst and control. Based on the results, it was observed that applying the proposed approach can be an effective step in reducing greenhouse gas emissions from combustion and increasing the life span of engines.

Keywords: XU7 Engine; Biochar;Copper catalyst;NOx;Exhaust emissions;

1. Introduction

The combustion time, in internal combustion engines, is limited by the engine's cycle to less than a second. Due to incomplete combustion of the fuel, the partial oxidation leads to emission of carbon monoxide (CO), nitrogen oxides (NOx) and a big range of volatile organic compounds (VOC), comprising hydrocarbons (HC), aromatics and oxygenated compounds. These emissions are particularly high during both stand-stills and velocity reduction, when inefficient air is taken in.

In order to decrease the harmful environmental effects of these emissions, catalytic converters are used within the car exhausts. The ordinary catalytic converters are composed of a metal guard with a ceramic honeycomb-like inside of it with protecting layers. This inner honeycomb has thin wall channels that are covered by aluminum oxide. This cover is porous and increases the surface area, letting more reactions to occur and comprising valuable metals, such as palladium, rhodium, and platinum. The amount of these metals are about 4-9 grams in a single converter. As the initial price of these metals is high and due to the expensive production of porous materials, always there has been the need to cheaper and simpler ones.

Biochar which is a residual by-product from pyrolysis of organic waste biomass, is rich in carbon, up to 50 wt%, and typically accounts for 15–40 wt% of the biomass feedstock[1]. Generally, biochar is similar to graphite that is mostly composed of the aromatic carbon rings linked together and arranged randomly and irregularly [2]. Consequently, biochar, which is an abundant and low-cost renewable carbon source, has pronounced potential to be applied as a cheap and promising catalyst. Additionally, biochar can be easily detached from catalysts by oxidation to recover the valuable metals[3].

Due to its cheap price and the easy preparation, biochar has got more attention in recent years[2-5]. Yan et al.[6]applied biochar in the synthesis of carbon-coated iron nano particles, so the catalytic activity on the conversion of synthesis gas to liquid hydrocarbons was evaluated. It was identified that a well-developed porous structure, which probably benefit the uniform dispersion of active components and stabilize these against sintering, are essential for a good catalyst support[6]. Some features of biochar assist its role as a catalytic material. For example, the incidence of inorganic, such as K and Fe in biochar

* Corresponding author e-mail: r.yeganeh@ilam.ac.ir.

contributes to its catalytic activity for tar cracking[7]. The functional groups of the surface in biochar could simplify the adsorption of metals, which is a necessary step for the production of biochar-supported catalysts [8]. Generally, the material is cheap and available everywhere, the methods of producing it is also applicable so the cost of making it is low and economic and it is possible to replace it with the conventional catalysts nowadays.

The Biochar-based catalyst is a new and promising method to be used as it is proved that this mesoporous material is a helpful one to absorb a large variety of gases and contaminants from different media, such as water, soil and air. Therefore, it is really suitable to trap and degrade the gaseous contaminants. In order to decrease the synthesis price of the catalytic converter, copper was chosen as a catalyzer to help the conversion processes within the converter. Therefore, the present work aimed at studying the catalytic application of biochar in using as catalytic material instead of honeycomb structure of the normal catalytic converters. The objective of this study is to propose a new catalytic converter for filtering the exhaust emissions with a reasonable price.

2. Materials and methods

2.1. Copper-based biochar preparation

The biochar was produced by the pyrolysis of dried chicken manure. The pyrolysis temperature was set to 400 °C. This temperature was obtained after about 30 min of heating with the carrier gas (N_2) sweeping at 0.3 L·min^{-1}, and the porcelain crucibles were fed into the heating zone with an N_2 flow rate of 0.03 L·min^{-1}. After 2 h, the pyrolysis process was stopped. The solid yield was the biochar, sieved through a 40 mesh (0.45 mm). Copper was used to be replaced with the expensive elements such as palladium, as an oxidating agent. The results did not show a clear difference between its usage and the control one. This could be due to lower amount of it or the oxidating function was not as well as palladium or rubidium. That is why the results were not significantly sharp.

2.2. Copper stabilization on the biochar

The initial mixture including 5 g of biochar and 2.482g (2 mmol) silver nitrate was prepared in a 250 ml flask. Then, 150 ml of deionized water was added to the mixture. A magnetic stirrer was used for stirring the resulting mixture at 75 °C for 24 h. The resulting product was filtered through a filter paper and washed several times with water and placed in an oven at 80 °C for 24 hours to get dried completely. The resulting precipitate was placed in the furnace for calcination at 550 °C for 5 hours[9]. This process has been summarized in Fig. 1. In order to make uniform samples, circular tablets were prepared from the material. The pressure of 10 bar was applied to ensure a proper texture of the tablets.

2.3. Engine condition and preparation

In this study, the XU7 engine, which was produced in 2011, was used to perform the tests. The data were taken from the vehicle in the on and off mode at idle speed (860 rpm).Before performing the tests, the engine was switched on for 15 minutes to reach the optimum temperature of the engine. The temperature of the radiator water in the engine was about 85±4˚C. This is due to different function of the engine in cold condition. In this case, after the engine reached the mentioned temperature the data collection was done by placing the prop of the device into the engine, for data collection. Temperature was about 27±3˚C.Exhaust emission parameters (O_2, CO, NO_X, CO_2, HC) were measured using AGS-688 (Italy). For this reason, the initial part of the sensor (suction) of the device was placed in the designed exhaust for the car.

2.4. Catalyst mold

A molded rectangular cube was made using galvanized sheet (thickness of 1.5 mm)in two different internal lengths of 7 and 14 cm (Fig. 2).

Figure 2. Designed catalyst mold

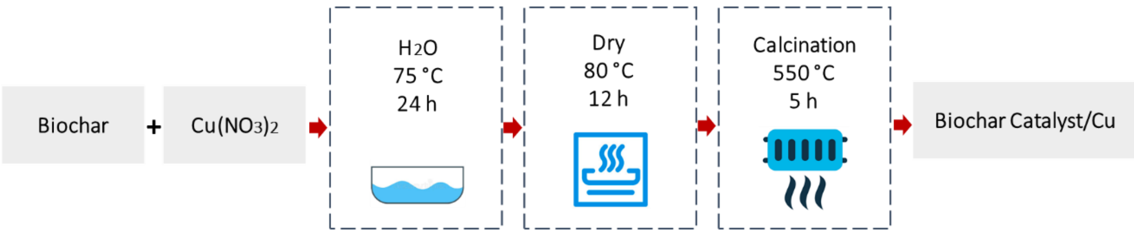

Figure 1. The preparation process of the catalyst.

2.5. Catalyst Implementation

The catalyst mold was designed and fabricated to replace the test specimens in two separate parts (door and mold case). For the catalyst die-casting, a refractory blanket was used. The test tablets were divided into four equal components and were placed in the mold (Fig.3).

2.6. The XU7 Test Engine

In this research, a XU7 engine made in 2011 was used for the experiments. Vehicle data were taken in clear mode at idle speed of 860 rpm. Before the tests, the engine was powered on for 15 minutes until the engine temperature reached its optimum point. The temperature of the radiator water in the engine was about 85±4 °C to perform in the pollutant conditions. For data acquisition, after the engine reached the specified temperature, a data device prop was used. The air temperature was about 27±3°C. Exhaust parameters (O2, CO, CO2,NOx, HC) were measured using AGS-688 device made in Italy. For the measurements, the inlet part of the exhaust sensor was inserted into a vehicle exhaust system.

2.7. Spectroscopy measurements

To investigate the percentage of copper fixed on the surface of biochar nanocavity, EDX spectroscopy (FESEM TESCAN, MIRA III, Czech Republic) of the catalyst was taken. Also, using ICP-AES the amount of copper metal in the biochar-stabilized copper composition was determined.

2.8. Data analysis

Analysis of variance was performed using completely randomized design and mean comparisons of treatments were performed using Duncan's multiple range test. The statistical analysis was done using SAS 9.1 software.

3. Results and Discussion

3.1. EDX Spectroscopy

Based on EDX spectroscopy, it was detected that there existed C, N, O and Cu elements in the catalyst. The percentage of elemental mass for 1 mmol of these elements was6.23%, 4.48%, 49.99% and 39.29% and for 2 mmol, it was 11.41%, 2.01%, 25.08% and 61.5%, respectively.

Each of the peaks shown in Figs 4 and 5 is unique for an atom and therefore represents only one element. Peaks higher in the spectrum mean higher concentrations of the element in the sample. The results of ICP-AES test showed that the amount of copper metal in the biochar-stabilized copper composition for 1 and 2mmol was 0.043 and 0.079 mmol/g, respectively.

a b c d

Figure 3. Preparation of the catalyst mold.

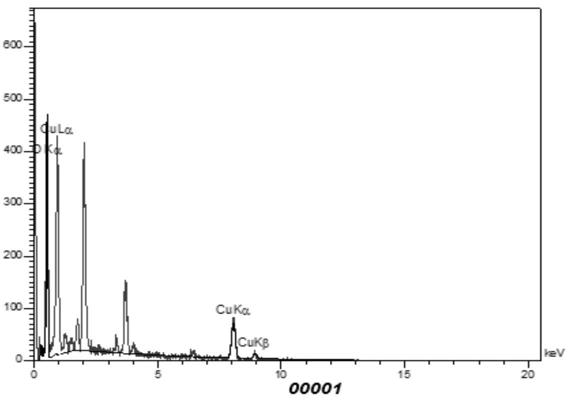

Figure 4. EDX diagram of the fixed Cu (1 mmol) on biochar.

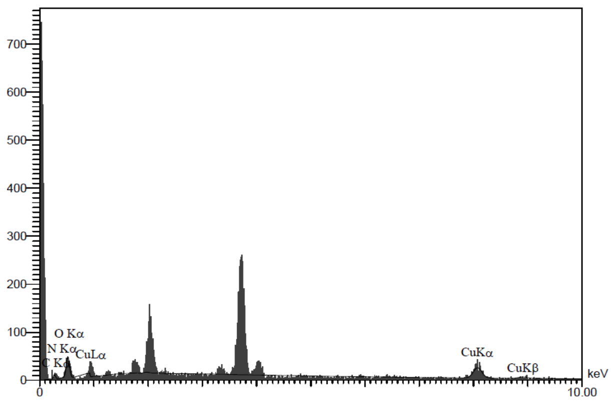

Figure 5. EDX diagram of the fixed Cu (2mmol) on biochar.

3.2. Analysis of variance

The results of the analysis for variables evaluated in XU7 engine are shown in table 1. As it is seen from the table, there were significant differences between different treatments regarding the extent of Co, HC, CO_2, and O_2, in the probability level of 1%. For λ (i.e. air to fuel ratio) there was a significant difference between catalytic treatments in the probability level of 5%. However, for the presence of NOx the difference was not significant.

3.2.1. Carbon monoxide

A comparison of the average volumetric CO concentration of the exhaust emitted by the XU7 engine with respect to the types of catalysts is given in Fig.6. As it can be observed, the average amount of CO emissions was lower than the standard limit(i.e. less than 2.5%). It is also notable that carbon monoxide is produced when the combustion is rich in fuel and air but the oxygen is insufficient. The results of the experimental treatments were significantly reduced for CO emissions of all treatments (in the probability level of 1%). The results showed that there was a significant difference between the proposed and non-catalyst treatments. However, there was no significant difference between experimental treatments.

3.2.2. HC

A comparison of the average concentration of unburned HC hydrocarbons in the exhaust of the XU7 engine with respect to the types of catalysts, biochar, proposed catalysts and no catalyst is shown in Fig. 7. As the figure shows, in the XU7 engine the average HC pollutant was below the standard limit (i.e. less than 250 ppm). This might be due to lack of several factors involved in the production of hydrocarbons, of which the most important are the non-stoichiometric fuel ratio, incomplete combustion, leakage and leakage volumes, leakage through outlet valve, simultaneous open valves, sediment, and oil on the combustion chamber wall. The results indicated that the effect of HC on engine exhaust gas level was significant and a significant difference between various treatments was observed (p>0.01).

According to the researches, HC and CO in vehicle exhaust oxidize and produce water and carbon dioxide. Catalytic engineering applied to automobiles is actually able to reduce CO and HC emissions up to ninety percentage [10] and particulate matter about fifty percentages is dipped down [11].

Table 1. The results of ANOVA test.

Sources of variation	Degree of freedom	Mean Squares					
		Co(%vol)	HC (ppm)	NOx (ppm)	CO_2(%vol)	O_2(%vol)	λ
Treatments	7	0.181**	5864.17**	0.0219ns	0.849**	0.259**	0.000131*
Errors	16	0.0014	159.417	0.389	0.0275	0.0155	0.0000375
CV (%)	-	5.865	11.539	4.118	1.2	10.209	0.592

**significance level p>0.01, *significance level p>0.05, ns not significant

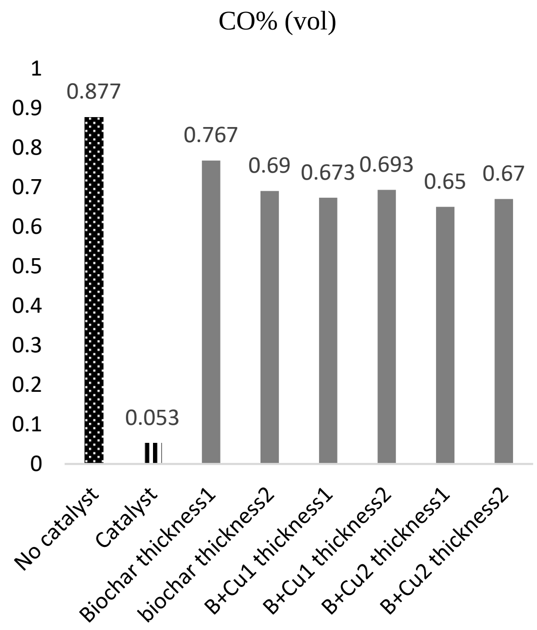

Figure 6. The amount of Co emissions in XU7 engine.

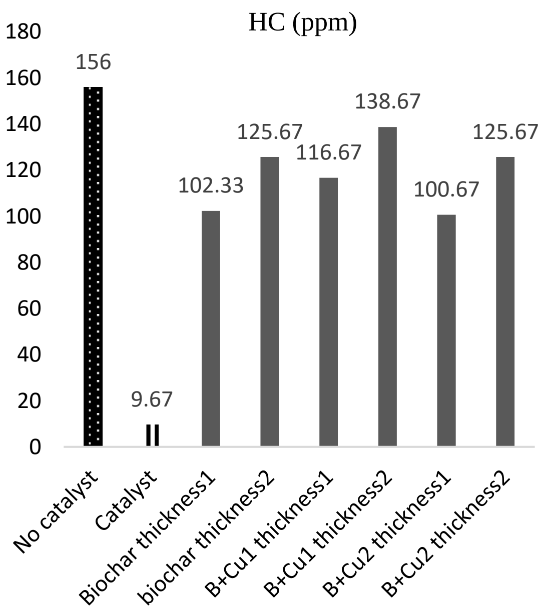

Figure 7. The amount of HC for XU7 engine.

Unburned hydrocarbons produced at the gasoline burning stage are converted to carbon dioxide and water vapor according to the oxidation process of Equation (1) [12]:

$$C_xH_{2x+2} + [(3x+1)/2]\ O_2 \rightarrow xCO_2 + (x+1)\ H_2O \qquad (1)$$

The results indicated that the removal rate by the proposed catalyst was 0.1626 g per catalyst, and the adsorption by the metal catalyst fixed on biochar was 1.2296 g per catalyst. The results showed that reduction of HC for the thickness of 2 mm and density of 1 mmol had a significant difference with thickness of 2 mm and density of 2 mmol, thickness of 2 mm and density of 1 mmol.

3.2.3. CO_2

The results for the percentage of CO2 emissions for all treatments have been presented in Fig. 8. It was observed that carbon dioxide produced in the XU7 was below the standard limit (more than 14%) with the exception of the catalyst-free case. This is a remarkable achievement for the proposed catalyst as the excessive carbon dioxide emissions worsens the global warming crisis.

In addition, the above results showed that in case of the proposed catalyst, the value of 0.0019 g per catalyst, gas increase was obtained, while the increased value of gas by the copper catalyst stabilized on biochar was achieved as 0.0041 g per g catalyst [13].

3.2.4. NOx

The results showed that the NOx produced in the XU7 was below the standard limit (i.e. < 50 ppm)(Fig. 9). The results showed that the effect of NOx on the gas output from the engine was not significant. For the proposed catalyst, the amount of gas absorption was 0.0003 g per catalyst. For the designed catalyst of copper fixed on biochar, the amount of gas absorption was 0.0018 g per catalyst. The results showed that there is no profound difference between the proposed catalyst and the other treatments.

3.2.5. O_2

Fig. 10 provides the results for the comparison of presence of O2in the XU7 engine exhaust. The results showed that the amount of oxygen produced in the XU7 engine was below the standard limit (i.e. < 3%). The results showed that the effect of O2 on engine exhaust level was significant (p>0.01).

According to the proposed catalyst, the amount of O2 increased by 0.001 g per catalyst. However, the amount of gas released compared to the designed sample is 0.0028 g per catalyst. This is because of the decomposition of the water vapor produced in the gasoline combustion stage and due to the involvement of O2 in the CO2 and HC oxidation reaction of O2.Installing the catalyst on the motor prevents the gas from releasing, which causes the exhaust gases to condense behind the catalyst to the smoke valve. This causes choking and impedes airflow into the engine.

The results showed that there was a significant difference between the proposed catalyst with other treatments. The highest mean value was obtained for catalyst-free combustion, indicating the highest amount of O2 emission. In the proposed catalyst, the O2was absorbed to a greater extent, indicating that the gas was involved in the catalytic reaction.

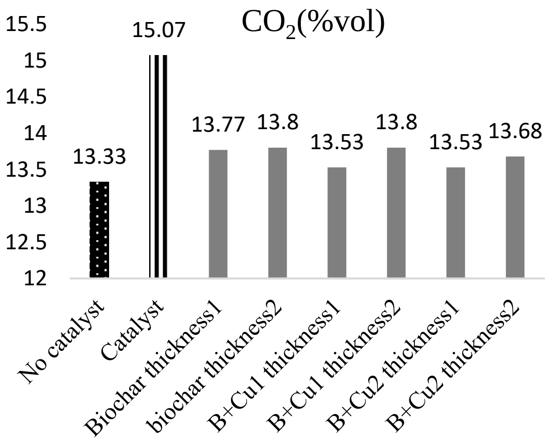

Figure 8. The amount of CO2 gas for XU7 engine

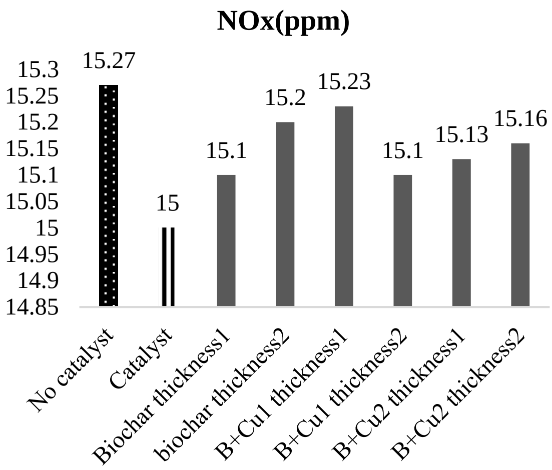

Figure 9. The amount of NOx gas for XU7 engine

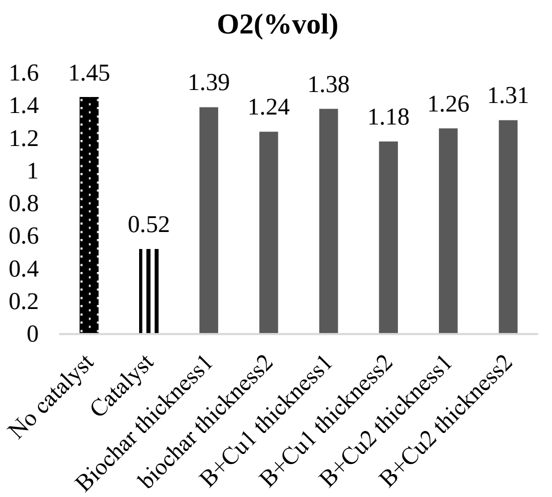

Figure 10. The amount of O2 in XU7 engine exhaust.

3.2.6. Coefficient of λ

The results showed that the coefficient of λ in the XU7 engine was below the standard limit (i.e. < 3%)(Fig.11).The ratio of coefficient of λ increased with respect to the proposed catalyst sample. However, due to the catalyst-free state of approximately 0.0002 g/L, the reduction of λ was carried out using a catalyst-based converter based on the activated carbon (present in biochar substrate). This is because of the decomposition of the water vapor produced in the gasoline burning stage as well as the involvement of O_2 in the CO_2 and HC oxidation reaction of O_2. The less the O_2, the less the coefficient of λ of the inlet airflow to the engine.

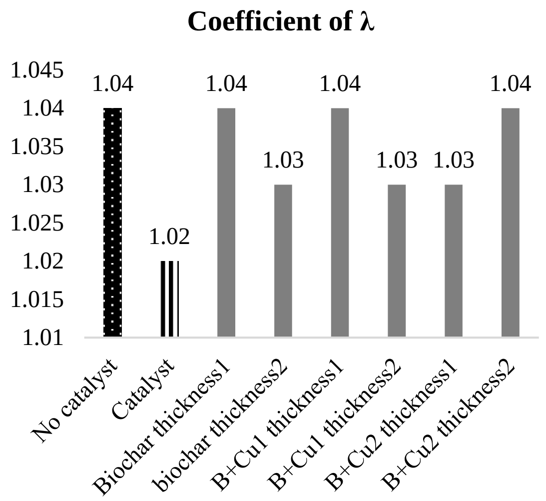

Figure 1. Coefficient of λ in XU7 engine**.**

4. **Conclusion**

The study presented a promising and cheap catalyst for the reduction of engine emissions. A copper catalyst supported on biochar was used as a catalytic converter in XU7 engine. The results showed that the proposed catalyst lowered all the measured contaminants (i.e. CO, CO_2, HC, O2 and NOx) to below the standard level. The proposed catalyst increased the ratio of air to fuel (λ) significantly in comparison to other treatments. According to the results, it is suggested that the usage of the proposed catalyst can be an effective step in reducing greenhouse gas emissions combustion and increasing the life span of engines.

References

[1] Brown, T. R., Wright M. R., & Robert C. B. "Estimating profitability of two biochar production scenarios: slow pyrolysis vs fast pyrolysis." Biofuels, Bioproducts & Biorefining,Vol 5, no. 1, 2011, 54-68.

[2] Yu, J. T., Dehkhoda A. M., & Ellis N. "Development of biochar-based catalyst for transesterification of canola oil." Energy & fuels,Vol 25, no. 1, 2011, 337-344.

[3] Xiong, H., Motchelaho M. A. M., Moyo M., Jewell L. L., & Coville N. J. "Correlating the preparation and performance of cobalt catalysts supported on carbon nanotubes and carbon spheres in the Fischer–Tropsch synthesis." Journal of Catalysis,Vol 278, no. 1, 2011, 26-40.

[4] Xiong, X., IrisK. M., Cao L., Tsang D. C. W., Zhang Sch., & Sikok Y. "A review of biochar-based catalysts for chemical synthesis, biofuel production, and pollution control." Bioresource technology,Vol 246, 2017, 254-270.

[5] Lee, J., Kim K., & Kwon E. E. "Biochar as a catalyst." Renewable & Sustainable Energy Reviews,Vol 77, 2017, 70-79.

[6] Yan, Q., Wan C., Liu J., Gao J., Yu F., Zhang J., & Cai Z. "Iron nanoparticles in situ encapsulated in biochar-based carbon as an effective catalyst for the conversion of biomass-derived syngas to liquid hydrocarbons." Green chemistry,Vol 15, no. 6,2013, 1631-1640.

[7] Hervy, M., Berhanu S., Weiss-Hortala E., Chesnaud A., Gerente C., Villot A., Minh D. P., Thorel A., Le Coq L., & Nzihou A. "Multi-scale characterisation of chars mineral species for tar cracking." Fuel,Vol 189, 2017, 88-97.

[8] Cao, X., Sun Sh., & Sun R. "Application of biochar-based catalysts in biomass upgrading: a review." RSC advances,Vol 7, no. 77, 2017, 48793-48805.

[9] Hajjami, M., Ghorbani F., & Yousofvand Z. "Copper (I) complex of 1, 3-DimethylBarbituric acid modified SBA-15 and its catalytic role for the synthesis of 2, 3-Dihydroquinazolin-4 (1H)-ones and Imidazoles." Applied Organometallic Chemistry,Vol 31, no. 12, 2017,e3843.

[10] V. Burns, J. Benson, A. Hochhauser, W. Koehi, et al., Description of auto/oil airquality improvement research program, SAE Trans. 1991, 912320.

[11] F. Terres, H. Weltens, D. Froese, Electrically heated catalyst – design andoperation requirements, SAE Trans. 1996, 961137.

[12] Venkatesan, S. P., Uday D. S., Hemant B. K., Kushwanth Goud K. R., Kumar G. L., & Kumar K. P. "IC Engine emission reduction by copper oxide catalytic converter." In IOP Conf. Ser. Mater. Sci. Eng, Vol. 197, no. 1, p. 012026. 2017.

[13] Vilčeková, Z., M. K., Domanicka M., HnatkoM., & ŠajgalíkP. "Influence of the preparation of si3n4 based foams on the compressive strengthand processing flaws." Powder Metallurgy Progress, Vol 13, no. 3-4, 2013, 139.

JJMIE

Volume 15, Number 2, June. 2021
ISSN 1995-6665
Pages 215 - 231

Jordan Journal of Mechanical and Industrial Engineering

Comprehensive Energy-Econo-Enviro (3E) Analysis of Grid-Connected Household Scale Wind Turbines in Qatar

Ehsan Abbasi Teshnizi[a], Mehdi Jahangiri[a], Akbar Alidadi Shamsabadi[b], Luis Martin Pomares[c], Ali Mostafaeipour[d], Mamdouh El Haj Assad[e*]

[a]Department of Mechanical Engineering, Shahrekord Branch, Islamic Azad University, Shahrekord, Iran.

[b]Young Researchers and Elite Club, Shahrekord Branch, Islamic Azad University, Shahrekord, Iran.

[c]Solar Technology Advisors, Calle Segre nº 27, 1ºA, 28002 – Madrid, Spain.

[d]Industrial Engineering Department, Yazd University, Yazd, Iran.

[e]Sustainable and Renewable Energy Department, University of Sharjah, Sharjah, UAE.

Received May 4 2020 Accepted May 24 2021

Abstract

Among various types of renewables, wind energy requires a less initial investment that is projected to decrease even more due to technology advancement, a higher number of turbines, and ease of restrictions. Unlike traditional power-plants, wind turbines have been developed in various dimensions, and minimal land is taken out of production, so they are recommended for small countries facing a lack of space. Given these facts, a potentio metric study of supplying the electricity of a residential house in 5 cities of Abu Samrah, Ar-Ruways, Doha, Duhan, and Musayid, Qatar, is performed using HOMER and meteorological 20-year-average data taken from the NASA website. The studied system is connected to the grid, and a techno-Econo-environmental study is conducted. The study results of the turbulence intensity (TI) parameter indicated the mechanical components of the wind turbine in the Doha station were under intermediate fatigue loads while these loads were lower in the remaining stations. According to the results, it is clear that Doha station, with a price per kWh of electricity generated, and a total net present cost (NPC) of $0.086 and $6349, respectively, produces the most cost-effective wind power electricity due to using BWC XL.1 horizontal axis wind turbine. The highest amount of CO2 emissions savings and most top production of CO2 are associated with Doha (-300 kg) and Abu Samrah (2844 kg) due to using EOLO and Turby wind turbines, respectively. Ar-Ruways generate the highest (8890 kWh/y) and lowest (658 kWh/y) amounts of wind power electricity and Abu Samrah stations which are due to utilizing Generic 10 kW and Turby wind turbines, respectively.

Keywords: Power curve; Hub height; Wind speed; National electricity grid; Weibull function.;

1. Introduction

For the first time in history, in 2015, the urban population has surpassed the rural one and future trends also reveal that, by 2020, around 70% of the world population will be living in cities. Among all continents, Asia and Africa will be more influenced by urbanization and, by 2050, their urban population will increase from 40% and 48% to 56% and 64%, respectively [1]. A dilemma involving this issue is the constantly increasing emission of carbon due to this rapid growth of world population and urbanization [2, 3].

Qatar also is experiencing rapid economic growth which is accompanied by a rapid escalation in population and urbanization and, therefore, higher demand for energy sources like fossil fuels, electricity, and water has resulted in an increased air and environmental pollution [4]. According to the IPCC (Intergovernmental Panel on Climate Change) reports, by producing 45 tons of CO_2 per capita per year, Qatar is ranked as the highest per capita carbon emitter globally [5, 6]. Air pollution is very alarming in Qatar because it often exceeds the local and international recommended standards [7]. According to WHO (World Health Organization), Duha is one of the most polluted cities in the world which ranks 12 in terms of air poor quality (annual average particulate matter formation) [8]. Although some international, national, and governmental policies are needed to solve these problems, people and regions can also be useful in reducing these issues [9]. For example, Qatar has large fossil fuel energy resources [10], but the country has also adopted a sustainability-oriented strategic solution for reducing energy consumption while producing more reliance on clean and renewable energy sources and that is raising public awareness about environmental damages due to overconsumption of energy [11] and the necessity of preserving fossil fuel as an inheritance for future generations, providing job security in

* Corresponding author e-mail: massad@sharjah.ac.ae.

this field and improving the lifestyle [12]. This roadmap will definitely enable Qatari citizens to give priority to saving energy and protecting the environment [13].

For human development to continue, renewable, i.e., infinite, energy sources have to be found. Due to its abundant benefits, wind energy application has grown rapidly [14, 15]. The most important advantage of wind turbines is that they are less environmentally harmful [16-18]. Wind turbines directly produce no air or environmental pollution [19,20]. This secures people residing around wind farms from serious health problems. Given the fact that wind is a renewable energy source and it is not dependent upon shipping or underground reverses, it also helps prevent indirect transportation-induced pollution. Furthermore, unlike the majority of methods, wind energy is capable of producing electricity without water. Thus, it prevents water pollution and shortages of energy caused by droughts [21].

In windy areas, wind turbines can produce electricity during all hours day and night. This is particularly true for coastal and mountainous regions. They can be installed at various places for residential or commercial applications. Wind equipment can be mounted in houses, farms, offshore platforms, and on top of high hills. This form of renewable energy is highly scalable. While traditional power-plants are built to provide electricity for huge populations, turbines are developed in various sizes. The energy produced by different models of wind turbines can supply the required power of a small farm, a house, or hundreds of houses [22,23].

Another advantage of wind turbines is that they occupy far less area than conventional power-plants or even solar farms and people can continue other activities around the wind farms. This is of high importance for small countries facing space problems — businesses, farmers, and landowners that install wind turbines on their lands and enjoy a significant saving and can keep their lands economically viable without using a considerable area of land. Wind turbines also cut the utility costs of residential houses. Wind energy is available in almost all parts of the earth, but there are discrepancies regarding wind compatibility and power. It is estimated that 1 million GW of wind energy is available all over the world and if the potential wind energy is extracted from 1% of these amounts, it could supply all the electricity demand of the world [24].

Belke and Palm (2009) studied the wind energy potential by collecting data at four various places in Ethiopia, i.e., Addis Ababa, Mekele, Nazret, and Debrezeit, and analyzing them using HOMER [25]. They determined monthly average wind energy potential, the probability density function of wind speed (PDF), wind cumulative density function (CDF) and wind duration curve (DC) for all four areas. According to the measurements at 10 m altitude, results indicated a reasonable wind energy potential with an average wind speed of 4 m/s for the studied sites, except for Debrezeit.

Rodrigues and Rossi (2016) compared to power generation of two small wind turbines (a 6 kW and a 5 kW) using HOMER [26]. They investigated the wind sources of three various cities: Campinas and Cubatãoin Brazil and Roscoe in Texas, US. A grid-connected and an off-grid system (using batteries) were evaluated. Results showed that for the 5 kW and 6 kW turbines, the cost of electricity (COE) of the off-grid system were up to 9.95 and 19.8 times higher than that of the grid-connected system, respectively.

Ayodele and Ogunjuyigbe(2016) studied the wind energy potential at Vesleskarvet, the Antarctic, to meet the energy demands of the South African SANAE IV Research Station located at Vesleskarvet [27]. Optimization results using HOMER showed that 15 wind turbines (PGE20/25 model) with the following specifications seemed capable of meeting the energy demands of SANAE IV research base: 25 kW rated power, 3.5 m/s cut-in wind speed, 25 m Hub height, 9 m/s rated wind speed and 25 m/s cut-out speed. These entailed $1,336,262 total NPC, operational cost of $976,500, and $0,102 COE.

Qolipouret al., (2016) used HOMER for a techno-economic evaluation of manufacturing small residential-scale wind turbines in six districts of Ardebil Province, Iran, given the wind speed data in the period of 2008 to 2014 [28]. Using an integrated ranking method and considering the power generation capacity of turbines, their manufacturing costs, profits, the sum of net and depreciation costs, and emissions per plant were calculated separately for each district. Results indicated that Ardebil, BilaSavar, Kowsar, Firozabad, Nir, Namin, and Airport sites ranked as sixth to first.

Becerra et al., (2017) studied the financial feasibility of installing wind farms in small-scale for Chile by evaluating real-world scenarios in high potential areas to be used for the residential sector [29]. They used HOMER for their evaluations. The selected places were Laguna Verde in the central parts and Porvenirin the southern parts of Chile. Given the 90 kW rated capacity, a small-scale wind farm was studied. Results obtained after 240 simulations indicated that direct connection to the wind farm consisting of FD16-30 wind turbines, by producing the lowest total NPC, was among the most optimal scenarios chosen.

Qolipouret al., (2018) applied mathematical modeling for facilitating the simultaneous optimization of construction of new wind power-plants and renewable electricity prices at various areas of Kermanshah Province, Iran [30]. Their case study included the development of one, two, or three wind power-plants in three regions of Taze Abad, Samer, and Gilan-e-Qarb (in the order of their potential wind power). First, ten-year wind speed data (2006-2016) of these three areas were simulated for techno-economic feasibility evaluation of wind power-plants using HOMER. Then, the software outputs were used to solve the related mathematical model in MATLAB. Results showed that by constructing one, two, or three wind power-plants, the optimal price would be $0.159, $0.151, and $0.140 per kW of electricity generated.

Shaahidet al., (2018) conducted the economic feasibility of developing a 30 MW wind power-plant in Turaif, Saudi Arabia [31]. In this study, the choice of commercial wind equipment, energy simulations, and the size of wind farms were performed using HOMER. The annual energy produced by this 30 MW wind farm (hub height of 50 m) reached 39752 MWh. By developing this 30 MW wind farm around 1598 tons of CO_2 emissions could be saved annually.

Mendez and Bicer (2019) studied wind energy potential in Qatar and its environmental and financial effects on the natural gas industry [32]. They selected a commercial wind turbine according to the wind speed and direction data.

Results indicated that, with an average wind speed of 5.06 m/s, a 17 MW wind power plant annually reduces 6.8 tons of CO_2 emissions as well as having an annual economic impact of $3.32 million on Qatar's economy.

Given the facts mentioned above and since no research has been conducted so far on vertical and horizontal axis wind turbines in Qatar to find the lowest cost of wind-powered electricity, this study is the first one to use 20-year average data taken from the NASA website and HOMER software for techno-Econo-environmentalresearch in this regard. The studied system was connected to the national grid, and such parameters as COE, total NPC, and the emissions produced were investigated. Eventually, the most suitable wind turbine among eight commercially available wind turbines (4 horizontal axis and four vertical axis) were identified for each station. Since the results of the present work can be used as a guide to help decision-makers and policymakers in the field of energy in Qatar, the authors of the present study have tried to accurately study the wind potential in different stations, determine various costs of wind power, and perform environmental analyses.

The HOMER software performs the most accurate technical, economic, and environmental calculations for renewable energies, and the reason for choosing it is its simplicity of use and one-year analysis. The present work used HOMER software whose database only contains the information on horizontal-axis wind turbines (HAWTs). The authors have been able to upgrade the software's features by inputting experimental data on the power curve of vertical-axis wind turbine (VAWTs) in a .txt file format which is the first attempt in this respect.

Furthermore, using realistic and updated data for the price of grid electricity, equipment, annual interest rate, etc. makes the results beneficial for policymakers in the energy sector to make sound decisions about wind-powered electricity in Qatar.

2. The Studied Area

Qatar is a country located in Southwestern Asia, occupying the small Qatar Peninsula on the northeastern coast of the Arabian Peninsula. Doha is its capital city, and its sole land border is with neighboring Saudi Arabia to the south, with the rest of its territory surrounded by Persian Gulf boundaries with Iran, Kuwait, Iraq, Saudi Arabia, Bahrain, and United Arab Emirates. The country covers an area of 11493 m^2 [33]. In 2018, Qatar's total population was 2.7 million [34]. Figure 1 shows Qatar's geographical location in the world.

Slightly tropical weather dominates throughout the year. Summer is the hottest time of the year that lasts very long from May to September with highs up to 50˚ C. Winter season (from November to May) is also rather mild with temperatures between 21˚ to 27˚ C [35]. Due to the growth in population and urbanization, Qatar is facing increasing energy demands [36]. Therefore, the first important step is to design and implement initiatives for reducing energy use by households [37].

Qatar is the second-largest consumer of electricity among the Gulf Cooperation Council (GCC) countries [38]. Qatar Electricity & Water Company (QEWC) has announced that in the last decade, Qatar has enjoyed rapid economic and infrastructural developments and this has led to a 6% to 7% increase in annual electricity demand [39]. In 2014, annual energy consumption in this country reached 17 million MW per capita [40]. Under the Kyoto Protocol and through ratification of the COP21 agreement by April 22, 2016, Qatar has shown its tendency to follow a GHGs reducing strategy [41]. Besides, preserving the environment for future generations, there is another critical goal which Qatar seeks for in the coming years [42]. Nowadays, Qatar's economy is considerably dependent upon oil and gas industry. Because of the precarious prices of the oil and hydrocarbons, however, a sustainable and clean energy-producing alternative seems necessary [43]. Qatar has estimated to generate 1800 MW of its required power by renewables by 2030 [44]. Qatar, along with other GCC countries, by an annual wind potential of more than 1400 hours, has the potential capacity for using wind energy [45]. Figure 2 shows the renewable energy deployment target of GCC countries by 2020 among which Kuwait and Qatar hit the highest potential by 10 and 6 percent, respectively [16]. Figure 3 depicts the wind potential at various areas of this country at 50 m height [46].

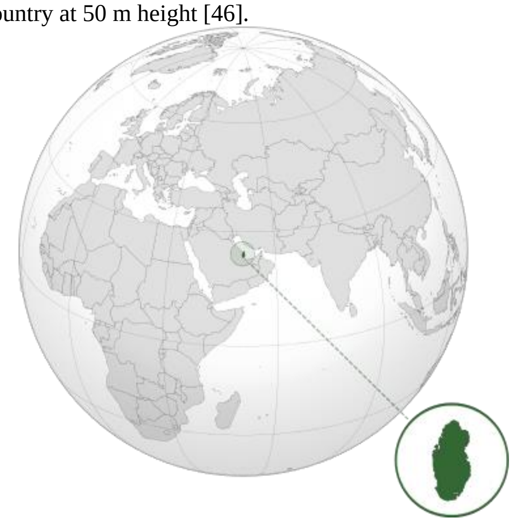

Figure 1. The location of Qatar in the world.

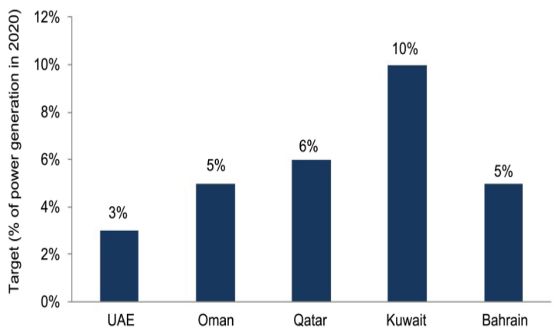

Figure 2. Target of Renewable energy in Gulf Cooperation Council countries by the year 2020.

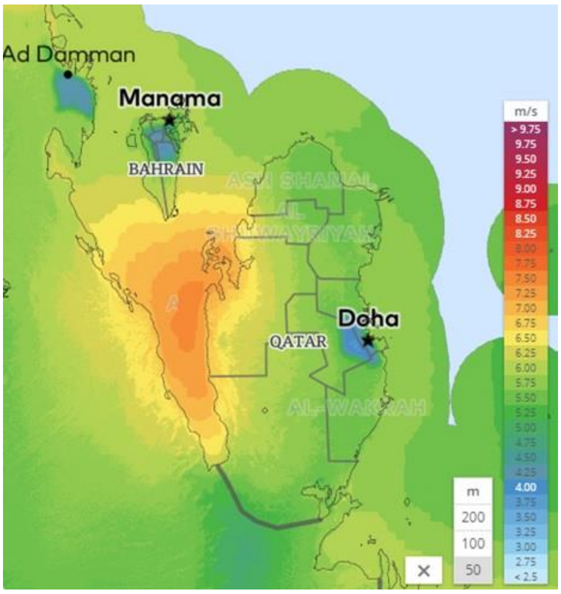

Figure 3. Wind atlas of Qatar in the height of 50m [46].

3. Methodology

HOMER was used to design and evaluate an optimal micropower in both off-grid and grid-connected states to achieve the applied program's purposes. When planning a power generation system, many decisions have to be made about the due configuration of the system: what components such as panel, wind turbine, diesel generator, etc., are required to build a power system? What is the appropriate number and size of each component?

Various technologies used, changes in the costs of these technologies and the availability of energy sources render it more difficult to make reasonable decisions. Optimization algorithms and sensitivity analysis of HOMER facilitate the evaluation of many feasible systems. HOMER outputs the simulation results in the form of tables and diagrams which makes it easy to compare various configurations. Then it compares them according to their economic and technical rankings and provides for the derivation of charts and graphs in reports and presentations. When one wants to assess the effect of changing such factors as access to resources and economic conditions on efficiency and cost-effectiveness of various systems configuration, HOMER's sensitivity analysis might be helpful. Results of this analysis can be used for the determination and identification of the factors most influential on the system design and operation. Also, HOMER's sensitivity analysis results might be useful for solving general equations of technology alternatives utilized for planning and decision-making. HOMER software simulates the operation of a system by doing the calculations of energy balance in 8769 hours of the year. For each time step, HOMER compares the thermal and electrical demand in that time step to the energy that the system can supply in that time step, and calculate the flows of energy to and from each part of the system. For systems that include fuel-powered generators or batteries, HOMER also decides in each time step how to operate the generators and whether to discharge or charge the batteries. Energy balance calculations are performed by HOMER for each system configuration, which can then determines whether an arrangement is feasible, i.e., or whether it can meet the electric demand under the situations that you specify, which can also estimate the installing and operating cost of the system over the project lifetime. The system cost calculations account for expenses, such as capital, operation and maintenance, replacement, interest and fuel [47].

The validation of data in the present work has been conducted using wind speed data from Lutak station in Teimourian et al. (2019) [48] work and the Weibull function calculated by them has been compared with that calculated by HOMER. Data used in the study by Teimourian et al. are obtained by an analytical method and from curve-fitting on the wind power data where C=7.22 and K=1.6. However, in the present work, using the HOMER software, C and K obtained from curve-fitting are 7.36 and 1.97, respectively. The reason for choosing the Weibull distribution function for validation is the fact that its uses for measuring potential and fitting the actual probability of wind occurrence. As the comparison in Figure 4 shows, there is a good agreement between the HOMER-plotted Weibull function and that obtained by Teimourian et al.

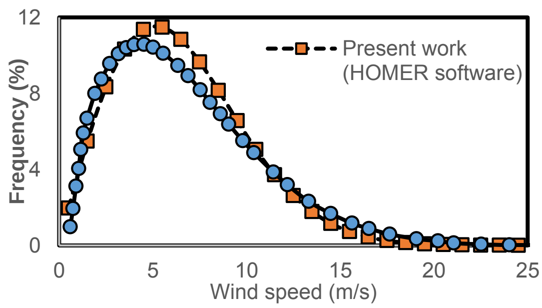

Figure 4. Validation of HOMER results against results of other works using Weibull function

The components used in the present work are explained below [49].

3.1. Wind Turbine

Based on the power curve and hub-height wind speed, HOMER calculates the wind turbines' power output. It should be noted that the power curves typically specify wind turbine performance under conditions of standard temperature and pressure. HOMER multiplies the air density ratio by the power value predicted by the power curve to regulate actual conditions, according to the following equation:

$$P_{WTG} = \frac{\rho}{\rho_0} \times P_{WTG,STP} \quad (1)$$

Where ρ is the actual air density (kg/m^3), ρ_0 is the air density at standard pressure and temperature equal to 1.225, $P_{WTG,STP}$is the power output of wind turbine at standard pressure and temperature.

The HOMER database contains only technical information and data about the power of horizontal axis wind turbines. In the present work, the experimental diagrams of power and technical specifications of four vertical axis wind turbines (WRE, Turby, Spiral, and WOLO) are converted into .txt files and added to HOMER software as inputs.

3.2. Converter

An inverter's efficiency is the efficiency with which it converts DC electricity to AC electricity (in %). The inverter can operate at the same time as one or more AC generators. Inverters that are not able to perform this way are sometimes called switched inverters. The rectifier's efficiency is the efficiency with which it converts AC electricity to DC electricity (in %). It is noteworthy that HOMER assumes the rectifier and inverter efficiencies are constant. Most solid-state converters are less efficient at a very low load because of standing losses.

3.3. Battery

HOMER calculates in each time step the maximum value of power that can absorb by the storage bank. The maximum charge power changes from a one-timestep to the next is pursuant to its state of charge and its recent discharge and charge history. Three separate limitations impose by HOMER on the maximum charge power of storage banks.

The Kinetic storage model is the first limitation which is given by the following equation [50, 51]:

$$P_{batt,cmax,kbm} = \frac{kQ_1 e^{-k\Delta t} + Qkc(1-e^{-k\Delta t})}{1-e^{-k\Delta t}+c(k\Delta t-1+e^{-k\Delta t})} \quad (2)$$

where Q_1 is the available energy [kWh] in the storage bank at the beginning of the time step, Q is the total amount of energy [kWh] stored in the storage bank at any time, c is the storage bank capacity ratio [unitless], k is the storage bank rate constant [h^{-1}], $\Delta t$is the time step length [h].

The maximum charge rate of the storage component is the second limitation which is given by the following relation[50, 51]:

$$P_{batt,cmax,mcr} = \frac{(1-e^{-\alpha_c \Delta t})(Q_{max}-Q)}{\Delta t} \quad (3)$$

whereα_c is the storage's maximum charge rate [A/Ah], and $Q_{max}$is the total capacity of the storage bank [kWh].

The storage component's maximum charge current is the third limitation which is given by the following equation[50, 51]:

$$P_{batt,cmax,mcc} = \frac{N_{batt} I_{max} V_{nom}}{1000} \quad (4)$$

whereN_{batt} is the number of batteries in the storage bank, I_{max} is the storage maximum charge current [A], $V_{nom}$is the storage's nominal voltage [V].

HOMER sets the utmost storage charge power equal to the minimum of these three values according to the following equation[50, 51]:

$$P_{batt,cmax} = \frac{\text{Min}\,(P_{batt.cmax.kbm}\cdot\ P_{batt.cmax.mcr}\cdot\ P_{batt.cmax.mcc})}{\eta_{batt.c}} \quad (5)$$

where$\eta_{batt,c}$is the efficiency of storage charge.

3.4. Generator

By recording fuel curve inputs, HOMER plots the corresponding efficiency curve. The fuel curve shows the quantity of fuel that the generator consumes to produce electricity. The fuel curve is assumed as a straight line by HOMER. The following equation gives the fuel consumption of the generator in units/hr as a subordinate of its electrical output:

$$\dot{m}_{fuel} = F_0 Y_{gen} + F_1 P_{gen} \quad (6)$$

whereF_0 is the fuel curve intercept coefficient [units/hr.kW],F_1 is the fuel curve slope [units/hr.kW], $Y_{gen}$is the generator rated capacity [kW], $P_{gen}$is the generator electrical output [kW].

HOMER defines the electrical efficiency of the generator as the electrical energy coming out divided by the chemical energy of the fuel going in. The following equation gives this relationship:

$$\eta_{gen} = \frac{3.6\, P_{gen}}{\dot{m}_{fuel} LHV_{fuel}} \quad (7)$$

whereLHV_{fuel} is the lower heating value of the fuel [MJ/kg].

3.5. Cost Calculations

The real rate of discount is used to convert between annualized costs and one-time costs. HOMER uses the real interest rate to calculate annualized costs and discount factors from NPCs. HOMER calculates the annual real interest rate (i) from the nominal interest rate (i') by the following equation:

$$i = \frac{i' - f}{1 + f} \quad (8)$$

where*f* is the expected inflation rate, the inflation rate is assumed the same for all costs.

The total NPCis obtained by dividing the total annual cost by the capital recovery factor. The following equations used by HOMER to calculate the capital recovery factor:

$$CRF = \frac{i\,(1+i)^N}{(1+i)^N - 1} \quad (9)$$

Moreover, the cost per kWh of electricity generated is gained by dividing the total annual price by the price of the real electricity load generated.

4. Data Required for Simulation

HOMER requires wind speed data for simulating wind turbine systems. For the studied stations, these were 20-year-average data [52] taken from the NASA website which are presented in Table 1. It can be observed that the highest average wind speed (4.1 m/s) is associated with the Doha station.

Given the availability of the national electricity grid in the studied region, the studied hybrid renewable energy system (Figure5) is connected to the national electricity grid, and it is possible to sell/ buy electricity to/ from the national grid. An equal price of $0.022 per kWh is assumed for buying or selling power from/to the national grid [53]. Besides, given the fact that $CO_2$is regarded as the primary pollutant emitted, 632 g of CO_2 is considered per kWh of electricity produced by the national electricity grid. The buying/selling capacity of 1000 kW from/to the national grid is also assumed. The amount of electricity required for a residential house is 14 kWh/d on an annual-average basis (Figure5).

As can be observed in Figure 6, the peak load required is 2.12 kW which happens in June and the mean electricity needed is 0.579 kW. The daily random variability of 15% for the necessary power was also taken into account.

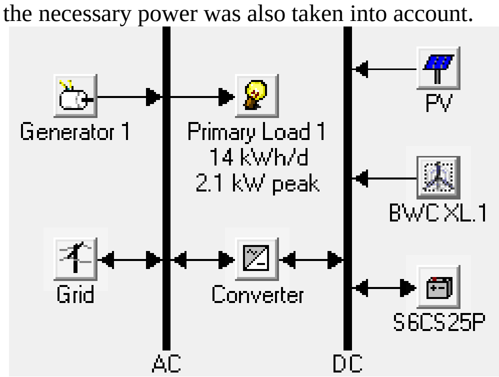

Figure 5. Schematic of the studied hybrid renewable energy system.

4.1. Wind Speed in the Studied Area

The wind speed will play an essential role in the designed system. Therefore, it is required to study the wind speed in the area of interest. To this end, wind data corresponding to the geographical location of the studied areas was taken from the NASA website. Figure 7 shows the daily-average wind speed for a year in the studied stations. From the results in Figure 7, it is evident that for Abu Samrah station, Ar-Ruways, Doha, Duhan, and Musayid stations the maximum and minimum daily-average wind speeds are respectively as follows: 4.4 m/s in June and 3.2 m/s in November, 4.6 m/s in June and 3.4 m/s in October, 4.9 m/s in June and 3.3 m/s in October, 4.4 m/s in June and 3.2 m/s in November, 4.3 m/s in June and 3.1 m/s in November.

Given the fact that the cut-in speed for many small wind turbines (power less than 10 kW [54]) is 3-3.5 m/s, we decided that small-scale wind-power generation is possible for all months of the year [55]. The wind energy potential for installing wind turbines is regarded as poor (<4 m/s), marginal (< 4-4.5 m/s), good to very good (5.5-6.7), and excellent (> 6.7 m/s) [56]. This is according to the wind speed available. In the stations studied in Qatar, it is clear that the wind speed can be categorized as good and very good or excellent for many hours of the day. According to Figure 7, wind speed is higher in hot seasons. Thus, in the summer month, when demand for electricity is the highest, the area can enjoy the maximum generation in case of installing wind turbines which is one of the advantages of using residential-scale wind turbines.

Table 1. Monthly averaged wind speed in the stations under study

Station	Z(m)	Long.	Lat.	Jan.	Feb.	Mar.	Apr.	May	Jun.	Jul.	Aug.	Sep.	Oct.	Nov.	Dec.
AbuSamrah	114	50.8	24.8	3.6	4.1	3.9	3.6	3.9	4.4	4.1	4.0	3.6	3.3	3.2	3.6
Ar-Ruways	0	51.2	26.1	4.0	4.5	4.3	4.0	4.5	4.6	4.2	4.1	3.7	3.4	3.5	3.9
Doha	10	51.6	25.3	3.9	4.5	4.6	4.4	4.7	4.9	4.2	3.8	3.5	3.3	3.6	3.8
Duhan	30	50.8	25.4	3.7	4.2	4.0	3.7	4.1	4.4	4.1	4.0	3.6	3.3	3.2	3.6
Musayid	17	51.6	25.0	3.6	4.2	3.9	3.7	4.0	4.3	4.0	3.9	3.5	3.3	3.1	3.6

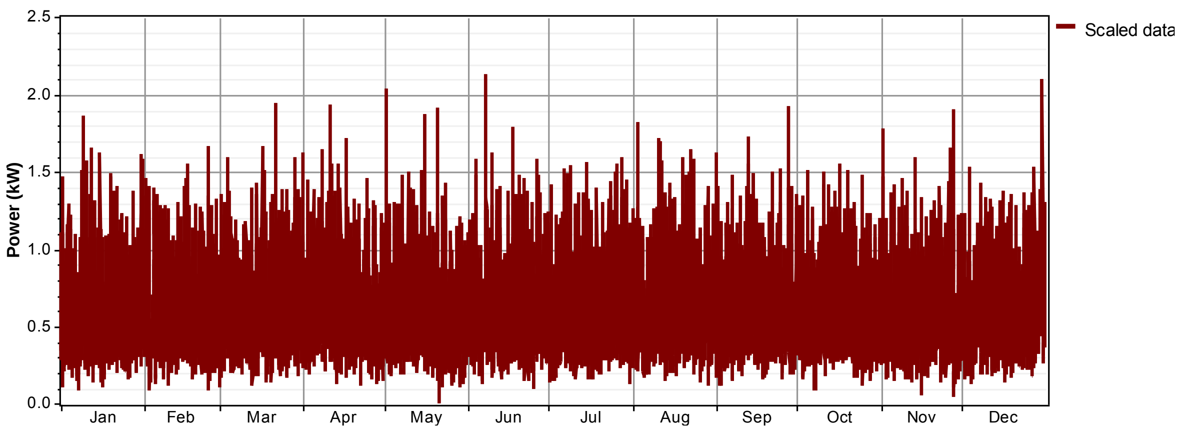

Figure 6. Annual required electricity amount.

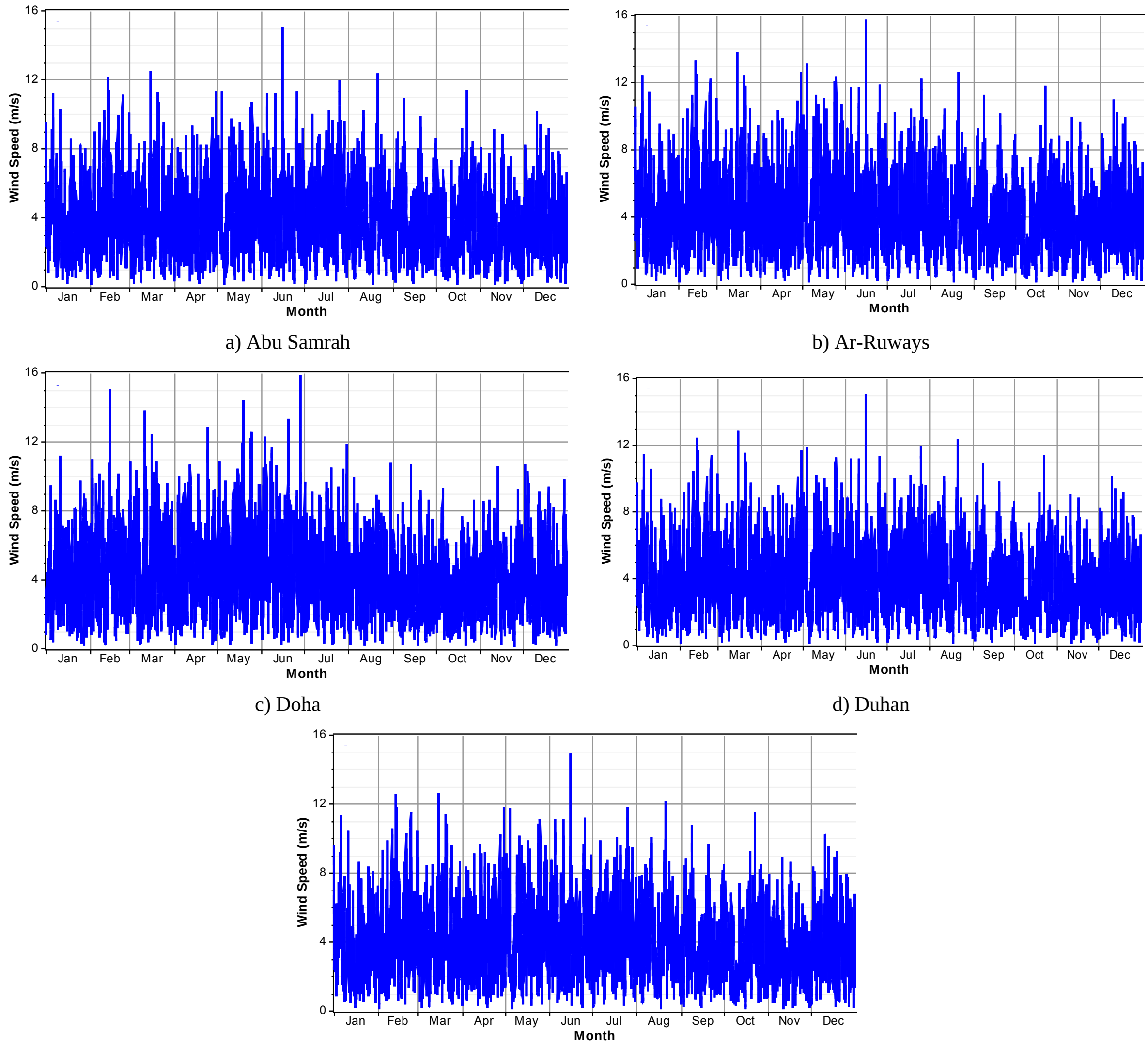

a) Abu Samrah

b) Ar-Ruways

c) Doha

d) Duhan

e) Musayid

Figure 7. The annual amount of wind speed for understudy stations.

Statistical methods were used to determine the wind energy potential in one of the areas of interest and to estimate the energy output of this site. A function that has proved accurate based on the measurements in various points of the world is the Weibull probability density distribution that requires k (shape factor) and c (scale factor) parameters and is in the following form [57]:

$$p(U) = \left(\frac{k}{c}\right)\left(\frac{U}{c}\right)^{k-1} \exp\left[-\left(\frac{U}{c}\right)^{k}\right] \quad (10)$$

where the scale parameter, *c*, indicates how strong the wind in a place is, while the shape parameter, *k*, means how peaked the wind distribution is, i.e. if the wind speeds tend to be very close to an absolute value, the distribution will have a high *k*-value and be very peaked. The empirical relations are used to determine *k* and *c*.

Wind turbines can convert 59.3% of the existing wind energy into electricity [58]. The turbine's power output (P) is given by the following relation [59]:

$$P = \frac{1}{2}\rho A V^3 C_p \quad (11)$$

where ρ is the air density [kg/m^3], A is the swept area [m^2], V is the wind speed [m/s], and C_p is the turbine's power factor for the corresponding wind speed.

The tall tower base of horizontal-axis wind turbines (HAWTs) allows access to the stronger wind in sites with wind shear which maximizes the power output of the turbine. Also, since the blades always move perpendicular to the wind, receiving power through the whole rotation, they are more efficient. The main advantage of vertical axis wind turbines (VAWTs) is that the wind turbine does not need to be pointed into the wind. This is an advantage on sites where the direction of the wind is very variable, such as on rooftops of residential buildings. Furthermore, with a vertical axis, the generator and other preliminary components can be placed nearby the ground, so the tower does not need to support it, which also makes maintenance easier. In the present work, 4 VAWTs and 4 HAWTs (commercially available) are used,and their specifications are presented in Table 2.

Table 2. Information of used wind turbines.

Power curve	Figure	Type
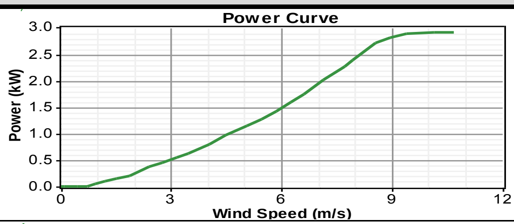		EOLO 3kW
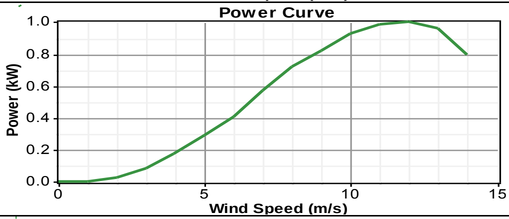		Spiral 1kW
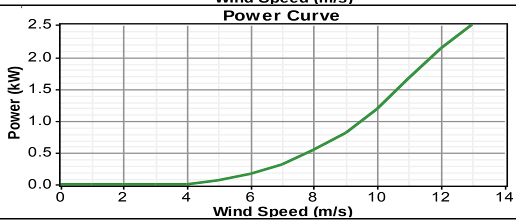		Turby 2.5 kW
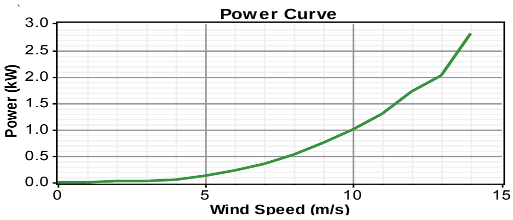		WRE 3kW
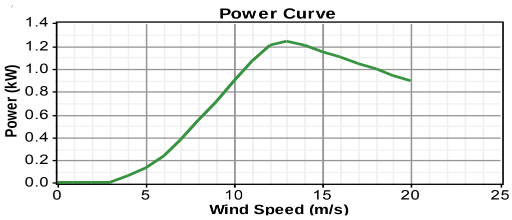		BWC XL.1
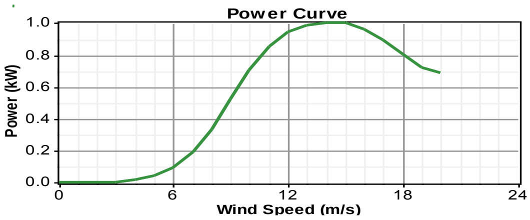		Generic 1 kW
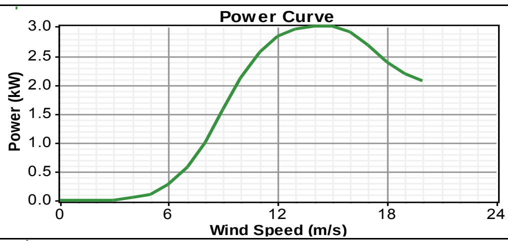		Generic 3 kW
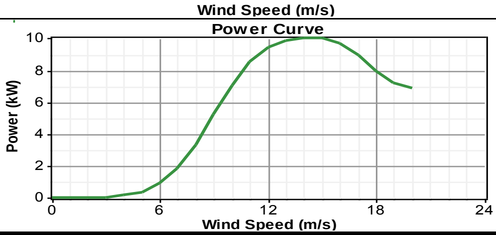		Generic 10 kW

Since Qatar is both lands- and sea-locked country, wind turbulence analysis in its stations is of high importance since the wind turbines are designed based on the wind speed and wind turbulence specifications [59]. Also, turbulence remarkably affects the applied fatigue loads on wind turbines, and a high level of turbulence reduces power generation and accelerates the fatigue of mechanical components [60, 61]. The following relation gives TI:

$$\mathrm{TI} = \frac{\sigma}{V_{ave}} \tag{12}$$

where σ is the standard deviation, V_{ave} is the average wind speed. The intensity of turbulence is ranked as low, mid, and high if it is ≤ 0.1, 0.1-0.25, and ≥ 0.25 [60], respectively.

4.2. The Price of Equipment

Since a diesel generator is used in the studied hybrid system, 0.56 $/l was entered into the software as the price of diesel [62]. Also, 5% was considered as the annual real interest rate [63]. The project lifetime of 25 years and zero pollution penalty were also taken into account. Table 3 summarizes the price, size, and type of equipment for the wind turbines selected for this study and shown in Table 2.

5. Results

Figure 8 shows the corresponding cumulative distribution function for the studied stations. The Weibull plot shows a good agreement with the measured speed shown in normalized form by a bar graph. As it could be seen from Figure 8, Abu Samrah (wind speed: 2-3.5 m/s; 38.7%), Ar-Ruways (2.5-3.5 m/s; 27.7%), Doha (2.5-3.5 m/s; 28.2%), Duhan (2-3 m/s; 28.8%), and Musayid (2-3.5 m/s; 38.5%) have the highest percentage of wind frequency, respectively. Also, c and k parameters determined based on the red line in Figure 8 and obtained by fitting to the experimental data of wind speed, are 4.25 m/s and 1.96, 4.58 m/s and 1.96, 4.63 m/s and 2.02, 4.31 m/s and 1.96, and 4.29 m/s and 1.96 for AbuSamrah, Ar-Ruways, Doha, Duhan, and Musayid stations, respectively.

As it could be observed in Figures 9 and 10, in Abu Samrah, Ar-Ruways, Doha, Duhan, and Musayid stations, the wind speed is higher than 4 m/s for 58.9, 53.9, 53, 58.1, and 58.5 percent of windy hours. Also, windy hours between the cut-in and cut-out speeds of most wind turbines, are 3598, 4043, 4119, 3675, 3633 hours/year(y), respectively. Windheim suggests 4000 running hours and a useful lifetime of 20 years for a wind turbine to be economically viable [74]. According to Windheim's criterion, therefore, using wind energy will be cost-effective for Ar-Ruways and Doha stations.

Table 3. Price, type and size of equipment.

Equipment	Price			Type
	Initial	Replacement	Operating & Maintenance	
Wind turbine BWC XL.1 [64]	2307	1845	10	Lifetime: 20 year Hub height: 25 m
Wind turbine Generic 1 kW [65]	2000	2000	20	Lifetime: 20 year Hub height: 25 m
Wind turbine Generic 3 kW [66]	9000	8000	15	Lifetime: 20 year Hub height: 25 m
Wind turbine Generic 10 kW [67]	6118	6118	35	Lifetime: 19 year Hub height: 25 m
Wind turbine EOLO [68]	5269	5269	130	Lifetime: 20 year Hub height: 10 m
Wind turbine Spiral [69]	1900	1900	48	Lifetime: 20 year Hub height: 10 m
Wind turbine Turby [70]	19243	19243	480	Lifetime: 20 year Hub height: 25 m
Wind turbine WRE [71]	13635	13635	340	Lifetime: 20 year Hub height: 25 m
Diesel generator [72]	3500	3000	0.023	Life time: 10000 h
Converter [72]	800	700	100	Life time: 15 year Efficiency: 90%
Battery Surrette 6CS25P [73]	1200	1100	50	Life time: 9645 kWh

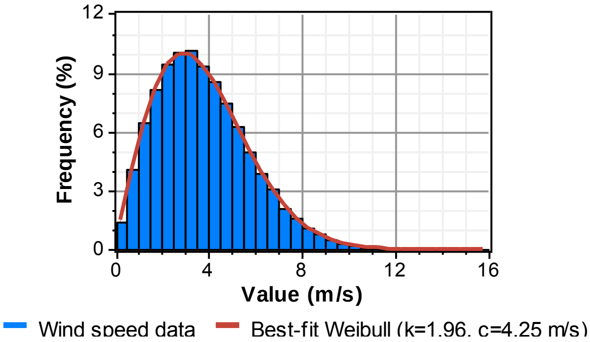

a) Abu Samrah

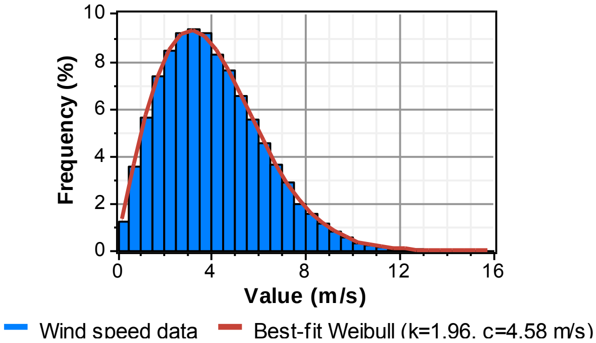

b) Ar-Ruways

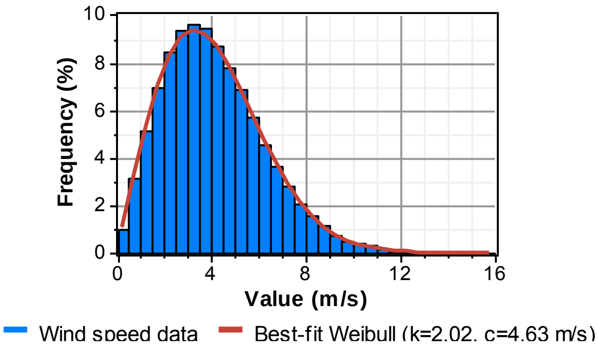

c) Doha

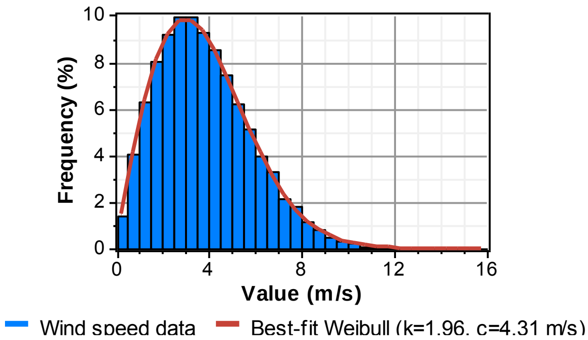

d) Duhan

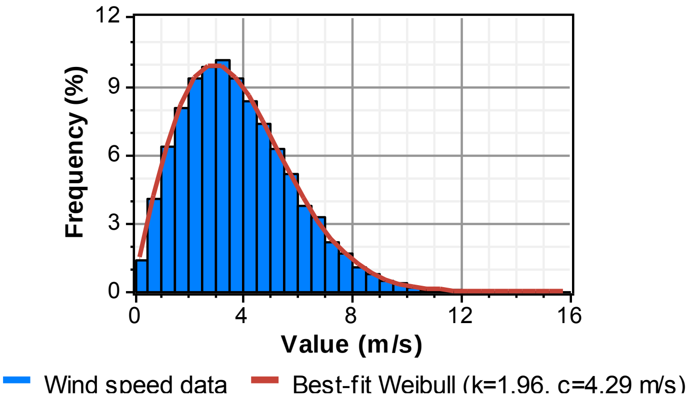

e) Musayid

Figure 8. Wind speed Weibull function.

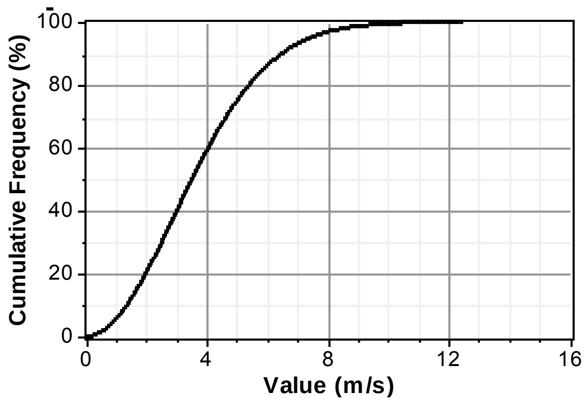

a) Abu Samrah

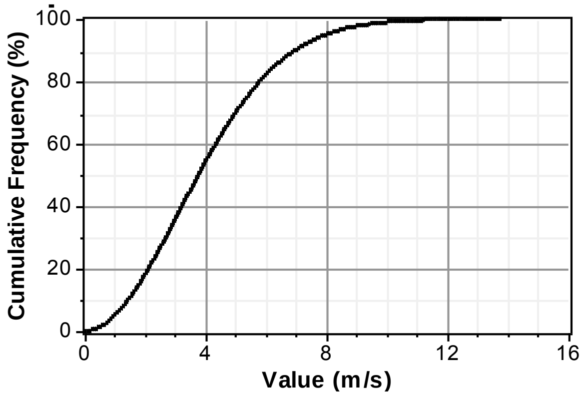

b) Ar-Ruways

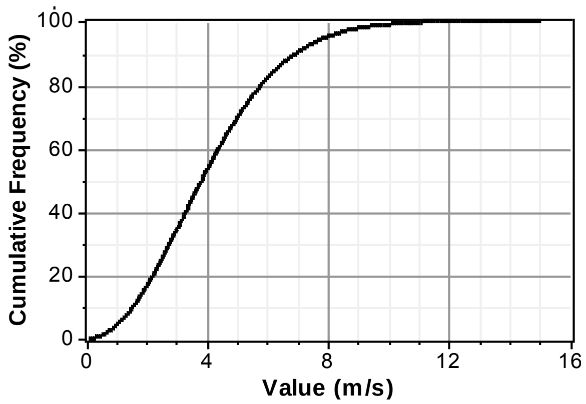

c) Doha

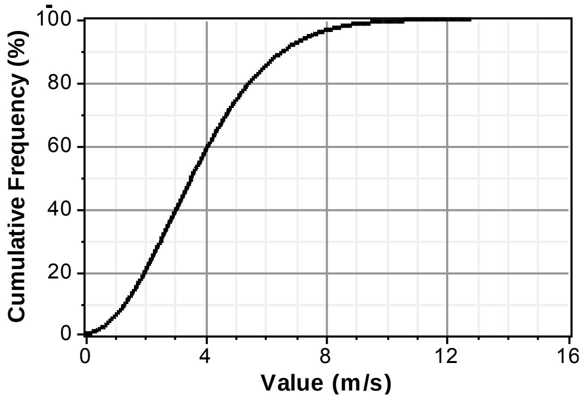

d) Duhan

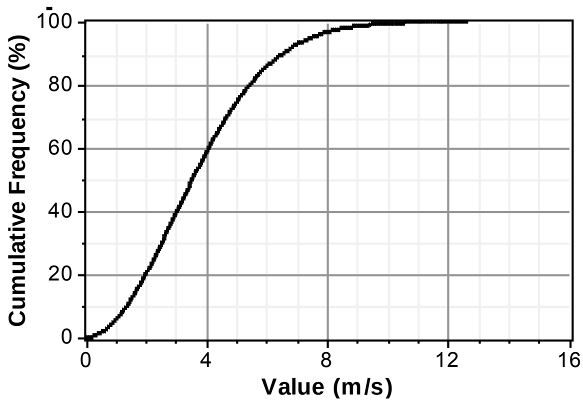

e) Musayid

Figure 9. Annual wind speed cumulative distribution function.

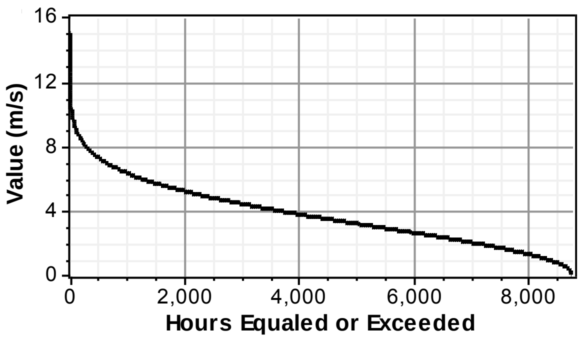

a) Abu Samrah

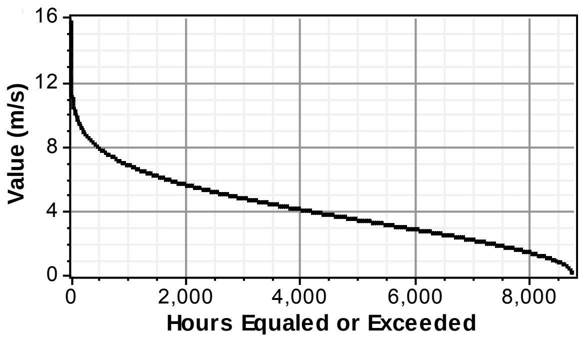

b) Ar-Ruways

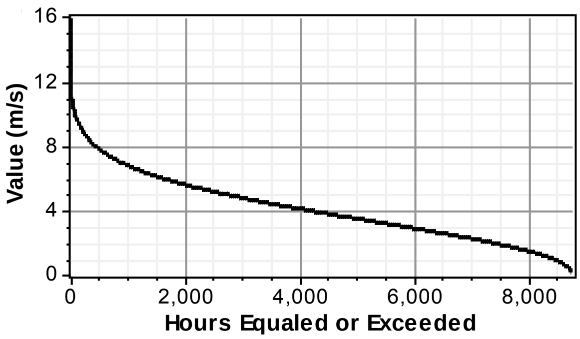

c) Doha

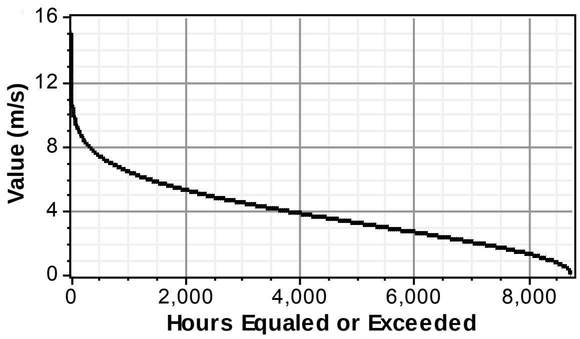

d) Duhan

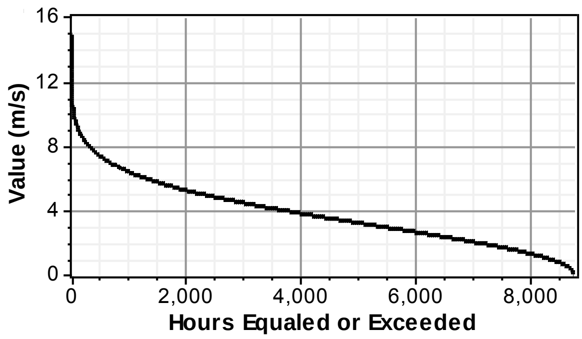

e) Musayid

Figure 10. Wind continuity-wind speed curve

In Table 4 the results of TIparameter are presented.

Table 4. Turbulence Intensity for studied stations

Station	TI
Abu Samrah	0.093
Ar-Ruways	0.096
Doha	0.127
Duhan	0.096
Musayid	0.095

From the results, it is evident that Abu Samrah, Ar-Ruways, Duhan, and Musayid stations have a low level of turbulence (< 0.1) and Doha has an intermediate level of turbulence (0.1-0.25) which means the mechanical components of wind turbines in 4 stations of Abu Samrah, Ar-Ruways, Duhan, and Musayid are under low fatigue loadings while in Duhan, these loadings are intermediate. The lowest and highest amounts of TI parameter are related to Abu Samrah (0.093) and Doha (0.127) stations, respectively. The average value of TI for all stations is equal to 0.101.

Table 5 summarizes the study results of 8 types of residential-scale wind turbines (4 HAWTs and 4 VAWTs) simulated by HOMER for the five target cities in Qatar. In this table, for Abu Samrah station, the most reasonable cost of generation per kWh of wind electricity and the total net present cost is obtained by the horizontal axis wind turbine (BWC XL.1) which is $0.088 and $6433, respectively. It should be noted, however, that the vertical axis wind turbine (Spiral), also occupies the second position regarding cost-effectiveness by $0.088 for the production cost per kWh of wind electricity and $6448 for the total net present cost. According to the results, the worst wind turbine to be used on a residential-scale in this station is TurbyVAWT with a cost production of $0.454 and a total NPC of $32870. Immediately following Turby, WRE VAWT ranks as the second-worst turbine to be used in Abu Samrah station by a production cost and total NPC of $0.337 and $24333, respectively. CO_2 is the most important, dangerous, and sizeable pollutant produced by diesel generators as a backup system. Given the results in Table 5, the most and least suitable wind turbines regarding contaminants are EOLO (-23.5 kg/y) and Turby (2844 kg/y) wind turbines. The highest amount of wind electricity (6908 kWh/y) is generated by EOLO VAWT producing 82% of total electricity generated by wind energy. The average values for production cost per kWh of wind electricity, totalNPC and electricity generated for Abu Samrah station are $0.1853, $ 13917.63, and 2622.5 kWh/y, respectively. For this station, EOLO VAWT is recommended for the residential-scale since it has a reasonable production cost per kWh of wind energy and the highest amount of electricity generated compared with other studied wind turbines. It not only produces no emissions, but also brings about harmful emissions due to selling a considerable amount of power to the national grid.

For Duha station, the most cost-effective electricity generation alternatives are BWC XL.1 HAWT and Spiral VAWT. The production cost per kWh of wind electricity and total NPC are $0.088 and $6417 for BWC XL.1 and $0.088 and $6432 for Spiral, respectively. Regarding CO_2 production, by emitting 2820 kg/y of CO_2, Turby ranks as the first least environmentally friendly wind turbine due to producing the lowest amount of wind electricity (704 kWh/y) and having the most significant dependence on a diesel generator. EOLO is the most environmentally friendly wind turbine since, due to producing a high level of wind electricity (7090 kWh/y), it sells more power to the national grid than it needs for the diesel generator and saves 72.3 kg CO_2 annually. In this station, the highest rate of wind electricity generation (7184 kWh/y) is associated with Generic 10 kW HAWT. The average values for production cost per kWh of wind electricity, total NPC, and electricity produced for Duhan station are $0.1846, $13967.63, and 2741 kWh/y, respectively.

Having a production cost of 0.086 $/kWh of wind electricity, BWC XL.1 HAWT is the most cost-effective turbine type for Ar-Ruways station followed by Spiral and Generic 1 kW turbines ($0.086 and $0.088, respectively). By a total NPC of $6350, BWC XL.1 turbine is the cheapest option for this station with Turby producing the most expensive wind electricity in this station by a COE of 0.45 $/kWh. Regarding CO_2 emissions, Turby and Generic 1kW turbines are the least suitable options by the annual production of 2716 and 2699 kg CO_2, respectively, while EOLO VAWT is the most environmentally friendly turbine by saving 245 kg/y CO_2. The lowest amount of wind electricity generation in this station (893 kWh/y) is related to Generic 1kW turbine, while Generic 10 kW wind turbine, by producing 8890 kWh/y, generates the highest amount of wind electricity. It is noteworthy, however, that the EOLO wind turbine makes the highest contribution to the total wind power generated by producing 85.1% of the total 9117 kWh/y. The average values for production cost per kWh of wind electricity, wholeNPC, and electricity generated for Ar-Ruways station are $0.1816, $13896.75, and 3231.8 kWh/y, respectively.

For Doha, the lowest and highest production costs per kWh of wind electricity generated are $0.086 and $0.45 associated with BWC XL.1 and Turby stations, respectively. The most cost-effective wind turbine, by a total NPC of $6349, is BWC XL.1. Also, the most and least suitable turbines regarding CO_2 emission are EOLO (-300 kg/y) and Turby (2720 kg/y). Considering the amount of electricity produced by wind energy, Generic 10 kW (8861 kWh/y) and Generic 1kW (890 kWh/y) have the highest and lowest values, respectively. It has to be mentioned, however, that the EOLO turbine takes the first place in producing the required electricity by supplying 86% of the total 9140 kWh of electricity annually. The average values for production costs per kWh of wind electricity, wholeNPC, and power generated for the Doha station are $0.1814, $13890.63, and 3238.1 kWh/y.

In Musayid station, BWC XL.1 and Spiral wind turbines are the most economical options having a price per kWh of electricity of $0.088 with BWC XL.1 (total NPC of $6422) slightly outperforming Spiral (entireNPC of $6436). From an economic point of view, Turby and WRE wind turbines, with production costs of $0.454 and $0.336 per kWh of electricity generated, are the least suitable ones. By producing -60.3 kg/y and 2828 kg/y CO_2, EOLO and Turby wind turbines are the most and least environmentally friendly options, respectively. The highest amount of wind electricity generated in this station is supplied by Generic 10 kW (7056 kWh/y, 70%) and EOLO (7045 kWh/y, 83%) wind turbines. The average values for production cost per kWh of wind electricity, total NPC, and power generated for Musayid station are $0.1849, $13973, and 2705.8 kWh/y, respectively. To sum up, it can be said that the Doha station with $0.086 per kWh of electricity generated which is due to using BWC XL.1 HAWT produces the most cost-effective wind electricity since it holds the lowest total NPC ($ 6349). The highest savings and production of CO_2 emissions are related to Doha (-300 kg/y) and Abu Samrah (2844 kg/y) stations, respectively. These pollutants are emitted by EOLO and Turby wind turbines, respectively. The highest (8890 kWh/y) and lowest (658 kWh/y) amounts of wind electricity generation are associated with Ar-Ruways and Abu Samrah stations using Generic 10 kW and Turby wind turbines, respectively. From the results, it is also evident that VAWTs are more costly than HAWTs. Furthermore, studies are indicative of the higher potential of wind energy for Ar-Ruways and Doha stations compared with other ones. The least suitable station for this purpose is Abu Samrah.

Table 6 compares theCOE of wind electricity in works performed in other parts of the world with the present work. Given that the present work uses 8 different types of wind turbines for different stations, the range of each kWh of generated wind power is between $ 0.086 to $ 0.454, which is in good agreement with countries close to Qatar such as Kuwait, Oman, and Saudi Arabia. The price of wind electricity in Qatar is also in the price range of the European Union, the United States, Japan, Taiwan, Turkey, Jordan, India, and the Eurasian region. This indicates that the Qatari wind energy potential is appropriate compared to other countries studied.

Table 5. Results of simulation.

Station	Turbine type	Total NPC ($)	COE ($/kWh)	CO_2 (kg)	Wind turbine production (kWh/y, % of total)
Abu Samrah	1	6451	0.089	2818	683, 13
	2	6433	0.088	2492	1259, 24
	3	14028	0.184	2235	2044, 35
	4	10392	0.131	1345	6787, 69
	5	10386	0.111	-23.5	6908, 82
	6	6448	0.088	2243	1694, 32
	7	32870	0.454	2844	658, 13
	8	24333	0.337	2672	947, 18
Duhan	1	6440	0.089	2796	722, 14
	2	6417	0.088	2459	1318, 25
	3	14006	0.183	2191	2164, 36
	4	10905	0.129	1289	7184, 71
	5	10362	0.110	-72.3	7090, 83
	6	6432	0.088	2209	1754, 33
	7	32858	0.454	2820	704, 13
	8	24321	0.336	2647	993, 19
Ar-Ruways	1	6393	0.088	2699	893, 17
	2	6350	0.086	2323	1560, 29
	3	13914	0.178	2003	2676, 42
	4	10793	0.125	1059	8890, 76
	5	10277	0.107	-245	7759, 85.1
	6	6369	0.086	2081	1979, 36
	7	32807	0.450	2716	912, 17
	8	24271	0.333	2545	1185, 22
Doha	1	6393	0.088	2700	890, 17
	2	6349	0.086	2319	1567, 29
	3	13911	0.178	1998	2667, 42
	4	10778	0.124	1029	8861, 77
	5	10250	0.106	-300	7845, 86
	6	6364	0.086	2072	1995, 37
	7	32809	0.450	2720	898, 17
	8	24271	0.333	2545	1182, 22
Musayid	1	6444	0.089	2803	710, 14
	2	6422	0.088	2469	1301, 24
	3	14013	0.183	2206	2125, 36
	4	10915	0.130	1308	7056, 70
	5	10368	0.111	-60.3	7045, 83
	6	6436	0.088	2218	1738, 32
	7	32862	0.454	2828	689, 13
	8	24324	0.336	2654	982, 19

1: Generic 1 kW 2: BWC XL 1 kW 3: Generic 3 kW 4: Generic 10 kW
5: EOLO 3 kW 6: Spiral1 kW 7: Turby 2.5 kW 8: WRE 3 kW

Table 6. Comparing the cost per kWh of wind power generation in different places with the present work

Ref.	Country	COE
[75]	China	0.021-0.023 EUR/kWh
[76]	European Union	0.2134 EUR/kWh
[77]	US	0.105-0.181 EUR/kWh
[77]	Japan	0.418 EUR/kWh
[78]	Taiwan	0.185 EUR/kWh
[77]	Canada	0.074 EUR/kWh
[79]	South Africa	0.363-1.601 $/kWh
[80]	Iran	0.674-2.847 $/kWh
[81]	Egypt	0.86 $/kWh
[82]	Saudi Arabia	0.0576 $/kWh
[83]	Oman	0.117 $/kWh
[84]	Kuwait	0.21-0.67 $/kWh
[85]	Turkey	0.348 $/kWh
[86]	Jordan	0.1108 $/kWh
[87]	Pakistan	0.0346 $/kWh
[88]	India	0.08 $/kWh
[88]	Eurasia	0.08 $/kWh
Present work	Qatar	0.086-0.454 $/kWh

6. Conclusion

Electricity demand in Middle Eastern countries is currently done mainly by traditional energy sources. Due to the negative impact of these resources and their depletion, as well as the increase in electricity demand, it seems that these countries should move towards renewable energy. Due to Qatar's relatively good potential in the field of wind energy, the use of wind energy at home scale is appropriate. According to studies, so far no comprehensive technical-economic-environmental potential measurement in the field of electricity supply at home scale using wind energy in Qatar has been done. Therefore, in the present work, using HOMER software, wind power generation is evaluated by 4 vertical axis turbines and 4 horizontal axis turbines in the on-grid mode for 5 stations located in Qatar. It should be noted that vertical axis wind turbines do not exist in the software database and have been added to the software by .txt files. Also, the use of up-to-date data on the price of equipment used, the real inflation rate, the up-to-date price of the national electricity grid, and the real price of diesel make the present work results usable with a very high percentage of confidence for energy decision-makers in Qatar. It should also be noted that the results of the present work can be used directly for regions with similar climates or the software and method of results analysis in the present work can be used for other regions of the world. The important results of the present work are:

- -By drawing Weibull functions and using the curve-fit method, parameters c and k were calculated for the studied stations.
- -By assessing the turbulence intensity parameter, it was observed that the wind turbines are only under relatively considerable fatigue loads at Doha station among the studied stations.
- - The minimum values of total NPC and COE parameters are $ 6349 and $ 0.086 per kWh, respectively, due to the use of BWC XL.1 horizontal axis wind turbine at Doha station.
- - The most environmentally friendly wind turbine that prevents the release of 300 kg of CO_2 emissions per year is EOLO 3kW, which is installed at the Doha station.
- - The highest wind power generation with at least 82% of the total electricity generated in all stations, is related to the EOLO 3kW vertical axis wind turbine.

Reference

[1] S. Coccolo, J. Kämpf, D. Mauree, J.L.Scartezzini, “Cooling potential of greening in the urban environment, a step further towards practice”. Sustainable cities and society, vol. 38, 2018, 543-559.

[2] H. Azizalrahman, “A model for urban sector drivers of carbon emissions”. Sustainable Cities and Society, vol. 44, 2019, 46-55.

[3] M.R. Abdelkader, A. Al-Salaymeh, Z. Al-Hamamre, F. Sharaf, “A comparative Analysis of the Performance of Monocrystalline and Multiycrystalline PV Cells in Semi-Arid Climate Conditions: the Case of Jordan”. Jordan Journal of Mechanical & Industrial Engineering, Vol. 4, 2010, 543- 552.

[4] L. Charfeddine, A.Y. Al-Malk, K. Al Korbi, “Is it possible to improve environmental quality without reducing economic growth: Evidence from the Qatar economy”. Renewable and Sustainable Energy Reviews, vol. 82, 2018, 25-39.

[5] The World Bank, CO_2 emissions (metric tons per capita) Qatar 2014. https://data.worldbank.org/indicator/EN.ATM.CO2E.PC?year_high_desc=true, 2018[Accessed 02 December 2018].

[6] F.E. Al-Thawadi, S.G. Al-Ghamdi, “Evaluation of sustainable urban mobility using comparative environmental life cycle assessment: A case study of Qatar”. Transportation Research Interdisciplinary Perspectives, vol. 1, 2019, 100003 (1-8).

[7] C. Lanouar, A.Y. Al-Malk, K. Al Karbi, “Air pollution in Qatar: Causes and challenges”. White Paper, vol. 1, 2016, 1-7.

[8] N.C. Onat, M. Kucukvar, N.N. Aboushaqrah, R. Jabbar, “How sustainable is electric mobility? A comprehensive sustainability assessment approach for the case of Qatar”. Applied Energy, vol. 250, 2019, 461-477.

[9] M.Z. Jacobson, M.A. Cameron, E.M. Hennessy, I.Petkov, C.B. Meyer, T.K.Gambhir, A.T. Maki, K.Pfleeger, H.Clonts, A.L. McEvoy, M.L.Miccioli,“100% clean and renewable Wind, Water, and Sunlight (WWS) all-sector energy roadmaps for 53 towns and cities in North America”. Sustainable Cities and Society, vol. 42, 2018, 22-37.

[10] A. Kamal, S.G. Al-Ghamdi, M. Koç, “Role of energy efficiency policies on energy consumption and CO_2 emissions for building stock in Qatar”. Journal of Cleaner Production, vol. 253, 2019, 1409-1424.

[11] M. Salahuddin, J. Gow, “Effects of energy consumption and economic growth on environmental quality: evidence from Qatar”. Environmental Science and Pollution Research, vol. 26, 2019, 18124-18142.

[12] A. Qazi, F. Hussain, N.A. Rahim, G. Hardaker, D. Alghazzawi, K. Shaban, K. Haruna, “Towards Sustainable Energy: A Systematic Review of Renewable Energy Sources, Technologies, and Public Opinions”. IEEE Access, vol. 7, 2019, 63837-51.

[13] W. Al-Marri, A. Al-Habaibeh, M. Watkins, “An investigation into domestic energy consumption behaviour and public awareness of renewable energy in Qatar”, Sustainable cities and society, vol. 41, 2018, 639-646.

[14] A.S. Ahmed, “Analysis the economics of sustainable electricity by wind and its future perspective”. Journal of Cleaner Production, vol. 224, 2019, 729-38.

[15] M. Al Zou'bi, "Renewable energy potential and characteristics in Jordan". Jordan Journal of Mechanical & Industrial Engineering, Vol. 4, 2010, 45-48.

[16] K. Al-Salem, S. Neelamani, W. Al-Nassar, "Wind Energy Map of Arabian Gulf". Natural Resources, vol. 9, no. 5, 2018, 212-228.

[17] J. Yang, Y. Chang, L. Zhang, Y. Hao, Q. Yan, C. Wang, "The life-cycle energy and environmental emissions of a typical offshore wind farm in China". Journal of Cleaner Production, vol. 180, 2018, 316-324.

[18] S.A. Ahmed, H.O. Mahammed, "A statistical analysis of wind power density based on the Weibull and Ralyeigh models of "Penjwen Region" Sulaimani/Iraq". Jordan Journal of Mechanical and Industrial Engineering, Vol. 6, 2012, 135-140.

[19] G. Kavari, M. Tahani,M. Mirhosseini, "Wind shear effect on aerodynamic performance and energy production of horizontal axis wind turbines with developing blade element momentum theory". Journal of Cleaner Production, vol. 219, 2019, 368-376.

[20] M. Shoaib, I. Siddiqui, S. Rehman, S. Khan, L.M. Alhems,"Assessment of wind energy potential using wind energy conversion system". Journal of Cleaner Production, vol. 216, 2019, 346-360.

[21] KQED Science, "Wind, Not Water, to Blame for Drought, Says Study". https://www.kqed.org/science/833862/wind-not-water-to-blame-for-drought-says-study/; 2016 [Accessed 15 November 2018].

[22] P.J. Simons, W.M. Cheung, "Development of a quantitative analysis system for greener and economically sustainable wind farms". Journal of Cleaner Production, vol. 133, 2016, 886-898.

[23] H. Zhou, Y. Lu, X. Liu, R. Chang, B. Wang, "Harvesting wind energy in low-rise residential buildings: Design and optimization of building forms". Vol. 167, 2017, 306 316.

[24] World Energy Council, "Energy Resources, Wind". https://www.worldenergy.org/data/resources/resource/wind/; 2018 [Accessed 01 November 2018].

[25] G. Bekele, B. Palm, "Wind energy potential assessment at four typical locations in Ethiopia". Applied Energy, vol. 86, no. 3, 2009, 388-396.

[26] R.V. Rodrigues, L.A. Rossi, "Performance of small wind turbines: simulation of electricity supply to loads connected to the public or isolated grid". EngenhariaAgrícola, vol. 36, no. 2, 2016, 281-290.

[27] T.R. Ayodele, A.S.O. Ogunjuyigbe, "Wind energy potential of Vesleskarvet and the feasibility of meeting the South African′s SANAE IV energy demand". Renewable & Sustainable Energy Reviews, vol. 56, 2016, 226-234.

[28] M. Qolipour, A. Mostafaeipour, S. Shamshirband, O. Alavi, H. Goudarzi, D. Petković, "Evaluation of wind power generation potential using a three-hybrid approach for households in Ardebil Province, Iran". Energy Conversion and Management, vol. 118, 2016, 295-305.

[29] M. Becerra, J. Moran, A. Jerez, F. Cepeda, M. Valenzuela, "Wind energy potential in Chile: Assessment of a small scale wind farm for residential clients". Energy Conversion and Management, vol. 140, 2017, 71-90.

[30] M. Qolipour, A. Mostafaeipour, M. Rezaei, "A mathematical model for simultaneous optimization of renewable electricity price and construction of new wind power plants (case study: Kermanshah)". International Journal of Energy and Environmental Engineering, vol. 9, no. 1, 2018, 71-80.

[31] S.M. Shaahid, L.M. Alhems, M.K. Rahman, "Potential of Development of Wind Farms in Turaif Saudi Arabia–A Case Study to Mitigate the Challenges of Fossil Fuel Depletion". International Journal of Applied Engineering Research, vol. 13, no. 3, 2018, 1798-1804.

[32] C. Méndez, Y. Bicer, "Qatar's Wind Energy Potential with Associated Financial and Environmental Benefits for the Natural Gas Industry". Energies, vol. 12, no. 17, 2019, 3329.

[33] Wikipedia, Qatar. https://en.wikipedia.org/wiki/Qatar/; 2018 [Accessed 20 November 2018].

[34] World Population Review, "Qatar Population 2018". http://worldpopulationreview.com/countries/qatar-population/; 2018 [Accessed 20 November 2018].

[35] iExplore, "Qatar - Weather". https://www.iexplore.com/articles/travel-guides/middle-east/qatar/weather/; 2017 [Accessed 17 November 2018].

[36] R. Chamoun, W. Chakroun, "Cost-efficiency study of BIPV systems in Qatar Residential Houses". International Journal of Renewable Energy Research, vol. 4, no. 3, 2014, 571-579.

[37] Z. Abdmouleh, A. Gastli, L. Ben-Brahim, "Survey about public perception regarding smart grid, energy efficiency & renewable energies applications in Qatar". Renewable & Sustainable Energy Reviews, vol. 82, no. 1, 2018, 168-175.

[38] N. Ayoub, F. Musharavati, S. Pokharel, H.A. Gabbar, "Energy consumption and conservation practices in Qatar-A case study of a hotel building". Energy Buildings, vol. 84, 2014, 55-69.

[39] F. Touati, N.A. Chowdhury, K. Benhmed, A.J.S.P. Gonzales, M.A. Al-Hitmi, M. Benammar, A. Gastli, L. Ben-Brahim, "Long-term performance analysis and power prediction of PV technology in the State of Qatar". Renewable Energy, vol. 113, 2017, 952-65.

[40] International Energy Agency (iea). "IEA Statistics Qatar". https://www.iea.org/statistics/statisticssearch/repor &product=indicators/; 2014 [Accessed 17 September 2018].

[41] M. Schenckery, Z. Yibo, M. Ranjana, "Modeling a regional energy system in a smart city & low emissions perspective: Scenarios for energy transition in Qatar". Qatar Foundation Annual Research Conference Proceedings,vol. 2018, no. 1, 2018, EEPP304.

[42] L. Charfeddine, A.Y. Al-Malk, K. Al Korbi, "Is it possible to improve environmental quality without reducing economic growth: Evidence from the Qatar economy?". Renewable & Sustainable Energy Reviews, vol. 82, no. 1, 2018, 25-39.

[43] Z. Cen, P. Kubiak, C.M. López, I. Belharouak, "Demonstration study of hybrid solar power generation/storage micro-grid system under Qatar climate conditions". Solar Energy Materials and Solar Cells, vol. 180: 2018, 280-288.

[44] S. Masiur Rahman, A.N. Khondaker, M. Imtiaz Hossain, M. Shafiullah, M. Hasan, "Neurogenetic modeling of energy demand in the United Arab Emirates, Saudi Arabia, and Qatar". Environmental Progress & Sustainable Energy, vol. 36, no. 4, 2017, 1208-1216.

[45] W.E. Alnaser, N.W. Alnaser, "Solar and wind energy potential in GCC countries and some related projects". Journal of Renewable and Sustainable Energy, vol. 1, no. 2, 2009, 022301.

[46] Global Wind Atlas. "Qatar". https://globalwindatlas.info/Qatar/; 2018 [Accessed 17 October 2018].

[47] P. Kumar, R. Pukale, N. Kumabhar, U. Patil, "Optimal design configuration using HOMER". Procedia Technology, vol. 24, 2016, 499-504.

[48] A. Teimourian, A. Bahrami, H. Teimourian, M. Vala, A.O. Huseyniklioglu, "Assessment of wind energy potential in the southeastern province of Iran". Energy Sources, Part A: Recovery, Utilization, and Environmental Effects, vol. , 2019, 1-5.

[49] HOMER Energy, "The HOMER Pro". https://www.homerenergy.com/products/pro/index.html/; 2018 [Accessed 28 October 2018].

[50] M. Jahangiri, A. Haghani, S. Heidarian, A. Alidadi Shamsabadi, L.M. Pomares, "Electrification of a tourist village using hybrid renewable energy systems, Sarakhiyeh in

Iran". Journal of Solar Energy Research, Vol. 3, 2018, 201-211.

[51] M. Jahangiri, A. Haghani, A. Mostafaeipour, A. Khosravi, H.A. Raeisi, "Assessment of solar-wind power plants in Afghanistan: A review". Renewable and Sustainable Energy Reviews, Vol. 99, 2019, 169-190.

[52] R.E. Ganoe, P.W. Stackhouse, R.J. DeYoung, "RETScreen® plus Software Tutorial". National Aeronautics and Space Administration (NASA), 2017, 3-27.

[53] Qatar General Electricity & Water Corporation, "Electricity tariff". https://www.km.com.qa/CustomerService/Pages/Tariff.aspx/; 2018 [Accessed 22 November 2018].

[54] A. Tummala, R.K. Velamati, D.K. Sinha, V. Indraja, V.H. Krishna, "A review on small scale wind turbines". Renewable and Sustainable Energy Reviews, Vol. 56, 2016, 1351-1371.

[55]Level, Wind turbine systems, http://www.level.org.nz/energy/renewable-electricity-generation/wind-turbine-systems [Accessed 16 January 2021]

[56] A. Mostafaeipour, "Feasibility study of harnessing wind energy for turbine installation in province of Yazd in Iran". Renewable & Sustainable Energy Reviews, vol. 14, no. 1, 2010, 93-111.

[57] J.F. Manwell, J.G. McGowan, A.L. Rogers,"Wind Energy Explained: Theory, Design and Application". John Wiley & Sons; 2002.

[58] J. Vignesh, A.S. Christopher, T. Albert, C.P.T. Selvan, J. Sunil, "Design and fabrication of vertical axis wind mill with solar system". Materials Today: Proceedings, Vol. 21, 2020, 10-14.

[59] S. Kucukali, C. Dinçkal, "Wind energy resource assessment of Izmit in the West Black Sea coastal region of Turkey". Renewable & Sustainable Energy Reviews, vol. 30, 2014, 790-5.

[60] P. Jain,"Wind Energy Engineering". United States of America: McGraw Hill, 2011.

[61] Vestas, "Vestas Brochures". http://www.vestas.com/en/media/brochures.aspx/; 2012 [Accessed 19 November 2018].

[62] Global Petrol Prices, "Gasoline prices, liter". https://www.globalpetrolprices.com/gasoline_prices/; 2018 [Accessed 17 December 2018].

[63] Trading Economics, "Interest Rate | Asia". https://tradingeconomics.com/country-list/interest-rate?continent=asia/; 2018 [Accessed 10 December 2018].

[64] R. Srivastava, V.K. Giri, "Optimization of hybrid renewable resources using HOMER". International Journal of Renewable Energy Research, vol. 6, no. 1, 2016, 157-163.

[65] F. Bulut, L.Ü.Y. Murat, Ç.A.M. Ertugrul, "The effects of incentives on renewable energy resources for home users". International Journal of Energy Applications and Technologies, vol. 4, no. 2, 2017, 94-100.

[66] R. Usman, A. Gidado, "Feasibility analysis of a grid-connected PV/wind options for rural healthcare centre using homer". European Journal of Engineering and Technology, vol. 5, no. 3, 2017, 12-20.

[67] A.R. Syarifah, A.G. Abdullah, D.L. Hakim, A.B.D. Nandiyanto, "Design of Hybrid Power System for Remote Area". IOP Conference Series: Materials Science and Engineering,vol. 288, no. 1, 2018, 012010.

[68] Makemu green energy. https://www.makemu.it/; 2018 [Accessed 18 October 2018].

[69] 1000W Spiral Small Vertical Axis Wind Turbine, http://maxtuoch.en.made-in-china.com/product/bKnEIGlJuUYB/China-1000W-Spiral-Small-Vertical-Axis-Wind-Turbine.html/; 2018 [Accessed 30 October 2018]

[70] K. Syngellakis, P. Clement, J. Cace, "Wind energy integration in the urban environment (WINEUR)". Techno-economic report. European Commission, 2005.

[71] GREEN WORLD GROUP. "Products". http://greenworldgroup.net/en/products/; 2018, [Accessed 25 October 2018].

[72] M. Jahangiri, O. Nematollahi, A. Sedaghat, M. Saghafian, "Techno-economical assessment of renewable energies integrated with fuel cell for off grid electrification: A case study for developing countries". Journal of Renewable and Sustainable Energy, vol. 7, no. 2, 2015, 023123.

[73] S. Vahdatpour, S. Behzadfar, L. Siampour, E. Veisi, M. Jahangiri, "Evaluation of off-grid hybrid renewable systems in the four climate regions of Iran". Journal of Renewable Energy and Environment, vol. 4, no. 1, 2018, 61-70.

[74] R. Windheim, "Wind energy utilization Status of research and development in the Federal Republic of Germany". Wind power '85 Conference, San Francisco, CA (USA), 1985.

[75] M.S. Nazir, Y. Wang, B. Muhammad, M.S. Hafiz, A.A. Kadhem, H.M. Nazir, A.N. Abdalla, Y. Ma, "Comparison of small-scale wind energy conversion systems: economic indexes". Clean Technologies, vol. 2, no. 2, 2020, 144-155.

[76] Eurostat. 2021, Electricity price statistics. https://ec.europa.eu//statistics-explained/index.php?title=Electricity_price_statistics#Electricity_prices_for_household_consumers.

[77] DOE. 2017 Wind Technologies Market Report; DOE: Washington, DC, USA, 2018

[78] C.C.M. Chagas, M.G. Pereira, L.P. Rosa, N.F. da Silva, M.A.V. Freitas, J.D. Hunt, "From megawatts to kilowatts: A review of small wind turbine applications, lessons from the US to Brazil". Sustainability, vol. 12, no. 7, 2020, 2760.

[79] A. Mostafaeipour, M. Jahangiri, A. Haghani, S.J.H. Dehshiri, S.S.H. Dehshiri, A. Sedaghat, H. Saghaei, E.T. Akinlabi, S.M. Sichilalu, M.S. Chowdhury, K. Techato, "Statistical evaluation of using the new generation of wind turbines in South Africa". Energy Reports, vol. 6, 2020, 2816-2827.

[80] T. Abdali, S. Pahlavan, M. Jahangiri, A. Alidadi Shamsabadi, F. Sayadi, "Techno-Econo-Environmental study on the use of domestic-scale wind turbines in Iran". Energy Equipment and Systems, vol. 7, no. 4, 2019, 317-338.

[81] M.A. Badr, A.N. Mohib, M.M. Ibrahim, "Small Wind Turbine Hybrid System for Remote Application: Egyptian Case Study". International Journal of Computer and Systems Engineering, vol. 8, no. 9, 2014, 1584-1589.

[82] S.M. Shaahid, L.M. Al-Hadhrami, M.K. Rahman, "Potential of establishment of wind farms in western province of Saudi Arabia". Energy Procedia, vol. 52, 2014, 497-505.

[83] A.H. Al-Badi, "Wind power potential in Oman". International Journal of Sustainable Energy, vol. 30, no. 2, 2011, 110-118.

[84] A. Hajiah, M. Sebzali, S. Ebrahim, "Analysis of wind power potential characteristics and feasibility in Kuwait for possible electricity production". International Journal of Renewable Energy Research (IJRER), vol. 3, no. 4, 2013, 812-818.

[85] S. Değirmenci, "Environmental impact and capacity analysis of renewable energy resources: case study of wind energy in turkey". Master of Science Thesis, Izmir Institute of Technology, 2016.

[86] S. Kiwan, E. Al-Gharibeh, E. Abu-Lihia, "Wind Energy Potential in Jordan: analysis of the first large-scale wind farm and techno-economic assessment of potential farms". Journal of Solar Energy Engineering, vol. 143, no. 1, 2021, 011007.

[87] Z.H. Hulio, "Assessment of Wind Characteristics and Wind Power Potential of Gharo, Pakistan". Journal of Renewable Energy, vol. 2021, 2021, 8960190.

[88] E.R.M. Shouman, "Global prediction of wind energy market strategy for electricity generation". In book: Modeling, Simulation and Optimization of Wind Farms and Hybrid Systems, 2020.

JJMIE

Volume 15, Number 2, June. 2021
ISSN 1995-6665
Pages 233 - 241

Jordan Journal of Mechanical and Industrial Engineering

Magnus Wind Turbine Effect Vertical Axis Using Rotating Cylinder Blades

Khalideh Al bkoor Alrawashdeh*, Nabeel.S.Gharaibeh, Abdullah A. Alshorman, Mohamad H. Okour

Mechanical Engineering Department, Al-Huson University College, Al-Balqa' Applied University, P.O.Box 50, Al-Huson, 19117 Irbid, Jordan.

Received July 17 2020 *Accepted November 30 2020*

Abstract

The aerodynamic characteristics of a Magnus wind turbine (MWT) with cylinder blades are evaluated by using numerical simulation COMSOL. Yaw and lifting systems are used to identify the features of the MWT to maximizing power output at minimum tresses, torque and fatigue. MWT is characterized by low efficiency of power production. Therefore, it is important to seek effective components to improve the power performance of MWT. The blades design in Yaw and lifting system are critical parameters that affect MWT performance. In this study, five suggestions were discussed to choose the best configurations of MWT in order to promote MWT application. Performance characteristics, such as stresses, Torque, deflection and fatigue with suggested configurations are analyzed and compared to identify the desirable components for this type of MWT. The results showed that the aerodynamic characteristics of MWT in this study will be presented as a significance guide for the initial research and preliminary design of MWT. Based on the suggested design configuration, the results showed that the Von Mises stresses are low at the bottom and high at the top, and the buckling is very high at the top but low at the bottom of the base while the maximum value of Findley's fatigue is for the bottom as a result of axial stress. As for the designed shaft, the force increases when the stress increases accordingly, therefore, the deflection also increases. Moreover, the results showed more specified ranges of stresses distributions on blades and deflection ranges of decrease and increase that enable for better design, control and power utilization of turbine.

Keywords: Magnus effect, wind turbine, stress, deflection, torque, yaw system;

1. Introduction

The world today faces a continuous looming threat of limited resources and energy; the burning of fuel can no longer be viewed as the only means to obtain energy. Renewable (Khatri et al., 2010), safe and sustainable ways of generating energy must be developed, and it is always the responsibility of engineers to make that possible. The wind power plays an important role in tackling climate change, and that through new designs and concepts, it allows for greater yield and efficiency of energy in its application. Wind turbines (WT) have come a long way in a short period of time since their initial development in the 1970s; consumption of electricity of grid and its cost had fallen greatly (Kaygusuz. K, 2004).

The regular wind turbines need high wind speed, which is not available in the Middle East as the average wind speed is 5.5 m/s (Musgrove. p, 1993; Ahmeda and Mahammeda , 2012; Jinbo et al., 2015). Wind turbines take advantage of wind power by converting the kinetic energy to electrical energy (Lu. X et al., 2009; Messaoud and Abdessameda, 2011). Wind power has proven to be one of the most efficient and economical sources. It is environmentally energy friendly (Fauzan et al., 2017).

Under the force of the wind, the blades will rotate around a horizontal or vertical axis, and this kinetic energy will drive the turbine to generate power (Benatiallah et al., 2010; Fredous et al., 2011, Ghenai, 2017; Messaoud et al., 2018). Electricity production depends on the speed of the airflow and blades design (Cox et al., 2017; AEO, 2017; Mishra et al., 2017). Wind turbines are manufactured in two local sizes, which are building - mounted and pole mounted (Kunz et al., 2007; WWEA, 2012; Minderman et al., 2012). Pole mounted turbines are free standing in a suitable position, generating 5 kW and more of electricity (Tangler, 1994, Schube et al., 2012). Building mounted turbines are small - sized, where it can be located on the roof and between buildings, and generate less power than the pole mounted turbines (Owens, 2014; Messaoud et al., 2018). Small turbines are used for applications such as charging a battery of a car, boat, caravans and to power traffic signs and for lighting small area like camps, parking and small fields.

The first MWT consisted of a brass cylinder fitted between two bearings and rotated at high speed using a string (Golding, 1976). The cylinder was attached to a freely

* Corresponding author e-mail: khalideh19@bau.edu.jo.

rotating arm and air from a blower was directed towards it (Seifert, 2012). As the Cylinder rotated, it was noticed that the spinning cylinder always tended to deflect towards the side of the rotor that was traveling in the same direction as the wind coming from the blower (Seifent. J, 2012; BORG, 1986). The idea of using the Magnus effect in many applications leads to develop a cylinder-blade windmill by coiling the spiral fins around the cylinders producing a spiral Magnus turbine (Sun et al., 2012). When the spiral cylinders catch the wind, the rotating force is generated due to the aerodynamic properties caused by Magnus Effect. The technologies of WT in conjunction with the Magnus effect has progressed greatly, in addition, electricity generation has risen almost exponentially.

The main objective of this study is to use the Magnus effect to rotate the blades at a lower airspeed. The suggested design utilizes wind energy and the Magnus effect as a lifting force on the circulating airfoil blade attached to a wind turbine design. The circulating airfoil shape is a new concept developed theoretically and will be implemented for the first time. The circulating airfoil design will be scaled to match that of a NAC,A0021 airfoil which shows high aerodynamic quality (Abbott and Doenhoff, 1959; Gregorck, 1989).

This study utilizes Magnus effect as a lifting force on circulating an airfoil blade attached to a wind turbine design. The circulating airfoil will rotate around its axis resulting in high pressure on a side while the other side will have low pressure which leads to lifting the rotor. The turbine is going to be portable where it can fit into small areas; such as small camping areas, small apartments, parking and a small park.

2. Modelling of MWT

The blade design will be the new circulating airfoil blade design consisting of two different sized cylinders, one of which is connected to a DC motor to circulate the airfoil surface and the other one rotating freely and maintaining the airfoil shape as shown in figure 1a. The hub of the wind turbine will house the two DC motors connected to two circulating airfoil blades. Also, there will be a generator that is connected to the blade's shaft to change the rotation action to energy that will be stored in a battery.

The study reported in this paper examines, using numerical analyzed, the aerodynamic characteristics of a MWT with cylinder blades in Yaw and lifting system to identify the features of the MWT to maximizing power output at minimum tresses, torque and fatigue, in addition to the influences of deflection.

The block diagram in figure 1b shows how the MWT works. Initially, battery 1 will turn on the cylinders of the blades of the Magnus wind turbine. The wind will attack the blades applying high pressure on the side of the blade that is rotating in the opposite direction of the wind. While the other side will have low pressure since it is rotating in the same direction as the wind. Therefore, the net force will result in lifting the blades. Then the transformation of kinetic energy into electrical energy will be done by the generator, which is connected to the blades by a rotating shaft with a gearbox. The generator will defuse the electrical energy for three different purposes. The first one will be for charging battery 1, which is the response to turn on the yaw system, the lift system and the initialization system. The second purpose is to charge battery 2 until sunset and discharge the stored energy for lighting after that. The third one is to transfer direct electrical power to lighting. There will be an emergency manual braking system that is connected to the rotating shaft to shut down the machine when needed. Also, the blades can be turned on manually in case the battery is dead.

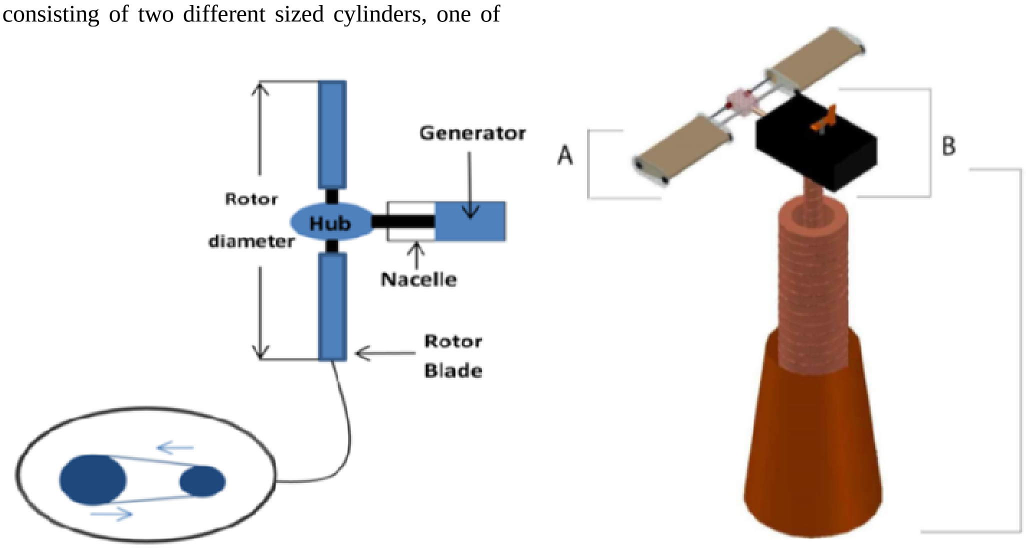

Part	Part Name	Description
A	Rotor Part	Converting wind speed to kinetic energy.
B	Power Generation Part	Converting mechanical energy to electrical power.
C	Tower Part	Support and lift the turbin.

Figure.1a: The mechanism of the MWT

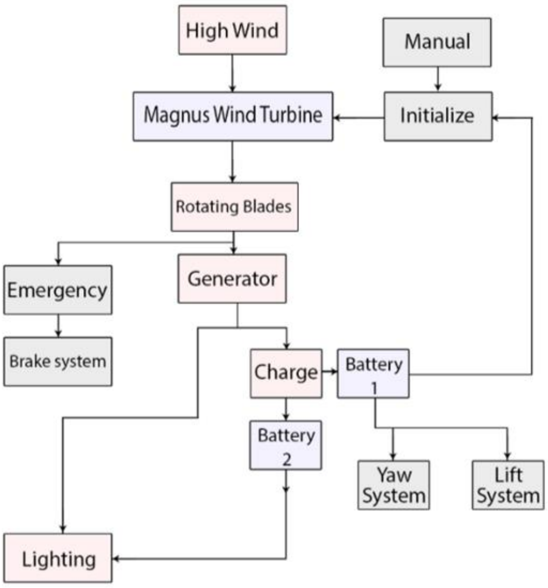

Figure.1b: The operation mechanism of the MWT

Figure 2 shows the rotation part of the blades (A), the power generator part –Nacelle (B). Table 1a shows the entire components of part A with the description, material, and manufacturing process. This part of the MWT consists of two blades; each one consists of two cylinders, two holders and a shaft that is connected to the motors through the coupler. The hub connects the blades to the low-speed shaft that is connected to the gearbox. The low-speed shaft will pass through a ball bearing that will be installed inside the hub to reduce the friction and to rotate the shaft smoothly.

In part B, the two shafts in this part are the high-speed shaft which will help to generate electricity and the other shaft is the lower speed shaft which is connected to the blades through the hub. The chokes are attached to the low speed shaft to support and keep it stable. The microcontroller, the indicator, and the yaw motor are representing the yawing system that rotates the turbine to face the wind's direction. A generator is attached to the high-speed shaft to generate power. The braking system is attached to the low-speed shaft for the emergency stop. Finally, the gearbox is used to transmit the rotation of the low-speed shaft to the high-speed shaft to generate power from the generator. Table1b shows the entire components with the description, material, and the manufacturing process.

Table.1a: Components of part A of MWT.

Part #	Part Name	description	Material	Manufacturing process
1	Large Blade's Shafts	Rotate blades	Aluminum	Purchased
2	Small Blade's cylinders	Rotate blades	Aluminum	Purchased
3	Hub	Keep shafts stable	Aluminum	Purchased
4	Ball Bearings	Smooth rotation	Aluminum	Purchased
5	Blade's Edges	Keeps cylinders in place	Rubber	Purchased
6	Stationary Shafts	Support the blade	Aluminum	Manufactured
7	Belt	Airfoil shape	Aluminum	Manufactured
8	Motors	Magnus effect	Aluminum	Manufactured
9	Rotating Shafts	Rotate the large shaft	Aluminum	Purchased

Table. 1b: Components of part B of MWT

Part #	Part Name	Description	Material	Manufacturing process
1	Choke	Keep shafts stable	Aluminum	Purchased
2	Low Speed Shaft	Transmit blade's rotation	Aluminum	Purchased
3	Brake System	Stops rotation of rotor	-	Purchased
4	Generator	Generate power	-	Purchased
5	Indicator	Wind direction indicator	Plastic	Purchased
6	Nacelle	Protects and covers the items	Aluminum	Manufactured
7	Yaw motor	Rotate the rotor	Aluminum	Purchased
8	High Speed Shaft	Connects gearbox to generator	Aluminum	Purchased
9	Pins	Enclose nacelle	-	Purchased
10	Microcontroller	Sends signal to yaw motor	Aluminum	Purchased
11	Gearbox	1:15 increasing rpm	Aluminum	Purchased

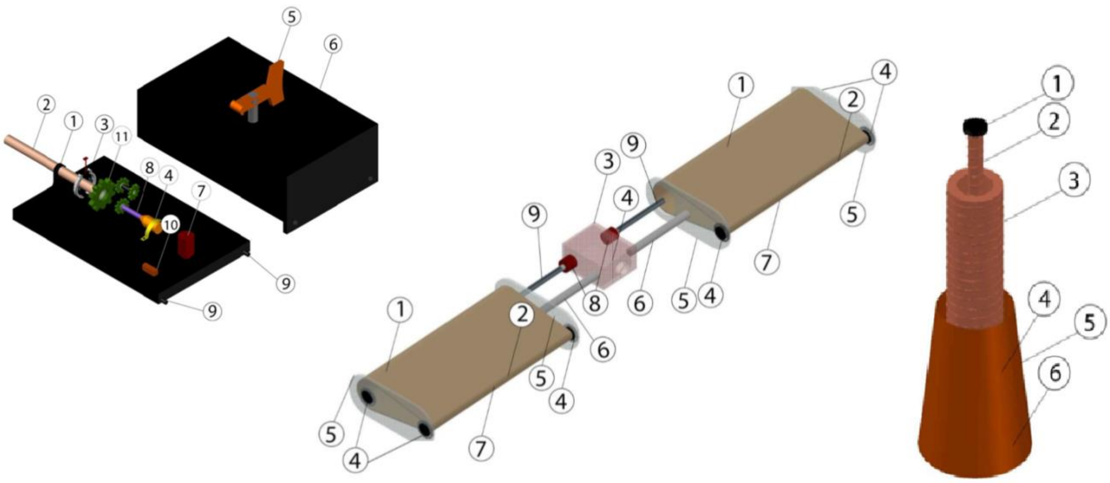

Figure. 2: Part A, B and C of the MWT assembled.

The lower body of the Magnus wind turbine is shown in Figure 2. The tower contains three parts: the base and two power screwed towers for lifting, also in the tower the bevel gear is shown inside the base of it for lifting the tower to the maximum height. The batteries of the turbine are hidden in the base of the tower, where one of the batteries is used for the yawing and lifting system, while the other battery is for lightning. Finally, the gear is installed at the top of the tower for the yawing system. Table 1c shows the entire components with the description, material, and manufacturing process.

Table. 1c: Component of part C of MWT

Part #	Part Name	Description	Material	Manufacturing process
1	Spur Gear	Yaw system	Aluminum	Purchased
2	Tower C	Power screwed Tower	Aluminum	Purchased
3	Tower B	Power screwed Tower	Aluminum	Purchased
4	Tower A	Base of Tower	Aluminum	Manufactured
5	Batteries	For initializing and charging	-	Purchased
6	Bevel Gears	For lifting system	Aluminum	Purchased

2.1. Design Proposal:

The MWT is divided into three main parts as shown in Figure 1, each part has different components. Some components need to be analyzed to avoid failures. Some components will be analyzed by calculations, while other parts will be numerically analyzed. The structural numerical analysis will be applied on stationary shafts that are connected between the hub and the airfoil blades to determine the stress, deflection and fatigue.

- The structural numerical analysis will be applied to the low-speed shaft to find stress, fatigue, deflection, and vibration.

- The structural numerical analysis will be applied to the towers to determine the stress, fatigue, buckling and deflection.

- Blades Analysis:

The first thing to start with is the blade's dimensions since they are the most important thing in the MWT. For rotating cylinder dimensions, assuming that: Airfoil shape of NACA 0021, the Speed ratio of α=1 and the Rated wind speed, V_{wind}= 15 m/s. Applying the speed ratio equation first to get the radius of the front cylinder of the blade:

$$\alpha = V_{Magnus} / V_{Wind} \quad (1)$$

$$\alpha = (\omega \times R_{cylinder}) / V_{wind} \quad (2)$$

The radius of rotating cylinder equal to:

$R_{cylinder} = 0.06\ (m)$

The diameter of rotating cylinder equal to:

$$D_{cylinder} = 2 \times R_{cylinder} \quad (3)$$

$D_{cylinder} = 0.12\ (m)$

The diameter of the front circle is almost considered to be equal to 21% of the rare diameter to make an approximate similarity to NACA0021. Diameter of rare cylinder:

$$D_{Rare\ cylinder} = 0.21 \times D_{Front\ cylinder} \quad (4)$$

$D_{Rare\ cylinder} \approx 0.03\ (m)$

Assume chord length to be 0.35 m.

For Rotor length assume the Coefficient of Power (C_p) =0.3, Density of Air (ρ)=1.225, Output Power (P) =1000 Watts and the Rated wind speed (V_{wind}) =15 m/s. Using power equation to measure rotor radius:

$$P = 0.5 \times \rho \times A \times V^3 \times C_P \quad (5)$$

Therefore, the rotor radius will be R_{rotor} =0.75 (m) by using equation 5.

For the stationary blade shaft Analysis: Stress analysis will be made to get the diameter of the shaft that connects the hub to the blades and supports them. Assume the Length (L)=0.24 m, Factor of Safety (n) =4, and Yield Strength (σy)=169 MPa.

$$n = \sigma_y / \sigma_{allowable} \quad (6)$$

$$\sigma_{allowable} = (M \times C) / I \quad (7)$$

Using equations 6 and 7, the minimum diameter that can be used is equal to d = 0.02 m. The chosen diameter, d=0.03 m. To analyze the low speed shaft stress (see Figure 3), the structural analysis will be applied to determine the diameter of the low speed shaft that connects the blades to the gearbox. By assuming the following: Length (L) =0.5 m, Factor of Safety (n) =4. 3 and the Yield Strength (σy) =169 MPa.

Determine the allowable stress to get the minimum diameter for the shaft by using equation 6 an 7, then the d = 0.03, so the chosen diameter d=0.04 m.

- Deflection Analysis

Structural analysis is applied to verify the deflection. Deflection analysis will help to know whether the material will handle the load or fail. In the case of Defection at blades, the length, height and width of each blade are given by 1.05, 0.17 and 0.4 m, respectively. Assuming the blades cantilever beam and has modulus of elasticity E=71.9 GPa. Then, the defection can be found by:

$$\delta = R \times L\ E \times I \quad (8)$$

$\delta = 1 \times 10^{-5}\ m$

While in the case of defection at Tip of low speed shaft, the length, mass and diameter of each blade is given by 0.1 m, 1.7 kg and 0.04 m, respectively. Assuming the blades cantilever beam and has modulus of elasticity E=71.9 GPa. Then, the defection can be found by deflection (Eq. 8), therefore the $\delta = 1 \times 10^{-6}$.

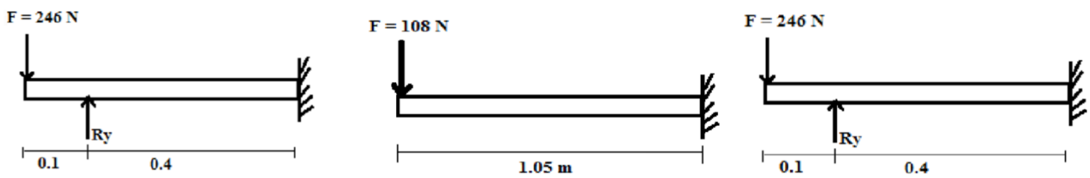

Figure. 3: Free body diagram of a. the low speed shaft, b. the stationary shaft and c. the Low speed shaft

- Vibration analysis

This analysis will help to determine whether there will be whirling in the low speed shaft or not. By Assuming: Eccentricity (a) $=2\times10^{-3}$ m, Mass (m) = 1.7 kg, Angular velocity (ω) =30 rpm, Length (l) =0.5 m and Diameter (d) =0.04 m.

Stiffness $(k) = (48 \times E \times I) / L^3$ (9)

Natural frequency $(\omega n) = (k/m)^{0.5}$ (10)

Frequency Ratio $(r) = \omega / \omega^n$ (11)

Amplitude $(A) = (\alpha \times r^2) / (1 - r^2)$ (12)

Substituting and solving equations 9, 10, 11 and 12, $A = 6.27 \times 10^{-8}\ m$. Therefore, there is no whirling in this shaft.

- Gearbox Analysis

Gearing analysis is applied to determine number of teeth and diameter of each gear. By assuming Gearbox ratio 15:1, Minimum number of teeth to avoid interference (N) =16, Pressure angle (ϴ) =14.5 and Module (m) =2 mm. Since the gearbox ratio is 1:15, the ratio of number of teeth can be taken as: $N2/N3 = 5$ and $N4/N5 = 3$ (see figure 4). So, $N2 = 5 \times N3 = 5 \times 16 = 80$ teeth, $N4 = 3 \times N5 = 3 \times 16 = 48$ teeth. Then diameter of each gear was can be determined by equation 13, so, the $D3 = 32\ mm$, $D2 = 160\ mm$, $D4 = 96\ mm$.

$D = m \times N$ (13)

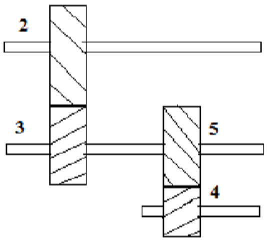

Figure. 4: Free Body Diagram of the Gearbox.

- High Speed Shaft Analysis

Lift Force can be calculated by equation 14, by Assuming the Rated wind speed, V_{wind}=15 m/s, Lift Coefficient, CL=1.2 and out power, P= 1000 watt

Lift force equation $(L) = 1\ 2 \times C_L \times \rho \times A \times v^2$ (14)

Torque equation $(T) = L \times 1\ 3 \times R_{rotor} \times n$ (15)

power equation $(P) = T \times \omega$ (16)

Substituting all the variables, the lift force L = 43.41 N, the torque $T = 21.705\ N.m$ and $\omega = 440\ rpm$.

The structural analysis will be applied to determine the diameter of the high-speed shaft that connects the gearbox to the generator. Assuming, Torque (T)=21.705 N.m, Factor of Safety (n) =4. 3, Yield Strength (σy) =169 MPa, Length (l) =0.12 m and Pressure angle (ϴ)=14.5.

Tangential force $(F_{tang}) = T / R_{gear}$ (17)

Normal force ( ) $= F_{tang} \times \tan 14.5$ (18)

Moment equation $(M) = F_{normal} \times L$ (19)

Substituting and solving equations 6, 7, 17, 18 and 19, the minimum diameter that can be used is equal to d = 0.015. Then the chosen diameter d=0.02 m.

3. Result: Numerical Analysis (CAD)

In this section, numerical analysis was applied to the low speed shaft, stationary shaft, and the tower using COMSOL, (*COMSOL* Multiphysics software, this software is an interactive environment for modeling and simulating scientific and engineering problems and applications). The studies on these parts were Solid mechanics studies using the Von Mises failure theory (Wenchao et al., 2016; Rao et al., 2016), and Findley's fatigue studies were applied to determine the fatigue of the first study. The materials used on all of these parts are assumed to be aluminum in COMSOL, and the properties assumed for the aluminum are shown in the table below.

Table. 2: Properties used for COMSOL

Property	Value	Unit
Density	2700	Kg/m^3
Young's modulus	70×10^9	Pa
Poisson's ratio	0.33	--
Findley's stress sensitivity coefficient	0.2	--
Findley's limit factor	213×10^6	Pa
Matake's stress sensitivity coefficient	0.27	--
Matake's limit factor	223×10^6	Pa

The tower is divided into three parts, where it is assumed that it is fixed at the bottom while it has an axial force at the top for each part. The boundary conditions are fixed constraint at the bottom of each part and a boundary load at the top of each part of the tower. For the upper part of the tower, it is shown in figure 5 that the Von Mises stresses and the buckling are moderately high. This agrees with the results of another study conducted by Genzalez et al (2011), they showed that The Von Mises criterion is a good option for ductile materials with equal tensile and compressive strength, which is coincident with Von Mises for non-ductile materials.

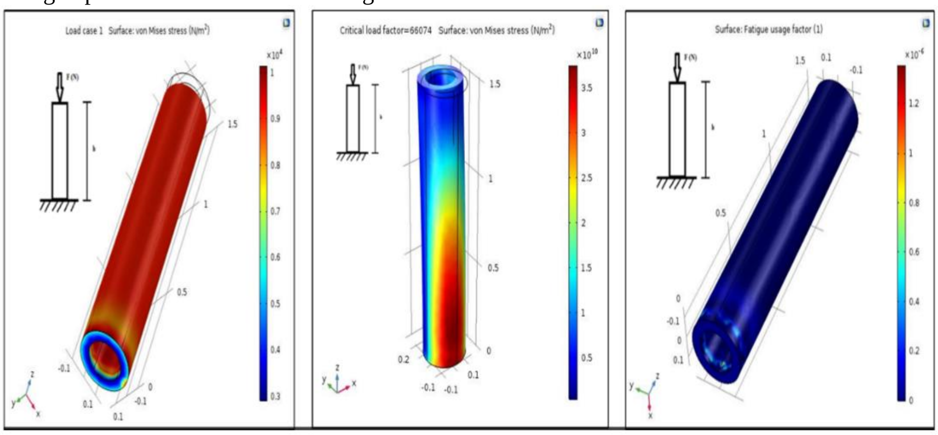

Figure. 5: a. Stress at the upper tower, b. Buckling in the upper tower and c. Fatigue in the upper tower

The fatigue analysis boundary conditions were taken from the studies of solid mechanics (see figure 5c). It is shown that the Findley's fatigue of the upper part of the tower is very low. The maximum fatigue of this part occurred at the bottom, consistent with the analysis study conducted by Li. H et al., (2018), that the fatigue damage relates much with the axial stress of the tower base, and under higher wind speed, the tower base experiences higher fatigue damage.

For the middle part of the tower, the boundary conditions are fixed constraint at the bottom of this part and a boundary load at the top of this part of the tower. It is shown in figure 6 that the Von Mises stresses and the buckling is moderately high, that corresponding with Chantharasenawong et al., (2011), that an Increasing in base diameter, not reflected in lower tower mass but also improves the stability of structures with a higher natural frequency of tower and lower maximum tip deflection.

As shown in figure 6, the fatigue analysis boundary conditions were taken from the studies of solid mechanics. It is shown that Findley's fatigue in the middle part of the tower is very low. The maximum fatigue of this part occurred at the bottom. Also, the fatigue in this part is less than the fatigue of the upper part of the tower.

Finally, the base of the tower the Von Mises stresses are different from the previous two parts. The boundary conditions are fixed constraint at the bottom of this part and a boundary load at the top of this part of the tower. It is shown in figure 7 the Von Mises stresses are low at the bottom while high at the top, and the buckling is very high at the top while it is low at the bottom of the base.

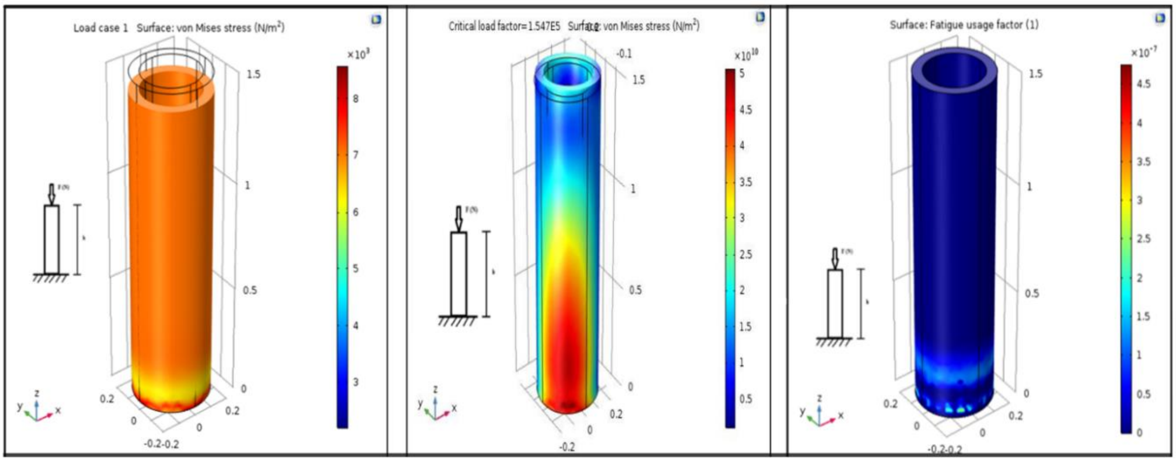

Figure. 6: a. Stress in middle tower, b. Buckling of the middle tower and c. Fatigue in the middle tower

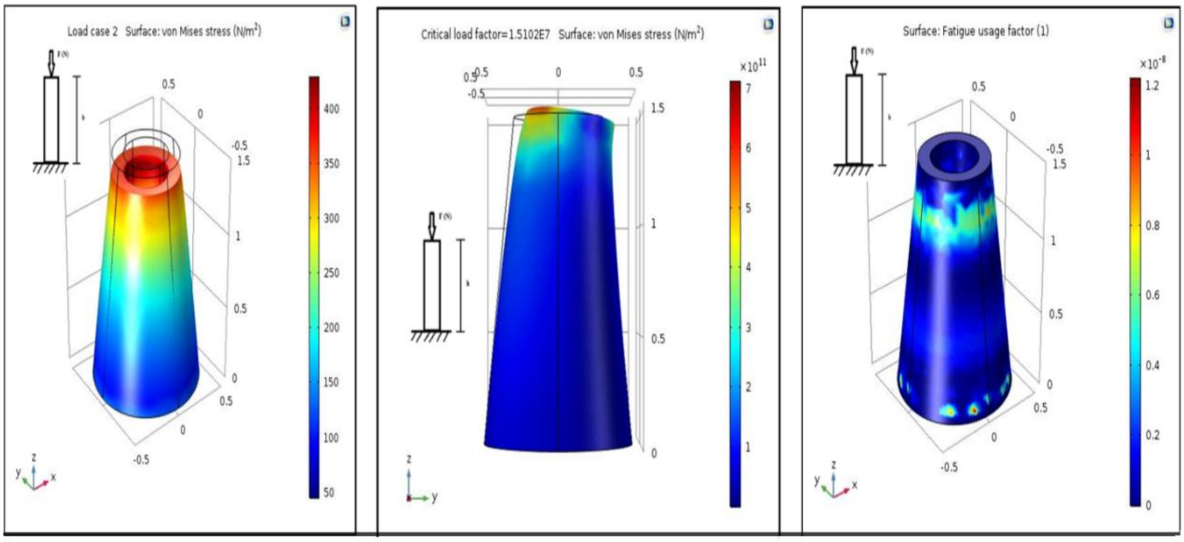

Figure. 7: a. Stress at the tower base, b. Buckling at the tower base and c. Fatigue in the tower base

The fatigue analysis boundary conditions were taken from the studies of solid mechanics (see figure 7c). It is shown that Findley's fatigue of the base part of the tower is moderately low. The maximum fatigue of this part occurred at the bottom. Also, the fatigue in this part is less than the fatigue of the upper part of the tower, this is related to the dimensions, geometry and material of the tower in addition to the dynamic cyclic loading of wind speed and motion.

The numerical analysis of the low-speed shaft in COMSOL is shown below where the shaft was assumed to be a simple design problem of a fixed beam that has a force at the end and torque. The boundary conditions of the low-speed shaft are a fixed constraint on the left side of the shaft, a point load on the top right side of the shaft, and a rotating frame with a speed of 30 RPM. Solid mechanics stationary studies were applied to determine Von Mises stresses and Findley's fatigue analysis was applied to determine fatigue of the first study.

In figure 8, the stress on the low-speed shaft is shown, where the maximum stress is in the point load and in the fixed part of the shaft. While in Figure 8b, the deflection of the low-speed shaft is shown, where the maximum deflection occurred at the point load.

Parametric studies were done for the low-speed shaft; table 3 shows the effect of the force on the stress and deflection of the low-speed shaft. It is shown that whenever the force increases, the stress increases for this design and geometry, therefore, the deflection increases. Table 4 shows the effect of the radius on the stress and deflection of the low-speed shaft. It is shown that whenever the radius increases, the stress decreases due to the increase in the exposed area, therefore, the deflection decreases.

Table. 3: Parametric study for the low speed shaft by changing the force.

$Force\ (N)$	RPM	$Stress\ (\frac{N}{m^2})$	$Deflection\ (mm)$
200	30	2.12E+07	3.038
400	30	4.24E+07	6.076
600	30	6.36E+07	9.113
800	30	8.48E+07	12.151
1000	30	1.06E+08	15.189

Table. 4: Paraetyric study for the low speed shaft by changing the radius.

$Radius\ (m)$	$Stress\ (\frac{N}{m^2})$	$Deflection\ (mm)$
0.01	1.42E+08	45.69
0.018	2.96E+07	4.61
0.026	1.44E+07	1.13
0.034	6.56E+06	0.41
0.042	5.39E+06	0.20
0.05	2.96E+06	0.10

The fatigue analysis boundary conditions were taken from the studies of solid mechanics (see figure 8c). It is shown that the Findley's fatigue of the low-speed shaft is moderately low. The maximum fatigue of this part occurred at the point load.

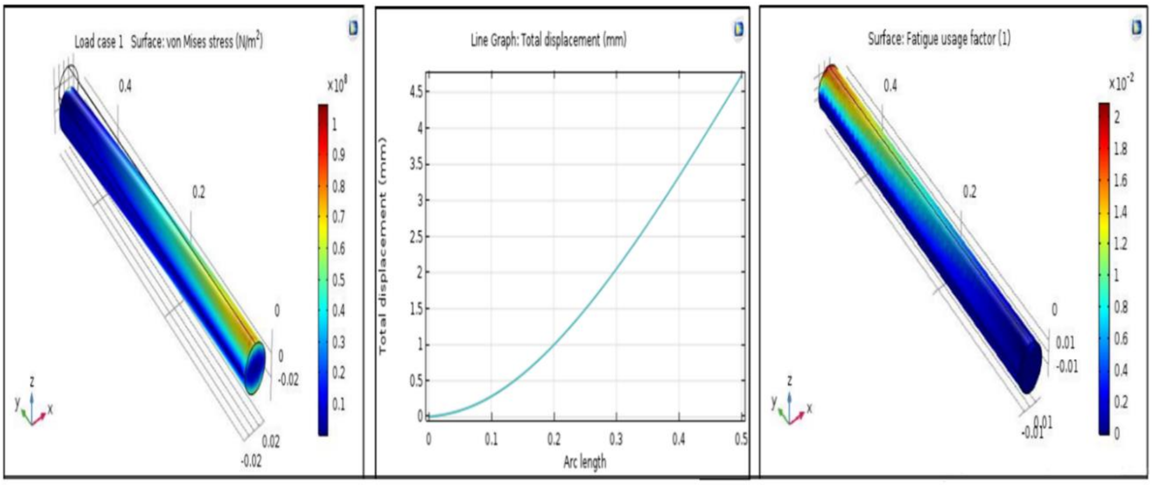

Figure. 8: a. Stress in the low speed shaft, b. Deflection in the low speed shaft and c. Fatigue of the low speed shaft.

3.1. Stationary shaft

The stationary shaft is placed between the hub and the blades. Numerical analysis was applied to determine the Von Mises stresses and fatigue where the shaft was assumed to be a simple design problem of a fixed beam that has a force at the end. The boundary conditions of the low speed shaft are a fixed constraint on the left side of the shaft, a point load on the top right side of the shaft. Solid mechanics stationary studies were applied to determine Von Mises stress and fatigue analyses were applied to determine fatigue of the first study.

In figure 9a, the stress on the stationary shaft is shown, where the maximum stress is in the point load. While in figure 9b, the deflection of the stationary shaft is shown, where the maximum deflection occurred at the point load. In figure 9c below, the fatigue analysis boundary conditions were taken from the studies of the solid mechanics. It is shown that the Findley's fatigue of the stationary shaft is moderately low. The maximum fatigue of this part occurred at the point load and at the fixed part.

Parametric studies were done for the stationary shaft. Table 5 shows the effect of the force on the stress and deflection of the stationary shaft. It is shown that whenever the force increases, the stress increases, therefore, the deflection increases. Table 6 shows the effect of the radius on the stress and deflection of the stationary shaft. It is shown that whenever the radius increases, the stress decreases, therefore, the deflection decreases. Table. 6: Parametric Study for the Low-Speed Shaft by Changing the Radius.

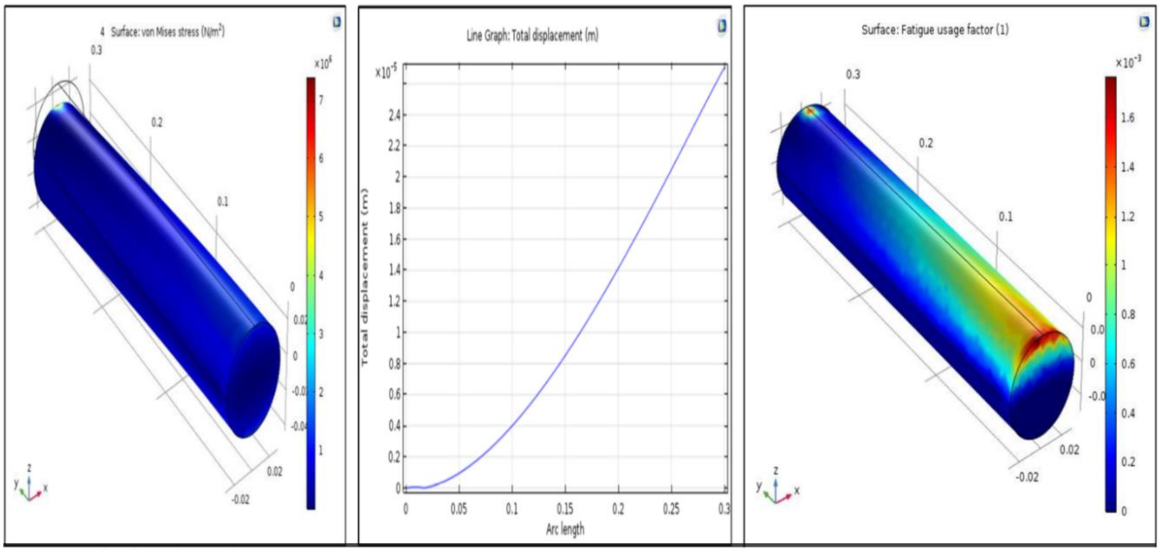

Figure. 9: Stress in the stationary shaft, b. Deflection in the stationary shaft and c. Fatigue in the stationary shaft.

Table.5: Parametric Study for the Stationary Shaft by Changing the Force

$Force\ (N)$	$Stress\ (\frac{N}{m^2})$	$Deflection\ (mm)$
200	1.33E+07	0.34
400	2.65E+07	0.67
600	3.98E+07	1.01
800	5.30E+07	1.34
1000	6.63E+07	1.68

Table. 6: Parametric Study for the Stationary Shaft by Changing the Radius

$Radius\ (m)$	$Stress\ (\frac{N}{m^2})$	$Deflection\ (mm)$
0.01	2.71E+08	35.50
0.02	9.28E+07	3.09
0.03	2.65E+07	0.67
0.04	1.96E+07	0.33
0.05	2.31E+07	0.31

Conclusion

The Magnus wind turbine (MWT) with cylinder blades was modeled by using numerical simulation COMSOL, and aerodynamic characteristics were evaluated. The results of the modeling show that the suggested design of turbine is going to be portable where it can fit into small areas. Also, there is no visible deflection, and the induced stress is less than the allowable limit which points out that the blade is safe, subsequently, no visible deflection is detected which results in no fatigue and this indicates that the low speed shaft, the upper tower, middle and base are safe.

Moreover, the analysis results reveal that the blade can be modeled as a cylinder with built-in support at the end of the hub. A uniformly distributed load is analyzed to represent aerodynamic lift with the high air force. As the force increases, the stress increases, therefore, the deflection increases. The MWT evaluation results illustrate that the radius of the stationary shaft increases, the stress decreases, therefore, the deflection decreases.

Reference

[1] Abbott. H and Doenhoff. A. E. von. 1959. Theory of Wing Sections. Dover Publications. New York, 326: pp. 113-115.

[2] AhmedaS. A and Mahammeda. H. O. 2012. A Statistical Analysis of Wind Power Density Based on the Weibull and Ralyeigh models of "Penjwen Region" Sulaimani/ Iraq, Jordan Journal of Mechanical and Industrial Engineering, 6(2), pp.135-140.

[3] AEO. 2017. Annual enery outlook 2017 with projections to 2050.

[4] Benatiallah. A, Kadi. L , Dakyo. B . 2010. Modelling and Optimisation of Wind Energy Systems, Jordan Journal of Mechanical and Industrial Engineering, 4(1), pp.143-150.

[5] BORG/ LUTHER group. 1986. The Magnus effect: An overview of its past and future practical applications.

[6] Cox. D., Davis. C., Ford motor co., Deaborn., MI. 2003. Wind energy: A report prepared for the panel on public affairs (POPA). American physical societyWilliam.

[7] Chantharasenawong. C., Jongpradist. P and Laoharatchapruek. S. 2011. Preliminary Design of 1.5-MW Modular Wind Turbine Tower. The 2nd TSME International Conference on Mechanical Engineering 19-21 October 2011, Krabi, Thailand.

[8] Fauzan. M. F., Chelvan. R. K., Amirah. A., 2017. Energy, Economic and Environmental Impact of Wind Power in Malaysia. International Journal of Advanced Scientific Research and Management. 2 (7).

[9] Ferdous. S., Bin Khaled. W , Ahmed. B., Salehin. S., Ovy. E. 2011. Electric Vehicle with Charging Facility in Motion using Wind Energy. World Rene. Energy congress. 8 -13 may 2011. Linkoping Sweden.

[10] Ghenai. C , Salameh. T , Janajreh. I.2017. Modeling and Simulation of Shrouded Horizontal Axis Wind Turbine Using RANS Method, Jordan Journal of Mechanical and Industrial Engineering, 11(4), pp.235-243.

[11] Golding. E. 1976. The generation of electricity by wind power. Halsted press, New York.

[12] Gregorek. G. M., Hoffmann. M. M., and Berchak. M. J. 1989. Steady State and Oscillatory Aerodynamic Characteristics of a NACA 0021 Airfoil: Data Report, Ohio State University, Columbus, OH.

[13] Jinbo. M., Farret. F. A., Junior. G. C., Senter. D., Lorensetti. M. F. 2015. MPPT of Magnus Wind System with DC Servo Drive for the Cylinders and Boost Converter. Journal of Wind Energy Volume 2015, Article ID 148680, 10 pages.

[14] Kaygusuz. K. 2004. Wind Energy: Progress and Potential. Energy Sources, 26:pp. 95–105.

[15] Khatri. K. K , Sharma. D , Soni. S. L, Kumar. S, Tanwar. D . 2010. Investigation of Optimum Fuel Injection Timing of Direct Injection CI Engine Operated on Preheated Karanj-Diesel Blend. Jordan Journal of Mechanical and Industrial Engineering, 4(5), pp. 629-640.

[16] Kunz .T.H., Arnett .E.B., Erickson .W.P., Hoar .A.R., Johnson .G.D., et al. 2007. Ecological impacts of wind energy development on bats: questions, research needs, and hypotheses. Frontiers in Ecology and the Environment. 5: pp.315–324.

[17] Li. H., Hu. Z., Wang. J., Meng. X. 2018. Short-term fatigue analysis for tower base of a spar-type wind turbine under stochastic wind-wave loads. International Journal of Naval Architecture and Ocean Engineering. 10(1):PP. 9- 20.

[18] Lu. X., McElroy. M. B., Kiviluoma. J. 2009. Global potential for wind-generated electricity. Communicated by James G. Anderson, Harvard University, Cambridge, MA. 106 (27):pp. 10933-10938.

[19] Minderman. J., Pendlebury .C.J., Pearce-Higgins .J.W., Park .K.J. 2012. Experimental Evidence for the Effect of Small Wind Turbine Proximity and Operation on Bird and Bat Activity. PLOS ONE. 7(7).

[20] Mayouf Messaoud, Bakhti Hadia , Dahmani Aissab. 2018. Sensorless Control System Design of a Small Size Vertical Axis Wind Turbine, Jordan Journal of Mechanical and Industrial Engineering, 12(2), pp.93-98.

[21] Messaoud. M and Abdessameda. R. 2011. Modeling and Optimization of Wind Turbine Driving Permanent Magnet Synchronous Generator. Jordan Journal of Mechanical and Industrial Engineering, 5(6), pp.489-44.

[22] Mishra. S., Purwar. S., Kishor. N. 2017.Maximizing Output Power in Oscillating Water Column Wave Power Plants: An Optimization Based MPPT Algorithm. Technologies. 6(15).

[23] Musgrove. P.J. 1993. Wind energy conversion- an introduction. IEEE proceeding. 130(9): pp. 506-516.

[24] Owens. B. 2014. The rise of distributed power.

[25] Pérez-González. A., Iserte-Vilar. J., González-Lluch. C. 2011. Biomed Eng Online. 2011; 10: 44. Published online 2011 Jun 2. doi: 10.1186/1475-925X-10-44. PMCID: PMC3123583.

[26] Rao. R. S., Mohan.S., G. Kumar. S. 2016. Determination of Fatigue Life of Surface Propeller by Using Finite Element Analysis. IJESC. 6(8).

[27] Schubel. P.J and Crossley. R. C. 2015. Wind Turbine Blade Design. Energies. 5.

[28] Seifent. J.2012. A review of the Magnus effect in aeronautics. Progress Aerospace sciences. 55: pp. 17-45.

[29] Sun. X., Zhuang. Y., Cao. Y., Huang. D., Wu. G. 2012. A three-dimensional numerical study of the Magnus wind turbine with different blade shapes. Journal of Renewable and Sustainable Energy 4(6).

[30] Tangler. J. 1994. Advanced wind turbine design studies advanced conceptual study final report. NREI. National Technical Information Service.

[31] Wenchao. L., Luca. S., Harm. A., Fangfang. L., Tianhua. Z.2016. Assessing the integrity of steel structural components with stress raisers using the Theory of Critical Distances. doi: 10.1016/j.engfailanal.2016.07.00.

[32] WWEA .2012. Small Wind Report 2012. World Wind Energy Association, Bonn, Germany.

المملكة الأردنية الهاشمية

الجامعة الهاشمية

المجلة الأردنية
للهندسة الميكانيكية والصناعية

JJMIE

مجلة علمية عالمية محكمة

تصدر بدعم من صندوق البحث العلمي

http://jjmie.hu.edu.jo/

ISSN 1995-6665

المجلة الأردنية للهندسة الميكانيكية والصناعية

المجلة الأردنية للهندسة الميكانيكية والصناعية: مجلة علمية عالمية محكمة تصدرعن الجامعة الهاشمية بالتعاون مع صندوق دعم البحث العلمي والابتكار- وزارة التعليم العالي والبحث العلمي في الأردن.

ترسل البحوث إلى العنوان التالي

رئيس تحرير المجلة الأردنية للهندسة الميكانيكية و الصناعية

الجامعة الهاشمية
كلية الهندسة
قسم الهندسة الميكانيكية
الزرقاء - الأردن

هاتف : 3903333 5 00962 فرعي 4147

Email: jjmie@hu.edu.jo

Website: www.jjmie.hu.edu.jo